AN END-TO-END MODEL OF AN ELECTROTHERMAL CHEMICAL GUN

by

Andrew James Porwitzky

A dissertation submitted in partial fulfillment
of the requirements for the degree of
Doctor of Philosophy
(Aerospace Science)
in The University of Michigan
2008

Doctoral Committee:

Professor Iain D. Boyd, Co-Chairperson
Professor Michael Keidar, Co-Chairperson
Professor Brian E. Gilchrist
Richard A. Beyer, U.S. Army Research Laboratory

You're gonna be nowhere,
the loneliest kind of lonely.
It may be rough going,
just to do your thing's the hardest thing to do.
But you've gotta make your own kind of music,
sing your own special song,
make your own kind of music,
even if nobody else sings along.

Make Your Own Kind of Music by Mama Cass Elliot

To my beautiful wife, Liz.
Without her, none of this would have been possible.

ACKNOWLEDGEMENTS

First and foremost, I must thank my doctoral committee for their time and assistance in the pursuit of my studies. I thank Professor Brian Gilchrist for taking the time to serve as my cognate member. Dr. Richard Beyer traveled from the U.S. Army Research Laboratory to participate in my defense, and has served as one of the primary collaborators for my research. Professors Iain Boyd and Michael Keidar have been my advisors during my time at the University of Michigan, and I could not have hoped for better. Professor Keidar has been supportive and had full confidence in me from the first day we met. His never-ending confidence and support has helped me to conduct my research, and for that I thank him immensely.

There are several people at the U.S. Army Research Laboratory in Aberdeen Maryland that have helped me with my work by providing valuable comments, recommendations and data. Without the following people my job would have been considerably harder: Dr. Michael Nusca, Dr. Anthony Williams, and Dr. Rose Pesce-Rodriguez.

I have many friends and colleagues here at the University of Michigan that have made my time here enjoyable. Some I have known but a few months, some have since moved on to continue their lives outside the University, but I thank them all for their friendship. They are Dave Berger, Jeremy Boerner, Tim Deschenes, Ethan Eagle, Tim Holman, Tyler Huismann, Leo Scalabrin, Tom Schwartzentruber, Tony Tan, Anton VanderWyst, and John Yim.

I have been truly blessed in my life to have wonderful friends that have stood by me over the years. I am truly proud to call these people my friends, and I think of them all as family: Charlie Brooks, Kyla LaRock, Alexandre Martin, Kim Mobley, and Emily Schelley.

My family have helped to make me the person I am today. My Mom and Dad raised me to be independent and to stand up for myself and my beliefs, no matter how unpopular that may make me. Bill and Nancy Rowell welcomed me into their home and their family with open arms, and have shown me nothing but love in the years I have known them.

A very special thanks must go to my best friend, and "best chick", Talia Karchem. Talia has helped me through some tough times in the years that we have known each other. No matter what mood I am in, I can call her up and have a laugh. I can't imagine not having her as my best friend, and I love her like a sister.

As is customary with acknowledgements, the most important person comes last. None of my achievements over the last eight years, and, indeed, for the rest of my life, would be possible without my beautiful wife, Elizabeth Rowell. If I filled this entire book with discussion of how I feel about Liz, it would still be insufficient to communicate what she means to me. She has always loved me for who I am. This thesis is dedicated entirely to her, because without her, I would not have had the opportunity to do any of the research contained within. So Liz, my biologist wife, I know you will probably never read a page past this one, so you can stop with the next sentence. I love you very much.

TABLE OF CONTENTS

LIST OF FIGURES

Figure

LIST OF TABLES

Table

LIST OF NOMENCLATURE

Physical Constants

ϵ_o	Permittivity of free space, 8.8542×10^{-12} F/m
e	Elemental charge, 1.6022×10^{-19} C
k	Boltzmann constant, 1.3807×10^{-23} J/K

Acronyms

ARL	U.S. Army Research Laboratory
CFD	Computational fluid dynamics
E3TC	End-to-end electrothermal chemical gun (model)
ETC	Electrothermal chemical
ETI	Electrothermal ignition
PPI	Plasma-propellant interaction
PPT	Pulsed plasma thruster

LIST OF APPENDICES

Appendix

CHAPTER I

Introduction

There has been much interest in recent years in the design and implementation of electrothermal chemical (ETC) guns. An ETC gun is a solid propellant based artillery piece in which the conventional ignition system has been replaced with a capillary plasma source. Numerous enhancements to the propellant combustion are achieved by igniting the propellant with a plasma. Some of the benefits of plasma based ignition in ETC guns are reduced ignition delay time, highly repeatable ignition time and enhanced burning and combustion of the solid propellant [1, 2].

In 1998, the U.S. Army Research Laboratory (ARL) began a program to investigate the nature of the plasma-propellant interaction (PPI) encountered in ETC guns. The primary goal of the ARL program was to provide information on the basic physics and chemistry involved in the PPI, to facilitate the design and implementation of the technology on a large scale. It was felt that a reduction in size of the power supply equipment necessary for ETC ignition was unlikely within the next decade, and that the key to implementation of ETC technology rested on a thorough and fundamental understanding of the physics involved [2].

It is the purpose of this dissertation, funded in part by a grant from the U.S. Army Research Office, to explore the fundamental physics involved in the plasma-propellant

interaction via numerical simulations. Numerical modeling allows us to isolate key physics and explore the impact that different phenomena have on the PPI. Previous numerical studies of the ETC phenomenon did not explore the PPI, which is widely considered to be the source of many of the ETC enhancements [2]. It is the objective of this thesis to formulate a numerical model of an ETC gun, focused primarily on the plasma-propellant interaction leading up to propellant ignition, as after propellant ignition the burning will proceed normally. While numerical simulations are carried out, research continued into experimental explorations of the PPI phenomenon at ARL. The work presented in this dissertation was conducted in close collaboration with the ETC researchers at ARL in Aberdeen, Maryland.

1.1 Electrothermal Chemical Guns

Before proceeding, a clear definition of an electrothermal chemical gun must be put forward, as there is sometimes confusion in the community. A schematic diagram of an ETC gun is shown in Fig. 1.1. A capillary plasma source generates a plasma which enters the combustion chamber and begins to interact with the solid propellant. Upon ignition of the solid propellant, expanding combustion gases provide the impetus to the projectile. This differs from an electrothermal gun, which does not use solid propellant. In an electrothermal gun, the plasma enters an expansion region when it exits the capillary. It is the expansion of the plasma into a working fluid that provides the projectile impetus in an electrothermal gun. This dissertation exclusively considers electrothermal chemical guns, in which the solid propellant provides the projectile impetus, as in conventional gun-type weapon systems.

Among the enhancements obtained by plasma ignition of the solid gun propellant is a reduced, and highly repeatable, ignition delay time. Figure 1.2 shows chamber

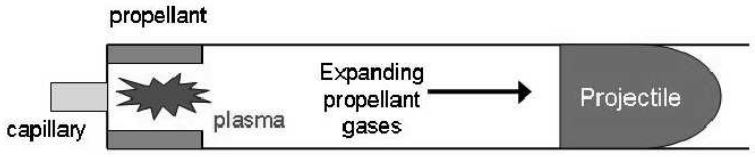

Figure 1.1: Schematic diagram of an electrothermal chemical gun.

pressure versus time curves for eleven conventional ignition and ten electrothermal ignition firings, taken from [3]. The peak chamber pressure is preceeded closely by the initiation of projectile motion within the gun barrel. It is clear that ETI results in shorter and highly repeatable ignition delay times. The effect of shorter and more reliable ignition delay times, when coupled to existing technologies such as a dynamic muzzle positioning system, can lead to remarkable improvements to both weapon accuracy and effectiveness. For some fire-on-the-move scenarios the probability of hit could be improved by up to 100% at 3 km for this combination of enhancements [3]. Additionally, due to the increased electrical energy deposited to the propellant by the plasma, temperature sensitivity to ignition time is greatly reduced. This means that the ignition delay time is also much more reliable over a range of operating temperatures. This effect can be seen in Fig. 1.3, taken from [3], which shows the muzzle velocity—a measurement of the propellant performance—for gun firings where the propellant was equilibriated to a range of different temperatures before firing. Even when conditioned to very low temperatures, ETC ignition results in performance near the ideal "hot performance" limit.

The higher peak pressure for the ETI firings in Fig. 1.2 is an example of what is commonly referred to as "enhanced burning/combustion", meaning that more energy, manifested here as a higher chamber pressure, is obtained from the same propellant as compared to conventional ignition. The plasma-propellant interaction theory of

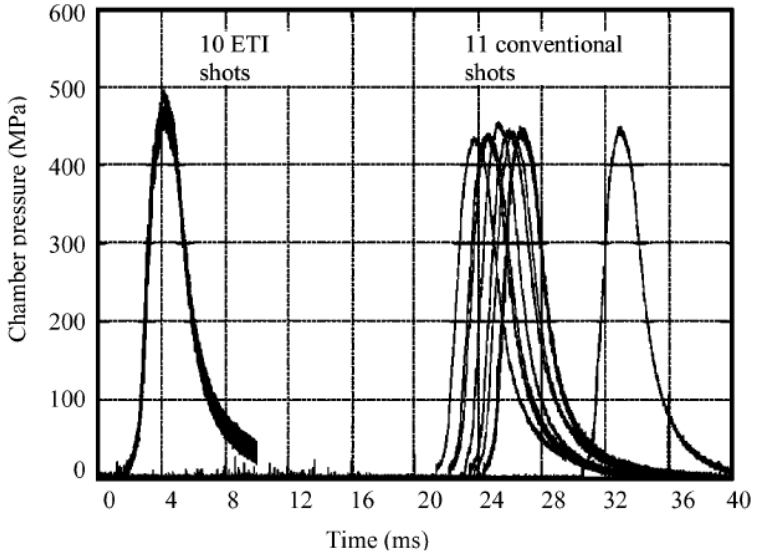

Figure 1.2: Comparison of the chamber pressure for conventional and plasma ignition (ETI) as a function of time, taken from [3].

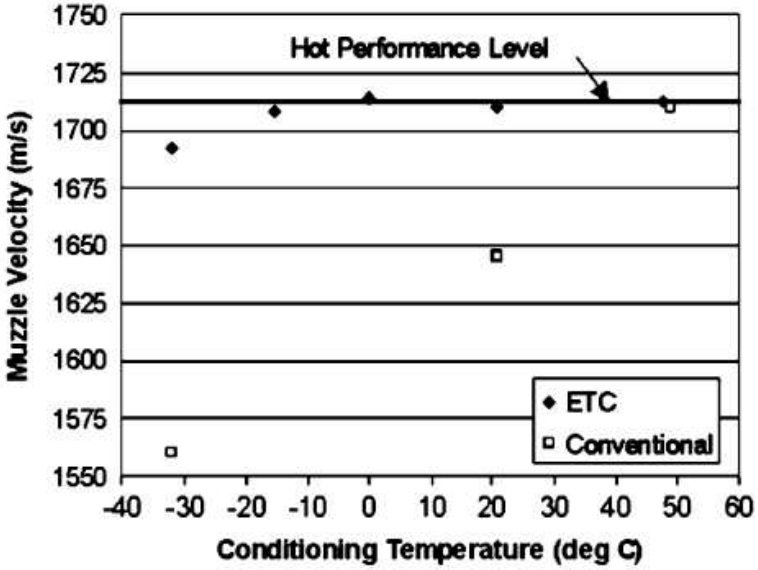

Figure 1.3: Muzzle velocity as a function of propellant pre-firing temperature for both ETC and conventional ignition, taken from [3].

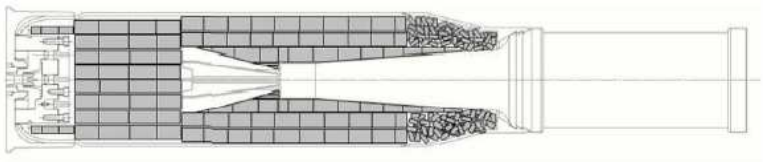

Figure 1.4: Diagram of a tight propellant packing choice, taken from [3].

Pesce-Rodriguez and Beyer states that the higher pressure is due to increased gasification of the propellant in the pre-ignition phase as compared to conventional ignition [2]. This increased gasification precedes the ignition (thus preceding the burn phase) and is due to the plasma-propellant interaction. "Enhanced burning/combustion" is thus not an appropriate term, but is commonly used in the community and literature.

As with conventional ignition systems, there is more than one choice for propellant packing options. The choice of propellant packing option changes the distance between the capillary plasma source and the propellant bed, which, as will be shown in Chapter III, has a significant effect on the plasma-air chemistry. Figure 1.4 illustrates a "tight" propellant packing option [3]. Illustrated on the left of Fig. 1.4 is a coaxial plasma injector, however the principle is the same for a capillary plasma source. On the right is the projectile. The propellant is cut into discs and loose blocks of varying sizes to ensure that little space remains in the shell. Small gaps are left that allow the igniting plasma to expand between the propellant blocks. This packing option yields a large surface area and high density of propellant.

Figure 1.5 shows an alternative packing option utilizing a bayonet tube [4]. A cylindrical bore is drilled in a propellant block. A bayonet tube is inserted into this bore. The tube contains holes at regular intervals that allow the igniting plasma to reach the propellant bed. The purpose of the tube is to provide regular injection/ignition sites along the length of the propellant bed. Without the tube, and

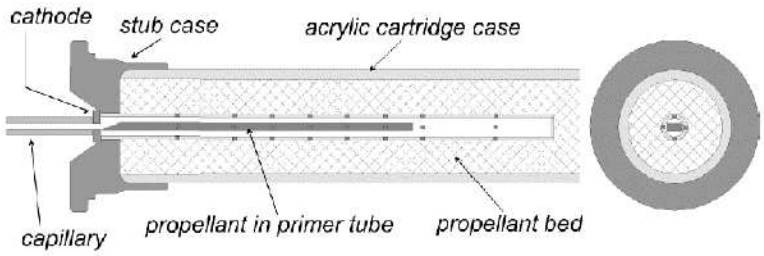

Figure 1.5: Diagram of a bayonet tube packing choice, taken from [4].

in the case of the tight packing option, ignition starts at the capillary end of the bed and proceeds toward the projectile end. The bayonet tube attempts to induce a more uniform ignition. It is clear from comparison of Fig. 1.4 and Fig. 1.5 that each option has a much different capillary-propellant distance. Indeed, the capillary-propellant distance varies significantly for the bayonet option, as different injection sites have different capillary-propellant distances. The capillary-propellant distance affects what reactions can take place in the plasma-air chemistry, thus altering the chemical composition of the plasma that reaches the propellant bed. Regardless of which propellant packing option is selected for final weapon implementation, the present work focuses on comparatively large capillary-propellant distances due to limitations in the experimental data.

All previous work on the expansion of the plasma jet for ETC application has had a major aspect in common: relatively large capillary-wall, or capillary-propellant, distances. There is typically a desire to inspect the propellant surface after it has been exposed to the plasma as this is highly informative [2]. It has been found in experiments that for small capillary-propellant distances the propellant is cracked or shattered by the initial pressure wave from the capillary firing [5], leading to typical experimental capillary-propellant distances greater than 20 mm. When a large capillary-wall distance is used it is typically because there are pressure sensors

located in the wall which are easily damaged by the high temperature, velocity and pressure of the jet near the capillary exit [5], again leading to larger sample distances. Since propellant fracturing alters the gross surface area of the sample in unknown ways, all experimental data useful for simulations concerning propellant mass loss is for large capillary-propellant distances. This makes it necessary to limit the present numerical studies to those situations. It should be noted that there are no assumptions in the presented model that would prevent simulation of small capillary-propellant distances, there is merely a lack of relevant and useful experimental data. Available experimental data is discussed in the next section.

1.2 Available Experimental Results

Experiments and numerical modeling can be two edges of the same sword. Experiments provide data that serve as boundaries, inputs, or validation of numerical simulations, while the results of numerical simulations can anticipate the outcome of experiments, suggest new experiments, or provide data that can not currently be measured by experimental techniques. Thus before any attempt can be made to numerically model an electrothermal chemical gun or the plasma-propellant interaction, a survey of available experimental data must be made. Since the work presented in this thesis was conducted without access to classified information, all experimental data must be available in the open literature.

The experimental data used in this thesis comes from two main sources: ARL and Pennsylvania State University. The work conducted at ARL led to much of the theoretical understanding of the plasma-propellant interaction referenced here, especially with regards to the propellant-radiation interaction. The experimental work exploring the PPI at Penn State provided much information that was useful for

numerical modeling. Presented here is an overview of the major experimental results that were utilized throughout this thesis. Included is discussion, from a modeling standpoint, of what data can be utilized, why and how.

1.2.1 Plasma Jet and Plasma-Air Chemistry

Li *et al.* collected much data regarding the expanding capillary plasma jet [5, 6, 7]. For each investigation conducted, the experimentally measured capillary electrical current was reported. As will be discussed in Chapter II, the electrical current supplied to the capillary plasma generator is the primary input required by the capillary numerical model. With this information it is possible to simulate the capillary used in each experiment. Coincidentally, most of the experiments conducted at Penn State used a capillary that was physically identical and had nearly identical current loading. This made it easier to compare multiple firings from an experimental standpoint, with the added benefit that only one capillary simulation need be carried out to model a number of different plasma jet experiments.

Experiments were conducted that directed a capillary plasma jet at a flat plate. The plate was instrumented with pressure sensors at regular intervals, providing time varying pressure profiles at discrete points along the wall [6]. Photographs of the plasma jet were also taken at regular intervals of 15 μs. This experimental data is utilized for comparison to computational fluid dynamics (CFD) results presented in Chapter III.

The plasma, being generated by a polyethylene capillary, is composed of atomic and ionized hydrogen and carbon, as well as free electrons. However, the plasma jet is passing through air, which is composed primarily of molecular oxygen and nitrogen. The high temperature of the plasma and the large ratio of air to capillary

plasma indicates that there is a significant possibility for plasma-air chemistry to occur. The chemical composition of the plasma can affect the plasma-propellant interaction, thus the plasma-air chemistry is of interest if the capillary-propellant distance is large enough to allow chemistry to occur. Indeed, the minimum capillary-propellant distance that leads to significant plasma-air chemistry is not known, but is something that will be estimated based on CFD results in Chapter III.

The capillary plasma jet was directed at a mass spectrometer probe in an attempt to measure the chemical makeup of the jet after any plasma-air chemistry had occurred [7]. It was quickly discovered that the flow time of the plasma jet was much less than the required sampling time of the mass spectrometer, meaning no data could be acquired before the plasma jet completely washed over the probe. In order the correct this problem the plasma jet must be slowed. This was accomplished by means of a plasma holding chamber. The capillary plasma generator was connected to a cylindrical holding chamber of radius 9.4 mm and length 129.5 mm [8] by a cylindrical nozzle of radius 1.6 mm [7]. Plasma exited the holding chamber through a 0.5 mm radius nozzle, and it was the chemical composition of this secondary jet that was measured [7]. Slowing the jet by means of the plasma holding chamber will allow additional chemical reactions to occur. This effect can not be measured by the experiment for the afore mentioned reason. Chemically reacting CFD simulations allow for the direct comparison of the primary and secondary jet, and will be presented in Chapter III. Additionally, in order to decrease heat loss to the holding chamber walls, which would further affect the plasma-air chemistry, the chamber walls were lined with polyethylene, the same material as the capillary liner. Observations of the liner after exposure to the capillary plasma jet indicate that the wall polyethylene ablated as far as 50 mm from the capillary nozzle, with a total mass loss three to five

times that of the mass loss from the capillary. To see what effect this had, the experimenters replaced the polyethylene liner with one of identical dimensions made of aluminum. Their results show that only CO intensity could be accurately measured, with all other chemical species being within the noise level of the measurement [7]. Essentially, by using a polyethylene liner, the experimenters created a much larger capillary. The higher mass loss due to this wall ablation increases the abundance of carbon and hydrogen in the plasma holding chamber, allowing new reaction mechanisms to occur. In the simulations conducted here, wall ablation was not used. This allows for comparison of how the capillary wall liner directly affected the chemical makeup of the secondary plasma jet. Those results are also presented in Chapter III.

1.2.2 The Plasma-Propellant Interaction

Samples of three solid gun propellants under consideration for ETC application were exposed to direct impingement by a capillary plasma jet [5]. The test chamber was vented to prevent pressure buildup, a key component to propellant combustion. Propellant samples were weighed before and after exposure to the plasma, thus resulting in an exact measurement of mass loss due to the plasma-propellant interaction for three different propellants exposed to an identical plasma. The three propellants used were JA2, XM39 and M43. XM39 and M43 are chemically very similar, with the primary difference being the substitution of 7.6% by weight of acetyl triethyl citrate for an energetic plasticizer in M43 [9]. Since the chemical makeup of this plasticizer was unknown, the simulations presented in this work compare JA2 and XM39. The precise makeup and differences between JA2 and XM39 will be discussed in Chapter IV when the plasma-propellant interaction model is introduced.

Experimental measurements of the mass loss due to the plasma-propellant inter-

action were taken over a range of capillary discharge energies and capillary-sample distances. However, for capillary-sample distances of less than 25 mm, significant fracturing of the samples was discovered [5]. Fracturing is due to the impact of the plasma pressure front on the propellant surface. With the surface area of the sample discs known, the total mass loss due to the plasma-propellant interaction can be simulated, thus only cases without fracturing can be utilized. These simulations and their results are discussed in Chapter IV.

1.2.3 Plasma Radiation Effects

One of the most obvious possibilities for the source of the enhancements encountered in plasma ignition is the plasma radiation itself. Radiation from the plasma represents a new energy transfer mechanism not significant in conventional ignition. Photographic images of ETC propellants taken before and after exposure to plasma radiation show clear evidence of a strong propellant-radiation interaction [10, 2]. Radiation exposed propellants show voids and cracks not present in virgin samples [2]. Further, there is a clear correlation between the optical properties of the propellants and their response to plasma radiation. Semi-transparent propellants, such as JA2, show in-depth effects from plasma radiation up to 1 mm into the propellant bed [10, 2]. Effects documented include fracturing of the propellant near the exposed surface, as well as in-depth voids created as radiation strikes graphite particles in JA2, causing them to heat and explode. Optically opaque propellants, such as XM39, show far less response to plasma radiation. XM39 reflects most of the incident radiation back into the plasma, and some experiments indicate that it may have a reflectivity as high as 50% [11]. Experiments designed to shield propellant samples from physical contact with the plasma, while allowing the plasma radiation

to reach the sample, confirm that these effects are due to the radiation incident from the plasma, and no other plasma-propellant interaction effect [10].

Experimental work to attempt to measure the possible heat transfer due to the plasma radiation yielded interesting results. A capillary plasma jet was directed at a stagnation plate with heat flux gauges mounted along it's length. The heat flux gauges were shielded from the plasma by a sheet of transparent material that allowed the plasma radiation to impact the heat gauges. An experimental minimum range of values for effective surface radiative heat transfer as a function of capillary-sample distance and capillary charging voltage was obtained from the experiments [12]. This data is utilized in Chapter IV. It is worth noting here that the reported radiative heat flux is far less than one would expect from a black body plasma. There is also evidence that ablated propellant material can act as a radiation shield, drastically reducing the amount of radiation that reaches the propellant bed [5]. For these reasons it is not trivial to attempt to model the radiation that actually reaches the propellant bed. If one could model the radiation signature from the capillary plasma as a function of time, the problem still remains to model radiation shielding, both by ablated propellant gases and by the solid propellant itself. Such a model would involve many physical parameters that may be unmeasurable over the range of conditions encountered in ETC application. Thus the present work takes the standpoint that radiation modeling, in this context, is at present futile. Rather, the decision was made to attempt to model all other heat sources in the PPI and present the radiation heat flux as the difference between all other heat fluxes and the total heat flux. This approach eliminates the need for complex, and sometimes questionable, radiation modeling while still yielding insight into the plasma radiation effects.

1.3 Thesis Overview

This chapter introduced and defined the concept of an electrothermal chemical gun. Discussed were some of the main enhancements encountered by using a plasma to ignite a solid propellant in terms of weapon performance. An overview was given of two main propellant packing options under consideration for ETC application, as well as how current experimental data relates to them. An overview of all major experimental data utilized in this thesis was then presented, along with discussion of how, and where, the data is used. The chapter concludes with a discussion of plasma radiation effects, with a summary of experimental data.

Chapter II describes the capillary numerical model employed in the present work. An explanation of the governing equations and physical assumptions is presented, as well as an overview of the solution method. The capillary model is used to conduct a parametric study to attempt to find the optimum peak discharge current and capillary size to maximize the peak outflow pressure or total capillary ablated mass. The effect of a time varying capillary internal radius is also explored. The primary result of this study is the discovery of the non-linear relationship between constant total deposited energy and total capillary ablated mass. The capillary code is then used to generate the inflow boundary condition for the CFD code.

Chapter III summarizes all original work performed with the computational fluid dynamics code LeMANS. A chemistry model for ETC application is presented that was developed based on available theoretical and experimental estimates of the makeup of the expanding plasma jet after the plasma-air interaction. Comparisons are made to experimental results. Three cases are presented and discussed. The first involves direct simulation of a capillary plasma jet expanding into an open chamber.

The second simulation studies the experiment referenced in Section 1.2 involving a plasma holding chamber. Comparison of these two simulations shows what effect the holding chamber had on the plasma chemical composition. Results from these two simulations yield refinements to the chemistry model, allowing for the elimination of some species as unnecessary and an increase in computational speed. The third simulation is of a bayonet tube packing option (Fig. 1.5) that clearly demonstrates the effect that the capillary-propellant distance has on the plasma-air chemistry. Conclusions from the plasma-air chemistry studies are presented.

Chapter IV presents the work on the plasma-propellant interaction model, the primary focus of this thesis. A summary of the previously developed ablation model, adapted for use in the plasma-propellant interaction, is presented. The coupling of the ablation to thermal models is discussed, resulting in the plasma-propellant interaction model which can determine the total effective heat flux to the propellant surface for a given experimentally determined ablated mass. A detailed overview of the relevant physical properties of the two gun propellants evaluated in this work, JA2 and XM39, is presented. Results from the PPI model are presented, and their meaning and implications are discussed. Conclusions are then drawn from the PPI modeling work.

Chapter V presents the model for the plasma sheath tailored for ETC application. An introduction to plasma sheaths is provided, with emphasis on the differences between fully collisional and collisionless sheaths, as well as theoretical limits for each extreme. The need for a sheath model in ETC work is explained. The sheath model is then coupled directly to the plasma-propellant interaction model from Chapter IV to determine the convective heat flux to the propellant bed. Results from the model are presented and discussed.

Chapter VI combines the coupled sheath/plasma-propellant interaction model with the CFD chemistry code and the capillary plasma source model to create the end-to-end electrothermal chemical gun model. Results are presented and compared to experimental data where possible.

Chapter VII summarizes all conclusions from prior chapters. A clear statement is made in Section 7.2 as to what work presented in this thesis is original and new, representing the contributions made to the field of electrothermal chemical gun research. In brief, the major contributions to the field include: the development of a plasma-air chemistry model for ETC application; simulations demonstrating the importance of plasma-air chemistry in ETC experimental geometries; the development of a plasma-propellant interaction model for determination of the total heat flux reaching the propellant bed; the development of a collisional plasma sheath model for determination of the convective heat flux reaching the propellant bed; and the combination of all the ETC submodels outlined in this thesis into a single ETC gun model. The chapter ends with suggestions for future areas of research in the field of ETC modeling.

Appendix A contains a detailed outline of the ablation model utilized extensively throughout this work. A derivation of the equation for convective heat flux in the plasma sheath model is presented in Appendix B. Appendix C contains qualitative discussions concerning the effect plasma-surface chemistry could have on the plasma-propellant interaction, and possible ways to model these phenomena, suggesting a future area of research.

CHAPTER II

Capillary Model

This chapter covers the model of the capillary plasma source used throughout this work. Presented in this chapter is an overview of the model itself, followed by the results of a parameter study conducted using the capillary model, as well as some interesting results concerning total deposited energy to the capillary. Although the model assumes the capillary internal radius does not change during the discharge, a time varying radius was incorporated, and studies were carried out to see what effect it has. A capillary simulation was performed to match the supplied electrical current profile from an experiment for use in Chapter III, and is summarized here so that all capillary model information is consolidated in one place. Some of the results presented in this chapter were first reported in [13].

The capillary numerical model utilized here was developed previously by Keidar *et al.* [14, 15]. The model was originally developed to model Teflon ablation in pulsed plasma thrusters [16], but was easily adapted to the polyethylene capillary plasma sources used in ETC application. Experimental validation of the model for polyethylene capillaries was conducted previously, and shows excellent agreement for the experimental total ablated mass [15]. Experimental validation with the capillary outflow pressure can not be performed, as there is no way to accurately measure the

pressure at the capillary nozzle. The capillary model consists of a kinetic ablation model strongly coupled to a quasi-neutral hydrodynamic plasma model. The ablation model is also used in the plasma-propellant interaction model, presented in Chapter IV. For this reason, details of the ablation model are presented in Appendix A. The details of the capillary model, specifically how the hydrodynamic region couples to the ablation model, are outlined below.

2.1 Overview of the Capillary Model

The capillary model uses kinetic ablation theory for the wall material [17, 18], coupled to a non-equilibrium hydrodynamic and a quasi-neutral bulk plasma layer, as illustrated in Fig. 2.1. A description of the ablation model can be found in Appendix A, as it is also used in Chapter IV. Solving the energy, momentum and mass conservation equations in the hydrodynamic layer allows for the determination of the plasma density and temperature at the polyethylene surface. The kinetic ablation model then determines the ablation rate, which in turn results in new plasma density, pressure, and plasma and surface temperatures [14].

The model is for a one dimensional axisymmetric capillary of length L and internal radius R. The spatial variable x varies from zero at the back of the capillary to the exit plane, at $x = L$. The model assumes that all flow parameters are uniform along the radial direction in each layer. The continuity, momentum and energy equations in the quasi-neutral plasma layer are, respectively,

$$A\left(\frac{\partial \rho}{\partial t} + \frac{\partial \rho U}{\partial x}\right) = 2\pi R\Gamma, \tag{2.1}$$

$$\rho\left(\frac{\partial U}{\partial t} + U\frac{\partial U}{\partial x}\right) = -\frac{\partial P}{\partial x}, \tag{2.2}$$

$$\rho\left(\frac{\partial \varepsilon}{\partial t} + U\frac{\partial \varepsilon}{\partial x}\right) = -P\frac{\partial U}{\partial x} + Q_j - Q_r - Q_F. \tag{2.3}$$

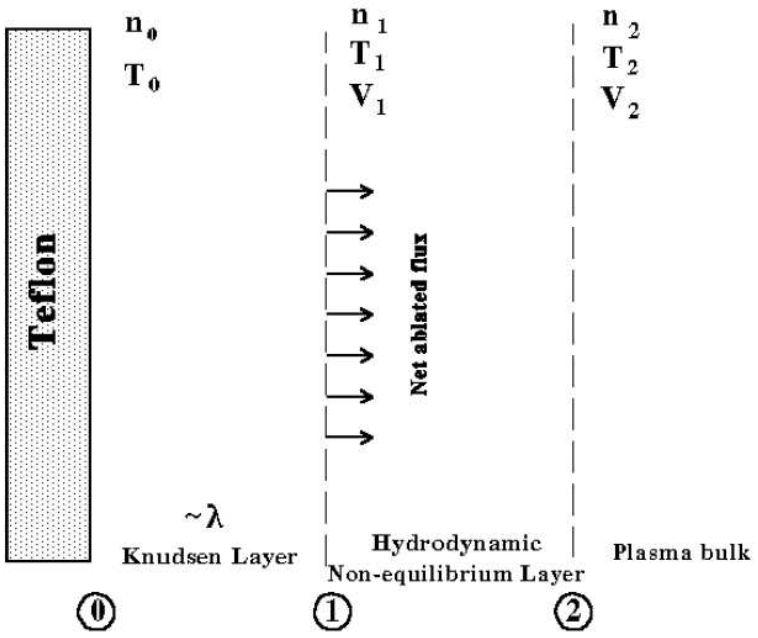

Figure 2.1: Diagram of the capillary model geometry, taken from [18].

Fluid density, velocity, and pressure are given by ρ, U and P, respectively. Capillary cross sectional area is given by A, and the ablation rate is given as Γ. It is assumed, due to the high pressure and small scale of the capillary, that pressure is constant in the quasi-neutral plasma layer, thus $\partial P/\partial x = 0$. Previous simulations and theoretical estimates indicate that the plasma temperature varies only slightly in the capillary, thus it is assumed that $\partial T/\partial x = 0$ [14]. In Eqn. 2.3, $\varepsilon = (3/2)(T_2/m) + (U^2/2)$, where T_2 is the plasma temperature in the quasi-neutral plasma layer, and m is the mass of an average fluid particle. The influx of energy to the plasma due to Joule heating is represented by $Q_j = j^2/\sigma$, where j is the electric current density and σ is the electrical conductivity determined by kinetic theory [14]. The form of the electrical conductivity used here is $\sigma = \epsilon_0\omega_p^2/(j\omega + \nu_m)$, where ϵ_0 is the permittivity of free space, ω_p is the plasma frequency, ω is the frequency of the oscillating current j, and ν_m is the sum of the electron-ion and electron-neutral collision frequencies,

all obtained via kinetic theory [19]. Energy losses due to plasma radiation to the wall is given by $Q_r = A_r Z_i^2 n_e n_i \sqrt{T_2}(1 + E_g/T_2)$ and comes from a simple black-body radiation model, where $A_r = 1.6 \times 10^{38}$ in SI units, the ion density is given by n_i, with E_g being the energy of the lowest excited state for the plasma [14, 20]. Energy losses due to convection are given by $Q_F = j_i(3T_2 + \phi)$, where $\phi = -T_2 \ln(j_{eth}/j_i)$ is the potential drop across the plasma sheath, j_i is the ion current density and j_{eth} is the thermal electron current density [14]. The form of Q_F will be discussed fully in Chapter V. For now it is sufficient to state that the basic form comes from kinetic theory.

Solving Eqns. 2.1 - 2.3 in the hydrodynamic layer yields the following relation for the ablation rate,

$$\Gamma = m n_1 V_1 = m n_1 \sqrt{\frac{n_2 k T_2 - n_1 k T_1}{m n_1 (1 - n_1/n_2)}}\ , \tag{2.4}$$

where k is the Boltzmann constant and n is the fluid number density. Subscript 1 represents values at the interface of the Knudsen and non-equilibrium hydrodynamic plasma layers, while subscript 2 represents values at the non-equilibrium hydrodynamic and quasi-neutral plasma layer interface [14]. Note that Eqn. 2.4 is only real if $n_1 k T_1 > n_2 k T_2$ and $n_1 > n_2$. If these conditions are not met the implication is that the backflux is higher than the flux from the wall into the bulk plasma. When this is the case, deposition to the polyethylene surface takes place instead of ablation, and the total ablated mass decreases. Both conditions are met during the discharge, thus the capillary model accommodates both situations. Polyethylene, and therefore the capillary plasma, is composed of carbon and hydrogen. Studies of film deposition have shown that carbon is likely to deposit and accumulate on the surface, while hydrogen is not. To account for this the model includes a parameter ν, which is the fraction of the backflux that deposits on the surface, with $\nu = 1$ being the most

deposition, and $\nu = 0$ neglecting deposition entirely [15].

The ablation model requires the polyethylene surface temperature, T_s, and the bulk plasma density and temperature, n_2 and T_2, as inputs. The latter are determined from the hydrodynamic model in the capillary. The polyethylene surface temperature is determined via a simple thermal model. The radial heat transfer equation, under the assumption that the heat layer thickness is much less than the cylinder curvature, is

$$\frac{\partial T(r,t)}{\partial t} = \alpha \frac{\partial^2 T(r,t)}{\partial r^2}, \tag{2.5}$$

where $\alpha = 2.84 \times 10^{-7}$ m^2/s is the thermal diffusivity of polyethylene. The boundary conditions for this situation are

$$-\lambda \frac{\partial T(R,t)}{\partial r} = q - \Delta H \Gamma - C_p(T_s - T_o)\Gamma, \tag{2.6}$$

$$\lambda \frac{\partial T(\infty,t)}{\partial r} = 0, \; T(r,0) = T_o, \tag{2.7}$$

where $r = R$ corresponds to the polyethylene surface, Γ is the polyethylene ablation rate, T_o is the initial temperature, ΔH is the enthalpy of sublimation of polyethylene, λ=0.5 W/Km is the thermal conductivity of polyethylene, and q is the heat flux. The analytical solution to Eqns. 2.5-2.7 is taken in the semi-infinite body limit, as this limit holds well under the condition of thin thermal boundary thickness.

In a real capillary, the discharge is typically initiated by an exploding wire [6]. The discharge current initially flows through the wire, causing it to explode, with the metal becoming ionized and forming a plasma. This "exploded wire plasma" serves to initiate polyethylene wall ablation, which generates further plasma, and the discharge is then stable, provided the discharge current continues to be supplied to the plasma. This exploding wire is replaced in the capillary model with an assumed initial plasma density and temperature. The initial conditions are consistent with

estimates of the plasma density and temperature from an exploded wire plasma, and the plasma density is small compared to the ablation sustained density provided by the capillary itself. Simulations that explored altering the properties of this initial plasma found that the simulation is not sensitive to the initial values, provided the plasma density and temperature are large enough to allow the capillary to enter the self sustained discharge mode. It should be noted that, in the capillary model, this initial plasma is assumed to have the same chemical composition as the discharge plasma, and that no metal ions are accounted for in the capillary simulation. The presence of metal in the capillary could be accounted for in the future. One of the most significant changes needed to accommodate the presence of the exploded wire would be the addition of an energy term representing the condensation of metal vapor to the polyethylene wall. Some of the initial metal plasma will be washed out of the capillary early on, but some will also condense to the polyethylene wall and re-ablate later during the discharge, an effect which will also need to be accounted for.

As inputs the capillary model requires capillary length and internal radius, a value for the backflux parameter ν, and a time varying electric current profile. For the parameter study, the capillary length is held constant at L=26 mm, a typical size for ETC capillaries [14, 21]. Similarly, the current profile is taken to be a sine wave with a half period of 300 μs, a typical discharge time for ETC experiments [14, 21]. The electrical current in the parameter study is thus completely defined by the peak current, I_{peak}. Previous simulations and experiments found good agreement with $\nu = 0.6$, however ν is varied here to find it's sensitivity under the current conditions.

As outputs, the capillary model generates time varying data for the capillary outflow density, pressure, temperature, species composition, and total capillary ab-

lated mass. Outflow velocity is assumed to be sonic as a boundary condition in the hydrodynamic model. The profile of the outflow pressure closely follows that of the discharge current, which is a sine wave here. Due to the range of temperatures and pressures encountered in the capillary, it is assumed that polyethylene molecules, C_2H_4, completely dissociate into atomic carbon and hydrogen. The Saha equation is used to find the ratio of atoms to ions for each species, while the quasi-neutrality condition determines the electron density [14]. The properties of interest in the parameter study are outflow plasma temperature T, peak pressure P_{peak}, and total capillary ablated mass M.

2.2 Capillary Parameter Study

Approximately one hundred simulations with varying conditions were performed for this parameter study. Presented here are the conclusions from the study, and representative data. A reference capillary was defined as follows

$$I_{peak} = 10 \text{ kA}, R = 1.6 \text{ mm}, \nu = 0.6. \tag{2.8}$$

Unless otherwise stated, all capillaries have a discharge time of 300 μs. The peak current takes on values of 10, 9, 7, 5, and 3 kA. Internal radius varies from 1.4 to 1.8 mm in increments of 0.1 mm. Note that for the simulations in this section, the internal radius does not change over time. The effects of a time varying internal radius are discussed in Section 2.3.

Presented in Table 2.1 is a selection of results from the parameter study. After a brief transient time, the plasma temperature in the capillary remains constant throughout the discharge, thus the temperature quoted in Table 2.1 is the plateau temperature.

Table 2.1: Selected results of the parameter study. *t_f=500 μs.

I_{peak}(kA)	R(mm)	ν	T(eV)	P_{peak}(MPa)	M(mg)
10	1.6	0.6	1.5	39.2	14.50
3	1.6	0.6	1.3	5.54	2.12
5	1.6	0.6	1.4	14.1	4.95
7	1.6	0.6	1.4	23.4	8.46
9	1.6	0.6	1.5	35.0	12.41
10	1.7	0.6	1.5	35.2	14.25
10	1.8	0.6	1.5	29.9	13.97
10	1.6	0.3	1.5	40.3	14.35
10	1.6	0.4	1.5	40.5	14.43
10	1.6	0.5	1.5	40.0	14.50
10	1.6	0.7	1.5	38.2	14.52
10	1.6	0.8	1.5	40.3	14.54
10	1.6	1.0	1.5	39.5	14.54
10*	1.6	0.6	1.5	39.9	24.20

Presented in Fig. 2.2 is a typical pressure versus time output from the capillary model. Severe fluctuations are clearly visible. These pressure fluctuations are due to the physical instability of the model. When the ablation model generates an ablated mass, that mass is converted into a pressure increase in the hydrodynamic model. This pressure increase changes the plasma density at the polyethylene surface, which then feeds back into the ablation model. This fully coupled treatment yields very accurate predictions for total capillary ablated masses, as discussed previously [15]. The drawback is that it is very unstable. All simulations here used a computational timestep of 10^{-11} seconds, while a complete simulation requires approximately fifty hours of CPU time. Reduction of the timestep failed to eliminate the fluctuations.

In order to accurately analyze this data, not only for this study but as input into a CFD code as discussed in Chapter III, a high order polynomial fit is performed on the simulation output. The fit is represented as the red curve in Fig. 2.2. Although similar fluctuations appear in plots of the plasma temperature, the previously stated stability of the temperature makes these fluctuations negligible, although a fit is still performed to provide input into the CFD code.

2.2.1 Conclusions from the Parameter Study

The results of the study indicate that for the range of parameters explored here, the selected value of ν has a negligible effect on the final ablated mass and peak pressure, indicating that backflux is not significant in this range. It is also apparent that the plasma temperature is only weakly dependent on the discharge current, thus an assumption that $T \approx 1.4 - 1.5$ eV is generally accurate. Increasing the discharge current leads to an increase in the plasma temperature. However, a rise in plasma temperature results in an increase in radiative and wall loses, thus cooling

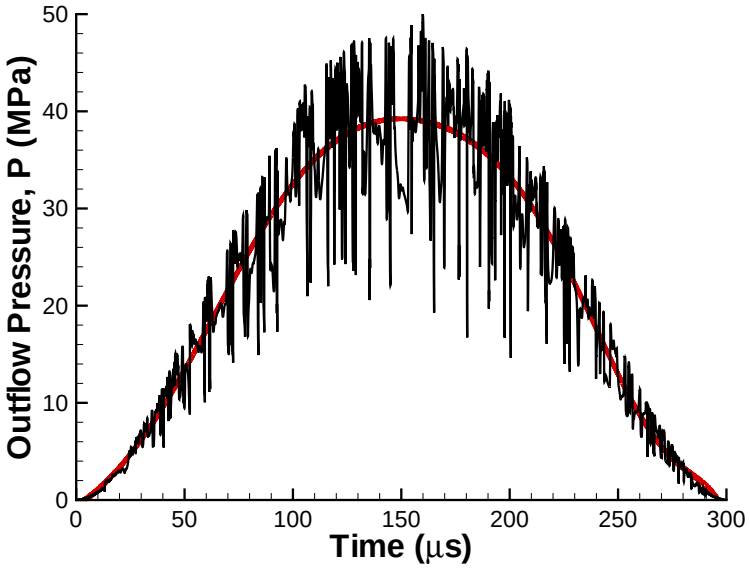

Figure 2.2: Reference capillary outflow pressure (black), and the polynomial fit (red) used to analyze the data.

the plasma. This results in a very stable plasma temperature over the parameter space explored here. It is this same effect that results in the plasma temperature maintaining a near constant level throughout the entire discharge.

Varying the internal capillary radius from 1.6 mm to 1.8 mm decreases the ablated mass by approximately 0.5 mg, which corresponds to a decrease of 3.7%. The peak pressure decreases by 10 MPa, or 23.7%. These two trends are to be expected. As the internal radius increases the Joule heating term (Q_j) in Eqn. 2.3 decreases as $j \propto 1/R^2$. Decreased Joule heating results in less ablation, resulting in a lower hydrodynamic pressure.

The greatest variation in both peak pressure and ablated mass comes from changing the discharge current. The variation in peak pressure and ablated mass as a function of peak discharge current show linear behavior. These results indicate that changing the current profile supplied to the capillary is not only the easiest way to alter the outflow pressure and ablated mass, but is also the most effective method,

as opposed to using capillaries of different internal radii.

An additional case is simulated in which a 500 μs discharge time is used for the reference conditions in Eqn. 2.8. The resulting plasma temperature is the same as in the 300 μs discharge. Peak pressure is 39.9 MPa, a small deviation from the 300 μs case. Total ablated mass increases in the longer discharge to 24.20 mg, an increase of 40.1%. If additional capillary ablated mass is needed, a longer discharge time can easily generate a larger amount of ablated mass. However, the total pressure increase for a longer discharge is negligible because the peak current is not any higher. The difference in peak pressure could be due solely to the uncertainty in determining the exact value, as discussed above.

Simulations run with capillaries of different lengths show the same behavior and percentage changes as the simulations presented above.

2.2.2 Total Deposited Energy

By varying the peak electrical current and internal capillary radius, the total energy deposited to the capillary can be changed. The total energy deposited to the capillary can be defined as

$$\frac{E}{\pi R^2} = \frac{V}{\pi R^2} \int_0^{t_f} I(t)dt, \tag{2.9}$$

where t_f is the pulse duration, here t_f =300 μs. The electrical energy is E, and the voltage across the capillary is defined as V. If constant voltage across the capillary for different current and radius pairs is assumed, the energy density per unit voltage (later referred to simply as the energy density) can be defined as $E_\rho = E/(V\pi R^2)$. Manipulating Eqn. 2.9, it can easily be shown that $E_\rho \propto I_{peak}/R^2$, under the assumption of a sinusoidal current profile. For fixed energy density we can vary the

internal radius and find the corresponding peak current via

$$I_{peakA} = I_{peakB} \left(\frac{R_A}{R_B} \right)^2, \tag{2.10}$$

where A and B refer to capillaries of two different radii and peak electrical currents, for which the total energy density is set equal.

A range of energy densities and internal radii are selected, and the peak electrical current is varied to match the selected energy density. The results of these simulations are shown in Table 2.2. The data for E1-E4 at R=1.6 mm is the same as that presented in Table 2.1 for the 10, 7, 5 and 3 kA cases, respectively. Contour plots of total capillary ablated mass and peak capillary outflow pressure are presented in Fig. 2.3 and Fig. 2.4, respectively. Note that via Eqn. 2.10, capillary radius and peak current are related by a scaling factor. Square boxes in Figs. 2.3 and 2.4 represent data points which correspond to data sets shown in Table 2.2. Contours are interpolated between these data points. One of the benefits of this model is the ease with which these figures can be generated. To reproduce this data via experimentation would be prohibitively time consuming and costly.

Figure 2.3 clearly indicates that the total ablated mass is not constant as a function of deposited energy. If it were, the contours shown in Fig. 2.3 would be horizontal lines. This non-linearity is due simply to Eqn. 2.10; as R_B increases so does I_{peakB} to maintain the constant energy density. As I_{peak} increases, the Joule heating increases as $Q_j \propto I_{peak}^2$, while the wall losses increase as $Q_F \propto I_{peak}$. Since Joule heating adds energy to the plasma, as Q_j increases, the wall temperature increases, thus increasing wall ablation. Hence at larger radius (which corresponds to a higher peak current) the total ablated mass is higher. Higher ablated mass results in higher capillary pressure, as the same trend can be seen in Fig. 2.4, though

Table 2.2: Results of the constant energy density study. For all cases ν=0.6, t_f=300 μs. Contours of M and P_{peak} are shown in Fig. 2.3 and 2.4, respectively.

Case	R(mm)	I_{peak}(kA)	E_ρ(J/Vm^2)	T(eV)	P_{peak}(MPa)	M(mg)
E1R4	1.4	7.65625	2.37×10^5	1.5	38.8	10.22
E1R5	1.5	8.78906	2.37×10^5	1.5	39.5	12.26
E1R7	1.7	11.28910	2.37×10^5	1.5	39.2	16.91
E1R8	1.8	12.65630	2.37×10^5	1.5	39.0	19.38
E2R4	1.4	5.35937	1.66×10^5	1.4	22.0	5.88
E2R5	1.5	6.15234	1.66×10^5	1.4	22.4	7.10
E2R7	1.7	7.90234	1.66×10^5	1.4	24.6	9.93
E2R8	1.8	8.85938	1.66×10^5	1.4	25.0	11.58
E3R4	1.4	3.82812	1.19×10^5	1.3	12.7	3.40
E3R5	1.5	4.39453	1.19×10^5	1.3	13.3	4.13
E3R7	1.7	5.64453	1.19×10^5	1.4	13.8	5.85
E3R8	1.8	6.32813	1.19×10^5	1.4	14.8	6.86
E4R4	1.4	2.29687	7.12×10^4	1.25	5.29	1.45
E4R5	1.5	2.63672	7.12×10^4	1.3	5.32	1.76
E4R7	1.7	3.38672	7.12×10^4	1.3	5.96	2.53
E4R8	1.8	3.79688	7.12×10^4	1.3	6.41	2.96
E5R4	1.4	6.44814	2.00×10^5	1.4	29.3	7.86
E5R5	1.5	7.40220	2.00×10^5	1.5	30.4	9.44
E5R6	1.6	8.42206	2.00×10^5	1.5	31.0	11.25
E5R7	1.7	9.50772	2.00×10^5	1.5	32.7	13.20
E5R8	1.8	10.65920	2.00×10^5	1.5	34.3	15.31

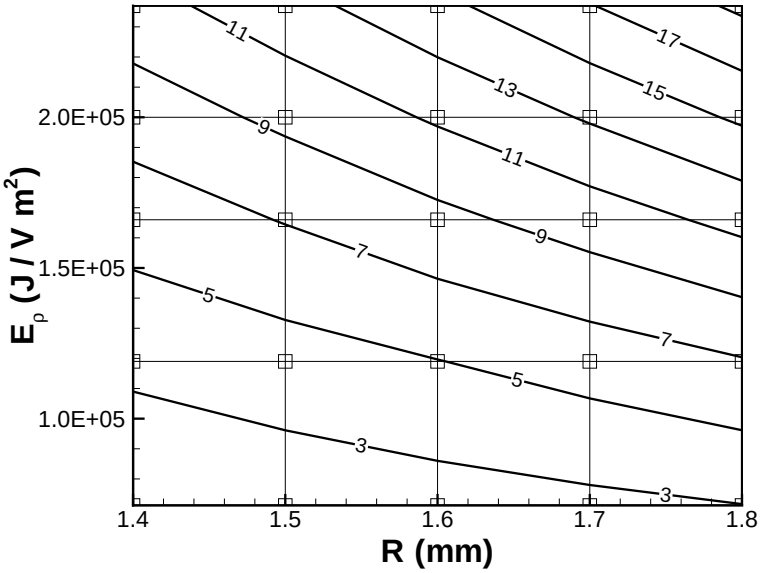

Figure 2.3: Total capillary ablated mass (M) in mg as a function of energy density and internal radius.

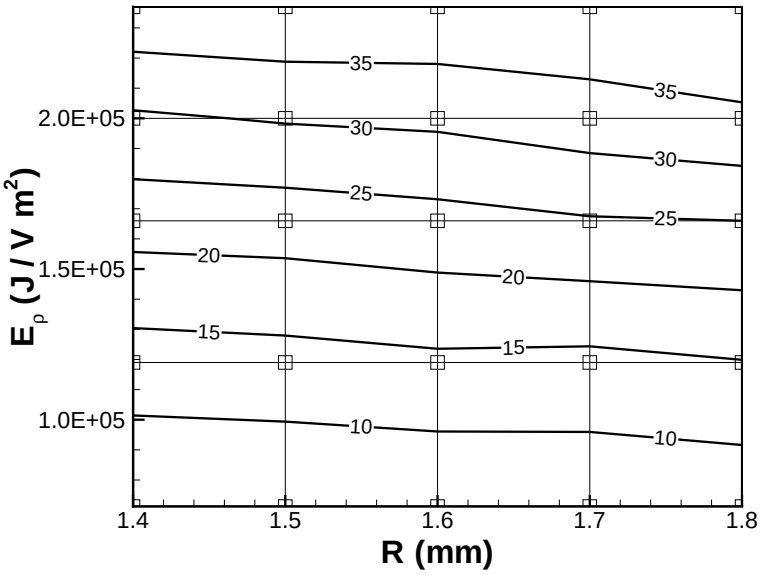

Figure 2.4: Peak capillary pressure (P_{peak}) in MPa as a function of energy density and internal radius.

less pronounced. Fluctuations in Fig. 2.4 are due to the difficulty in determining peak pressure from the simulation data, as discussed earlier. These results indicate that the largest ablated mass and peak pressure can be obtained at the lowest possible electrical energy by using a capillary with a large internal radius.

2.3 Variable Internal Radius

In reality, as the capillary wall material ablates, the internal radius will increase. This can be accounted for in the model via a time varying internal radius. At each time step, the radius is updated based on the total ablated mass from the previous time step. The time varying radius is given by

$$R(t) = \sqrt{\frac{M(t)}{\pi L \rho_s} + R_o^2}\ , \tag{2.11}$$

where R_o is the initial radius, $M(t)$ is the total ablated mass at time t, and $\rho_s = 0.95\times 10^3$ kg/m^3 is the density of polyethylene. A selection of representative simulations are rerun with the time varying radius to determine what effect the assumption of constant capillary radius has on the outflow data, the results of which are shown in Table 2.3. The changes in radius over the 300 μs discharge are typically less than 0.06 mm, or a 4% increase. Using a time varying radius decreases the total ablated mass, but typically by less than 1%. The decrease in outflow pressure ranged between $1-10\%$ when compared to the static radius results. It is concluded that for single use capillaries the assumption of static internal radius is valid.

Simulations are conducted to determine the effect that this change would have on restartable capillaries. Time varying radii are used for the reference capillary of Eqn. 2.8, with the restarted internal radius equal to the final radius of the previous run. The results of this study are shown in Table 2.4. After four firings, the ablated mass between the first and last discharge changed by less than 3.3%, the peak pressure

Table 2.3: Results of the variable internal radius study. For all cases ν=0.6.

I_{peak}(kA)	R_o(mm)	T(eV)	P_{peak}(MPa)	M(mg)
3	1.6	1.25	5.70	2.12
5	1.6	1.4	12.7	4.94
7	1.6	1.4	23.3	8.40
9	1.6	1.5	32.1	12.36
10	1.6	1.5	38.9	14.45

Table 2.4: Results of the restartable capillary study. For all cases I_{peak}=10 (kA), ν=0.6.

Run	R_o(mm)	T(eV)	P_{peak}(MPa)	M(mg)
1	1.6000	1.5	38.9	14.45
2	1.6572	1.5	36.8	14.25
3	1.7117	1.4	33.1	14.09
4	1.7639	1.4	29.1	13.98

dropped by 10 MPA, and the final radius is 1.8143 mm, a 12%. For this case, the pressure drop is approximately 25% of the initial peak pressure, which is a significant change. Current thinking in ETC gun design is to employ single use capillaries, thus this series of simulations is presented as an aside to the ETC model, but has relevance to related fields.

2.4 Simulating an Experimentally Tested Capillary

In Chapter III, the capillary model is used to generate the inflow to the CFD calculation. In the interest of consolidating all capillary model results and information, the inflow capillary used in Chapter III, and thus the rest of this work, is presented here.

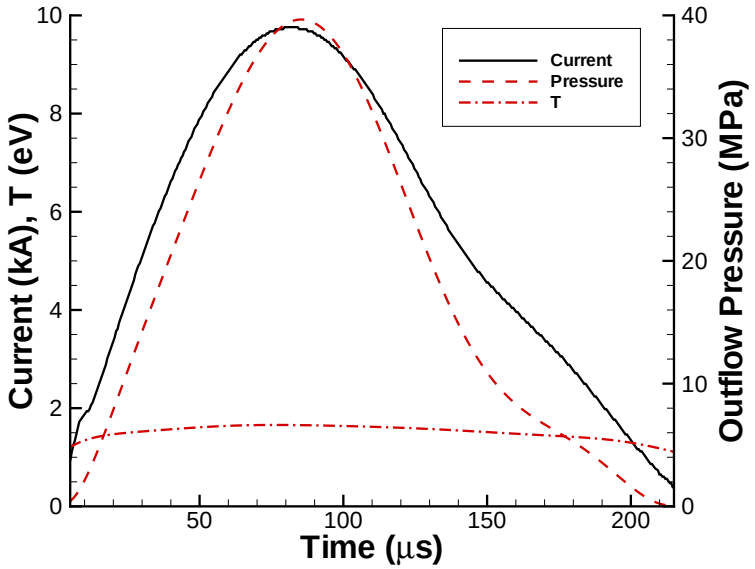

Figure 2.5: Experimental capillary electrical current (black) and polynomial fits to the resulting outflow (red) used in the CFD simulations of Chapters III and VI.

The electrical current profile used was obtained from the experiment is being simulated [6], and represents a discharge time of 220 μs with a peak current of nearly 10 kA occurring at roughly 85 μs. As in the reference capillary, L=26 mm and R=1.6 mm, with constant internal radius assumed. The current profile was extracted from the publication of Li *et al.*[6] via a data stripping code. The electric current input to the capillary model can therefore be considered exact. Figure 2.5 shows the data points for current obtained by the stripping code in black.

The red curves in Fig. 2.5 represent the polynomial fits to the capillary model results that are input into the CFD simulation as the inflow pressure and temperature. All species exit the capillary at a single plasma temperature, which is mostly time invariant at 1.5 eV. The exit boundary condition for the capillary model is sonic flow, with the velocity inflow of the CFD simulation given as $\sqrt{\gamma P/\rho}$. As will be seen and discussed in Chapter III, the CFD simulation is not sensitive to this condition, as the jet is a pressure driven flow.

Some of the polynomial fits to the capillary output give inaccurate values near the start and end of the simulation, so a 5 μs offset is used. This 5 μs is added back into the CFD simulation in post processing in order for the start times to more fully agree with the experiments.

2.5 Conclusions

A parametric study was conducted using a previously developed capillary plasma generator model tailored for electrothermal chemical gun application. Results indicated a linear correlation for most varied parameters, and the insignificance of other varied parameters in the range explored. A strong non-linear behavior exists in total ablated mass as functions of total deposited electrical energy and internal capillary radius, indicating that the most energy efficient way to increase the total capillary ablated mass is to use capillaries of larger internal radius. The use of a time varying internal capillary radius was also explored, the effects of which were found to be negligible for single use capillaries. The use of the capillary model to simulate an experimental capillary firing via the measured capillary discharge current was presented. The output from this experimental capillary simulation is used as inflow in the CFD simulation discussed in the next chapter.

CHAPTER III

Plasma-Air Chemistry

In order to perform accurate modeling of the plasma-propellant interaction it is necessary to know which species are reaching the propellant surface, as well as the density of the plasma. Knowledge of these two conditions is of key importance to modeling of the plasma-propellant interaction (Chapter IV). In both experimental setups and final implementation there is the possibility for some plasma-air interaction before the resulting species reach the propellant surface, introducing the possibility that the species coming from the plasma capillary and those interacting with the propellant are not the same. The present chapter develops a model to determine the effect plasma-air chemistry can have on the chemical composition of the plasma.

Previous work modeling the plasma-air interaction was conducted at the Army Research Laboratory. In one such simulation and matching experiment [22], a high pressure plasma jet was fired at a stagnation pressure probe 15 cm from the capillary inflow. Pressure versus time data were obtained and compared to the simulation. Although accurate pressure probe results were obtained, there are some problems with these previous simulations. The ARL model simulated 38 chemical species, including 16 ionic species. However, a detailed look at the chemistry model [23] shows that in the 57 reactions there are 12 species that are not included, 10 of which are ionic

species. Data were provided for species concentrations at locations between the capillary inflow and the pressure probe. A careful analysis of the species concentrations at the pressure probe shows that there is a strong deviation from quasi-neutrality [22]. The most likely reason for this is that the electrons diffused away at high speed in the simulation. However, since the ARL model contains no electromagnetic terms in the equations governing the fluid calculations, this deviation from quasi-neutrality should not have an effect on the ion flow. What makes the results questionable is that the missing electrons will have an effect on the recombination rates near the pressure probe, since there will not be enough electrons to allow ions to recombine. The CFD code used in this thesis is designed to simulate quasi-neutral plasma flows, with an electron diffusion model that maintains quasi-neutrality [24]. In all the simulations presented here the deviation from quasi-neutrality was less than 0.01% everywhere. Since the ARL study was the previous major effort in this field, for the above reasons this problem warranted a second look.

Recent experiments of Li *et al.* [6, 7] have investigated the plasma-air chemistry and the plasma jet in some detail. These experiments include stagnation pressure probe results for a range of capillary-probe distances, propellant sample analysis at a range of capillary-sample distances, sequential photographs of the plasma jet interaction for these cases, and sampling the chemical species present in the jet. The conditions of these recent experiments serve as the basis for the simulations (Case S1 and Case S2) presented in this chapter.

An overview of the chemically reacting CFD code used for this work, LeMANS, is discussed. Then an overview of the experiments and how they are adapted to simulation is shown. Results and discussion for Cases S1 and S2 are then presented. An abbreviated chemistry model is highlighted, based on the results of simulations,

which yields faster computational times. Finally, a practical ETC configuration is simulated and conclusions are drawn concerning plasma-air chemistry from these three simulations. Much of the data and results presented in this chapter first appeared in [21].

3.1 LeMANS Overview

The computational fluid dynamics code used throughout this thesis, LeMANS, was developed by Leonardo Scalabrin at the University of Michigan Department of Aerospace Engineering. It is a chemically reacting, parallelized, implicit Navier-Stokes CFD code using a modified Steger-Warming Flux Vector Splitting scheme for calculation of inviscid fluxes between mesh volumes, is second order accurate in space, and for the purposes of this thesis time integration is performed using a point implicit method. The code is first order accurate in time, thus a small timestep and CFL number are used to ensure accuracy [25]. LeMANS was designed to accommodate quasi-neutral plasma flows, where electron mobility is limited to ensure quasi-neutrality [24]. For ETC application, LeMANS was modified to allow for time varying boundary conditions, namely the capillary plasma inflow. This work represents the first time LeMANS has been used for time accurate or internal flows. The temporal accuracy of LeMANS was verified by simulation of shock tube cases and comparison to an exact Riemann Solver.

Presented here is an overview of some of the models contained in LeMANS that were used throughout this thesis. Complete details of the code can be found elsewhere [26, 27, 28]. The viscosity of the fluid is modeled by

$$\mu = \sum_s \frac{X_s \mu_s}{\phi_s}, \tag{3.1}$$

where X_s is the species mole fraction, and μ_s is the species coefficient of viscosity,

modeled as

$$\mu_s = 0.1 \exp[(A_s \ln T + B_s) \ln T + C_s], \tag{3.2}$$

where A_s, B_s and C_s are constants fit to experimental data. The term ϕ_s in Eqn. 3.1 is given by

$$\phi_s = \sum_r \left[1 + \sqrt{\frac{\mu_s}{\mu_r}} \sqrt[4]{\frac{\mathrm{MW}_r}{\mathrm{MW}_s}} \right]^2 \left[\sqrt{8 \left(1 + \frac{\mathrm{MW}_s}{\mathrm{MW}_r} \right)} \right]^{-1}, \tag{3.3}$$

where MW_s is the species molecular weight [26].

Forward chemical reaction rates are modeled as

$$k_f = C T^{\eta} \exp(-\theta / T), \tag{3.4}$$

where C, η and θ are constants fit to experimental data. Backward reaction rates are represented as

$$k_b = \frac{k_f}{K_{eq}}, \tag{3.5}$$

where K_{eq} is the temperature dependent equilibrium constant, modeled as

$$K_{eq} = \exp \left[A_1 \left(\frac{T}{10^5} \right) + A_2 + A_3 \ln \left(\frac{10^5}{T} \right) + A_4 \left(\frac{10^5}{T} \right) + A_5 \left(\frac{10^5}{T} \right)^2 \right], \tag{3.6}$$

where A_1-A_5 are again constants fit to experimental data, or theoretical expansions of partition functions [26]. These final three equations are used to model the chemical reactions outlined in the next section.

3.2 Plasma-Air Chemistry Model

The chemistry model developed is built upon previous work, both theoretical and experimental, on plasma-air chemistry for ETC application. LeMANS was originally designed for simulating hypersonic flow around reentry vehicles, and uses Park's model [29] for nitrogen-oxygen chemistry, the same model used by NASA [27]. Due

to the wide use of this model, it is utilized for all nitrogen-oxygen chemistry in the ETC chemistry model. Additional species are chosen based on the abundances from the ARL simulations [22], where species with high abundances are chosen first. Due to a desire to compare with the recent measurements of Li *et al.* on plasma species present in the jet [7], many of the more abundant detected species are added. As a final step, species are added that are needed for extended chemical mechanisms. For instance, to go from H to H_2O the species OH should be added to the model to allow for a less direct reaction path. The total number of species is kept to a minimum to decrease computational expense as the needed resources and computational time can rapidly go beyond practical limits.

The model arrived at contains 26 chemical species and 60 reactions. The first eleven species are from Park's model, namely N_2, O_2, NO, N, O, NO^+, N_2^+, O_2^+, N^+, O^+, and electrons (e). The remaining species are OH, CO, CO_2, H_2O, C_2H_2, C_2H_3, CH, CH_2, HCO, NH, H_2, C, C^+, H, and H^+. The C_xH_y compounds are added because the experiments detected a significant amount of these species [7].

The reaction rate data is obtained from the GRI-Mech project for all chemistry not included in Park's model [30]. The GRI-Mech data is used in several commercially available hydrocarbon chemistry software packages, including the CHEMKIN software. For the hydrogen and carbon ionization reactions the work of Chang and Ordonez [31, 32] was employed. Table 3.1 presents a complete list of all reactions used in the simulation. Some of the third body reactions, indicated by the presence of species M, have different reaction rates for a certain M. These species specific rates are also incorporated into LeMANS. All the reactions used have accompanying backward reactions, defined by Eqns. 3.5 and 3.6.

Reaction rate constants, defined in Eqn. 3.4, are listed in Tables 3.2–3.5. The

Table 3.1: Reactions employed in the chemistry model.

Number	Reaction	Number	Reaction
1	$O+H+M \rightarrow OH+M$	31	$HCO+M \rightarrow H+CO+M$
2	$O+H_2 \rightarrow H+OH$	32	$N+OH \rightarrow NO+H$
3	$O+CH \rightarrow H+CO$	33	$NH+O \rightarrow NO+H$
4	$O+CH_2 \rightarrow H+HCO$	34	$NH+H \rightarrow N+H_2$
5	$O+CO+M \rightarrow CO_2+M$	35	$NH+OH \rightarrow N+H_2O$
6	$O+HCO \rightarrow OH+CO$	36	$NH+O_2 \rightarrow NO+OH$
7	$O+HCO \rightarrow H+CO_2$	37	$NH+N \rightarrow N_2+H$
8	$O+C_2H_2 \rightarrow CO+CH_2$	38	$NH+NO \rightarrow N_2+OH$
9	$O_2+CO \rightarrow O+CO_2$	39	$C+NO \rightarrow CO+N$
10	$H+O_2 \rightarrow O+OH$	40	$N+CO_2 \rightarrow NO+CO$
11	$2H+M \rightarrow H_2+M$	41	$CH_2+O_2 \rightarrow 2H+CO_2$
12	$H+OH+M \rightarrow H_2O+M$	42	$2CH_2 \rightarrow 2H+C_2H_2$
13	$H+CH \rightarrow C+H_2$	43	$H+e \rightarrow 2e+H^+$
14	$H+HCO \rightarrow H_2+CO$	44	$C+e \rightarrow 2e+C^+$
15	$H+C_2H_3 \rightarrow H_2+C_2H_2$	45	$O_2+M \rightarrow 2O+M$
16	$OH+H_2 \rightarrow H+H_2O$	46	$N_2+M \rightarrow 2N+M$
17	$2OH \rightarrow O+H_2O$	47	$NO+M \rightarrow N+O+M$
18	$OH+C \rightarrow H+CO$	48	$NO+O \rightarrow O_2+N$
19	$OH+CH \rightarrow H+HCO$	49	$N_2+O \rightarrow NO+N$
20	$OH+CH_2 \rightarrow CH+H_2O$	50	$O_2^+ + N \rightarrow O_2+N^+$
21	$OH+CO \rightarrow H+CO_2$	51	$NO+O^+ \rightarrow O_2+N^+$
22	$OH+HCO \rightarrow H_2O+CO$	52	$NO^+ + O \rightarrow N^+ + O_2$
23	$OH+C_2H_3 \rightarrow H_2O+C_2H_2$	53	$N_2+O^+ \rightarrow N_2^+ + O$
24	$C+O_2 \rightarrow O+CO$	54	$NO^+ + O_2 \rightarrow NO+O_2{}^+$
25	$CH+O_2 \rightarrow O+HCO$	55	$NO^+ + N \rightarrow N_2{}^+ + O$
26	$CH+H_2 \rightarrow H+CH_2$	56	$N+O \rightarrow NO^+ + e$
27	$CH+CH_2 \rightarrow H+C_2H_2$	57	$2O \rightarrow O_2{}^+ + e$
28	$CH+CO_2 \rightarrow HCO+CO$	58	$2N \rightarrow N_2{}^+ + e$
29	$CH_2+O_2 \rightarrow OH+H+CO$	59	$O+e \rightarrow O^+ + 2e$
30	$2CH_2 \rightarrow H_2+C_2H_2$	60	$N+e \rightarrow N^+ + 2e$

Table 3.2: Reaction rates for reactions 2–30 from Table 3.1, excluding third body reactions.

Number	C	η	θ
2	3.87×10^{4}	2.7	3150.16
3	5.70×10^{13}	0.0	0.0
4	8.00×10^{13}	0.0	0.0
6	3.00×10^{13}	0.0	0.0
7	3.00×10^{13}	0.0	0.0
8	6.94×10^{6}	2.0	959.119
9	2.50×10^{12}	0.0	24053.9
10	2.65×10^{16}	-0.7	8575.38
13	1.65×10^{14}	0.0	0.0
14	7.34×10^{13}	0.0	0.0
15	3.00×10^{13}	0.0	0.0
16	2.16×10^{8}	1.5	1726.05
17	3.57×10^{4}	2.4	-1061.8
18	5.00×10^{13}	0.0	0.0
19	3.00×10^{13}	0.0	0.0
20	1.13×10^{7}	2.0	1509.66
21	4.76×10^{7}	1.2	35.2254
22	5.00×10^{13}	0.0	0.0
23	5.00×10^{12}	0.0	0.0
24	5.80×10^{13}	0.0	289.855
25	6.71×10^{13}	0.0	0.0
26	1.08×10^{14}	0.0	1565.02
27	4.00×10^{13}	0.0	0.0
28	1.90×10^{14}	0.0	7946.86
29	5.00×10^{12}	0.0	754.831
30	1.60×10^{15}	0.0	6010.47

Table 3.3: Reaction rates for reactions 32–60 from Table 3.1, excluding third body reactions.

Number	C	η	θ
32	3.36×10^{13}	0.0	193.74
33	4.00×10^{13}	0.0	0.0
34	3.20×10^{13}	0.0	166.063
35	2.00×10^{9}	1.2	0.0
36	1.28×10^{6}	1.5	50.3221
37	1.50×10^{13}	0.0	0.0
38	2.16×10^{13}	-0.2	0.0
39	2.90×10^{13}	0.0	0.0
40	3.00×10^{12}	0.0	5686.39
41	5.80×10^{12}	0.0	754.831
42	2.00×10^{14}	0.0	5529.89
43	9.98×10^{14}	0.29	164202.0
44	7.32×10^{14}	0.41	146581.0
48	8.40×10^{12}	0.0	19450.0
49	6.40×10^{17}	-1.0	38400.0
50	8.70×10^{13}	0.14	28600.0
51	1.40×10^{5}	1.9	15300.0
52	1.00×10^{12}	0.5	77200.0
53	9.10×10^{11}	0.36	22800.0
54	2.40×10^{13}	0.41	32600.0
55	7.20×10^{13}	0.0	35500.0
56	5.30×10^{12}	0.0	31900.0
57	1.10×10^{13}	0.0	80600.0
58	2.00×10^{13}	0.0	67500.0
59	3.90×10^{33}	-3.78	158500.0
60	2.50×10^{34}	-3.82	168600.0

Table 3.4: Reaction rates for GRI-Mech third body reactions from Table 3.1.

Number	M	C	η	θ
1	CO	7.50×10^{17}	-1.0	0.0
1	CO_2	1.00×10^{18}	-1.0	0.0
1	H_2	1.00×10^{18}	-1.0	0.0
1	H_2O	3.00×10^{18}	-1.0	0.0
1	M	5.00×10^{17}	-1.0	0.0
5	O_2	1.80×10^{11}	0.0	1200.18
5	CO	2.70×10^{10}	0.0	1200.18
5	CO_2	6.30×10^{10}	0.0	1200.18
5	H_2	3.60×10^{11}	0.0	1200.18
5	H_2O	1.80×10^{11}	0.0	1200.18
5	M	1.80×10^{10}	0.0	1200.18
11	H_2	9.00×10^{16}	-0.6	0.0
11	H_2O	6.00×10^{19}	-1.2	0.0
11	CO_2	5.50×10^{20}	-2.0	0.0
11	M	1.00×10^{18}	-1.0	0.0
12	H_2	1.61×10^{22}	-2.0	0.0
12	H_2O	8.03×10^{22}	-2.0	0.0
12	M	2.20×10^{22}	-2.0	0.0
31	H_2	3.74×10^{18}	-1.0	8554.75
31	H_2O	1.50×10^{18}	-1.0	8554.75
31	CO	2.80×10^{18}	-1.0	8554.75
31	CO_2	3.74×10^{18}	-1.0	8554.75
31	M	1.87×10^{18}	-1.0	8554.75

Table 3.5: Reaction rates for Park's model third body reactions from Table 3.1.

Number	M	C	η	θ
45	N_2	2.00×10^{21}	-1.5	59500.0
45	O_2	2.00×10^{21}	-1.5	59500.0
45	NO	2.00×10^{21}	-1.5	59500.0
45	N_2^+	2.00×10^{21}	-1.5	59500.0
45	O_2^+	2.00×10^{21}	-1.5	59500.0
45	NO^+	2.00×10^{21}	-1.5	59500.0
45	M	1.00×10^{22}	-1.5	59500.0
46	N_2	7.00×10^{21}	-1.6	113200.0
46	O_2	7.00×10^{21}	-1.6	113200.0
46	NO	7.00×10^{21}	-1.6	113200.0
46	N_2^+	7.00×10^{21}	-1.6	113200.0
46	O_2^+	7.00×10^{21}	-1.6	113200.0
46	NO^+	7.00×10^{21}	-1.6	113200.0
46	M	3.00×10^{22}	-1.6	113200.0
47	N_2	5.00×10^{15}	0.0	75500.0
47	O_2	5.00×10^{15}	0.0	75500.0
47	NO	5.00×10^{15}	0.0	75500.0
47	N_2^+	5.00×10^{15}	0.0	75500.0
47	O_2^+	5.00×10^{15}	0.0	75500.0
47	NO^+	5.00×10^{15}	0.0	75500.0
47	M	1.10×10^{17}	0.0	75500.0

Table 3.6: Equilibrium rate constants for reactions 2–30 from Table 3.1, excluding third body reactions.

Number	A_1	A_2	A_3	A_4	A_5
2	-0.351228	1.08616	-0.194031	-0.0765602	-0.000286077
3	-1.30351	-3.08199	-0.384687	8.91859	-0.000313876
4	-0.62088	-0.999888	-0.604653	4.64268	-0.000579195
6	-0.00928796	-1.5696	0.746125	4.28643	0.000776025
7	-1.43896	-4.3829	-1.12929	5.67325	-0.000421468
8	-1.70837	1.49545	1.03604	2.2988	0.000289522
9	-0.376745	-1.27512	-1.03356	0.468782	-0.000474064
10	-1.78086	3.46037	-0.718546	-0.649807	-0.00656168
13	-1.39263	-0.864873	-0.00647235	1.17764	0.000132626
14	-0.147036	-2.34202	0.760971	4.37946	0.000858592
15	-1.15832	-1.37501	0.226756	3.40042	0.00116991
16	1.29848	-1.94904	0.0264527	0.792384	-0.000518721
17	0.999277	-2.65118	0.0122282	0.886838	-0.000445049
18	-1.61089	-2.19983	-0.743523	7.86138	-0.000651774
19	-3.3583	-0.433783	-1.65856	4.67017	-0.00147741
20	3.12464	-2.87985	0.886686	0.874277	0.000283299
21	-0.821907	-3.16324	-1.69889	1.37399	-0.00107248
22	1.98431	-4.73665	1.01006	5.15517	0.000517923
23	1.05701	-3.80395	0.495333	4.17373	0.000865654
24	0.541703	-1.19974	0.347929	6.9267	0.000237861
25	-1.09958	0.490681	-0.522068	3.7317	-0.000547733
26	-1.97232	1.04278	-0.951373	-0.0673619	-0.00110605
27	-1.62768	-3.52871	-1.92231	6.65413	-0.000934824
28	-0.98942	1.89316	0.457055	3.26574	-0.0000973058
29	0.0	500.0	0.0	0.0	0.0
30	-0.504163	-4.06352	-1.27508	6.75462	-0.00035718

Table 3.7: Equilibrium rate constants for reactions 32–60 from Table 3.1, excluding third body reactions.

Number	A_1	A_2	A_3	A_4	A_5
32	-0.348807	-0.509057	-0.486089	2.47538	-0.000352302
33	-1.38048	-0.751899	-0.68022	3.62247	-0.000534026
34	-0.690722	-1.29983	-0.0337205	1.22956	2.47824×10^{-6}
35	0.765271	-3.35137	0.0544086	2.01571	-0.000435789
36	0.368898	0.439737	0.329541	2.69236	0.0003161
37	-0.425539	-2.89129	-0.276394	7.37666	-0.000201801
38	0.378745	-2.64929	0.351111	4.88988	0.000274091
39	0.914104	-2.86214	0.332784	5.34076	0.00019254
40	4.44493	0.285176	2.60359	0.970923	0.00260831
41	0.0	500.0	0.0	0.0	0.0
42	0.0	500.0	0.0	0.0	0.0
43	-0.967090	-3.397600	-2.340800	-16.64200	-0.0104770
44	-0.967090	-3.397600	-2.340800	-16.64200	-0.0104770
48	-0.002428	-1.741500	-1.233100	-0.953650	-0.045850
49	0.969210	0.893290	0.735310	-3.959600	0.006818
50	-2.596000	2.302100	-3.574400	-1.526400	-0.080816
51	-1.635500	0.830580	-2.995200	-1.379400	-0.079927
52	-0.884720	1.425400	-2.039800	-6.873100	-0.056184
53	-1.618100	2.556200	-3.282300	-0.937210	-0.075176
54	1.713900	0.864690	2.767900	-4.393200	0.070493
55	-1.836500	2.257700	-3.062200	-2.471300	-0.058248
56	-0.528010	-7.328100	-1.926400	-3.261800	0.018540
57	1.183500	-8.204900	-0.391460	-8.608700	0.043187
58	-2.364400	-5.070400	-4.988500	-5.733200	-0.039703
59	0.6647800	-5.971600	-0.584860	-16.21200	0.0232730
60	-0.967090	-3.397600	-2.340800	-16.64200	-0.0104770

Table 3.8: Equilibrium rate constants for third body reactions from Table 3.1.

Number	A_1	A_2	A_3	A_4	A_5
1	2.75849	-2.24859	0.894633	5.08351	0.000121692
5	1.47278	-5.15994	-0.92114	6.46437	-0.000996995
11	2.29871	-2.86083	0.826899	5.1835	0.000125285
12	4.30112	-5.18843	1.04764	5.96046	-0.000224511
31	0.850793	-1.56074	1.42589	-1.02846	0.00630212
45	0.509890	2.477300	1.713200	-6.544100	0.029591
46	1.476600	1.629100	1.215300	-11.457000	-0.009444
47	0.507650	0.735750	0.480420	-7.497900	-0.016247

parameters C, η, and θ are such that they return k_f in SI units when temperature is in Kelvin. Equilibrium constant fit parameters, defined in Eqn. 3.6, are listed in Tables 3.6–3.8, and are such that K_{eq} is in SI units when temperature is in Kelvin.

Thermodynamic data for each species, such as specific heat and enthalpy of formation, are obtained from GRI-Mech or Field and Franklin [33]. Viscosity data for each species are obtained from McBride and Gordon [34]. These values are listed in Table 3.9, with viscosity in SI units when temperature is in Kelvin. The viscosity for electrons is not given, as LeMANS uses an electron mobility limiter to ensure quasi-neutrality.

Although LeMANS is capable of accommodating a two temperature model, representing translation and vibration, sufficient information could not be found for all chemical species to use this approach. More importantly, due to the high temperatures involved in these flows the translational and vibrational temperatures are nearly equilibrated, rendering a two temperature model largely unnecessary.

Table 3.9: Formation enthalpy ($h_{f,o}$), viscosity fit coefficients (A_s, B_s, C_s) from Eqn. 3.2, and specific heat (C_v) for the 26 species chemistry model.

Species	$h_{f,o}$ (J/kg)	A_s	B_s	C_s	C_v (J/kgK)
N_2	0.0	0.0268142	0.3177838	-11.3155513	445.39
O_2	0.0	0.0449290	-0.08261580	-9.20194750	389.72
NO	2.996123×10^6	0.0436378	-0.03355110	-9.57674300	415.70
N	3.362161×10^7	0.0115572	0.6031679	-12.4327495	890.79
O	1.543119×10^7	0.0203144	0.4294404	-11.6031403	779.44
NO^+	3.283480×10^7	0.302014	-3.5039791	-3.73551570	415.70
N_2^+	5.425897×10^7	0.0268142	0.3177838	-11.3155513	445.39
O_2^+	3.658450×10^7	0.0449290	-0.08261580	-9.20194750	389.72
N^+	1.340460×10^8	0.0115572	0.6031679	-12.4327495	890.79
O^+	9.770599×10^7	0.0203144	0.4294404	-11.6031403	779.44
OH	2.31351×10^6	-0.0797322	2.02509	-17.8822	1268.28
CO	-3.9479×10^6	0.0509243	-0.0904635	-9.58362	744.624
CO_2	-8.9433×10^6	-0.0145015	0.891184	-13.2516	655.475
H_2O	-1.34353×10^7	-0.0874392	2.16337	-18.6426	1404.7
C_2H_2	8.77674×10^6	-0.0124719	0.850745	-13.4664	1373.18
C_2H_3	1.11015×10^7	-0.0124719	0.850745	-13.4664	1274.28
CH	4.595×10^7	-0.0874392	2.16337	-18.6426	1603.81
CH_2	2.80238×10^7	-0.0874392	2.16337	-18.6426	1907.65
HCO	1.44853×10^6	-0.0874392	2.16337	-18.6426	906.506
NH	2.3793×10^7	-0.0874392	2.16337	-18.6426	1392.75
H_2	0.0	0.0617707	-0.202077	-10.0344	10257.4
C	5.97231×10^7	0.00990234	0.602879	-12.7238	1043.61
C^+	1.50275×10^8	0.00990234	0.602879	-12.7238	1043.61
H	2.17986×10^8	-0.0148088	1.06893	-15.5487	12481.5
H^+	1.53134×10^9	-0.0148088	1.06893	-15.5487	12481.5
e^-	0.0	-	-	-	0.0

3.3 Simulation Methodology

The first two simulations (Case S1 and S2) presented are based directly on experiments. In each experiment, an identical plasma capillary with nearly identical current load was used. Identical capillaries and current loads allow for the use of one capillary input for each simulation, thus the main difference between the two simulations is the geometry. The simulation of this capillary is discussed in Section 2.4.

The first experiment [6] fired the plasma into an open chamber at 1 atm pressure. Five pressure sensors were implanted at 9.5 mm intervals in a wall 40 mm away, oriented parallel to the exit plane of the capillary. The first pressure sensor was aligned with the capillary exit at the stagnation line, this sensor was labeled P0. Each subsequent sensor was labeled P1-P4, with P4's center being 38 mm above the capillary centerline.

Before entering the chamber the capillary plasma travels through a cylindrical nozzle 1.6 mm in radius and 13 mm in length [6]. Since the flow variables could change in this distance, the nozzle flow is also simulated. The simulation uses an axisymmetric geometry, with the outflow at y=50 mm, and walls at x=13 mm and x=53 mm. The latter wall contains the five pressure sensors. Pressure versus time data are output at the five "pressure sensors" in the simulation. The P0 sensor is the first wall cell above the symmetry plane, with P1-P4 extracted from wall cells at positions y=9.5 mm, 19 mm, 28.5 mm, and 38 mm, respectively. This simulation is labeled below as Case S1.

In the second experiment [7], the capillary plasma was injected into a cylindrical plasma holding chamber of radius 9.4 mm and 129.5 mm length [8]. Gas escaped the

plasma holding chamber through a 0.5 mm radius nozzle into a 10x10x10 cm chamber that housed a mass spectrometer probe to measure the species present in the plasma [7]. The plasma holding chamber was employed in the experiment because the plasma jet washed over the probe too rapidly for any measurements to be made, thus the flow had to be slowed down. Chemical abundances, in terms of arbitrary intensity units, of some species were measured by the mass spectrometer probe. These arbitrary units make it difficult for exact comparisons to be made, however qualitative comparisons are possible that yield much insight. The simulation of this flow, labeled below as Case S2, has the geometry listed above, with the change that the expansion chamber after the secondary nozzle is not encumbered by the measurement apparatus. This allows for a more direct comparison of the jets in Case S1 and Case S2.

It must be noted that in an attempt to decrease heat loss to the walls, the holding chamber in the experiment was lined with polyethylene. However, there is evidence that this liner ablated as far as 50 mm from the primary nozzle with a total mass loss three to five times that of the mass loss from the capillary [7]. To see what effect this had, the experimenters replaced the polyethylene liner with one of identical dimensions made of aluminum. Their results show that only CO intensity could be accurately measured, with all other chemical species being within the noise level of the measurement [7]. Essentially, by using a polyethylene liner, the same compound that is ablating in the capillary to form the plasma, the experimenters created a much larger capillary. The higher mass loss due to this wall ablation increases the abundance of carbon and hydrogen in the plasma holding chamber, allowing new reaction mechanisms to occur. This may explain the high abundance of C_xH_y detected in the experiment. The present simulation does not include this ablating holding chamber, and can be thought of as the case with the aluminum

liner.

These two simulations allow for some key comparisons to be made concerning the chemistry of the plasma-air interaction. Since the capillary is identical in both experiments, and hence in both simulations, it is possible to compare the chemistry of the primary jet of Case S1 to that of the secondary jet of Case S2, to see the full effect that the holding chamber had. Also, simulating the secondary jet without wall ablation illuminates how the polyethylene liner skewed the results of the mass spectrometer data.

3.3.1 Case S1

Due to the large computational expense of running a 26 species, chemically reacting CFD simulation, grid convergence was found first for a single species non-chemically reacting flow. This single species had the same inflow temperature, velocity and pressure profile as the full simulation. Grid convergence is based on the arrival time of the pressure pulse at P0, the value of the peak pressure, and the behavior of the pressure profile just beyond the peak. Case S1 uses rectangular cells with a uniform cell spacing of Δx=0.1 mm, which results in 202,080 cells. Case S1 ran on thirty 2 GHz processors with a timestep of $\Delta t = 2.5 \times 10^{-9}$ s, having a total runtime of 296 hours to simulate 70 μs of real time.

Snapshots of Mach number contours for Case S1 are shown in Fig. 3.1, where t=0 μs is at the start of the current profile in Fig. 2.5. The data from t=35 μs is used for detailed examination of the chemistry. At this time the jet is fully developed, the precursor shock can clearly be seen, and the jet has not yet begun interacting with the wall. Evaluating the chemistry at this time will allow for a much more direct comparison with the secondary jet chemistry of Case S2.

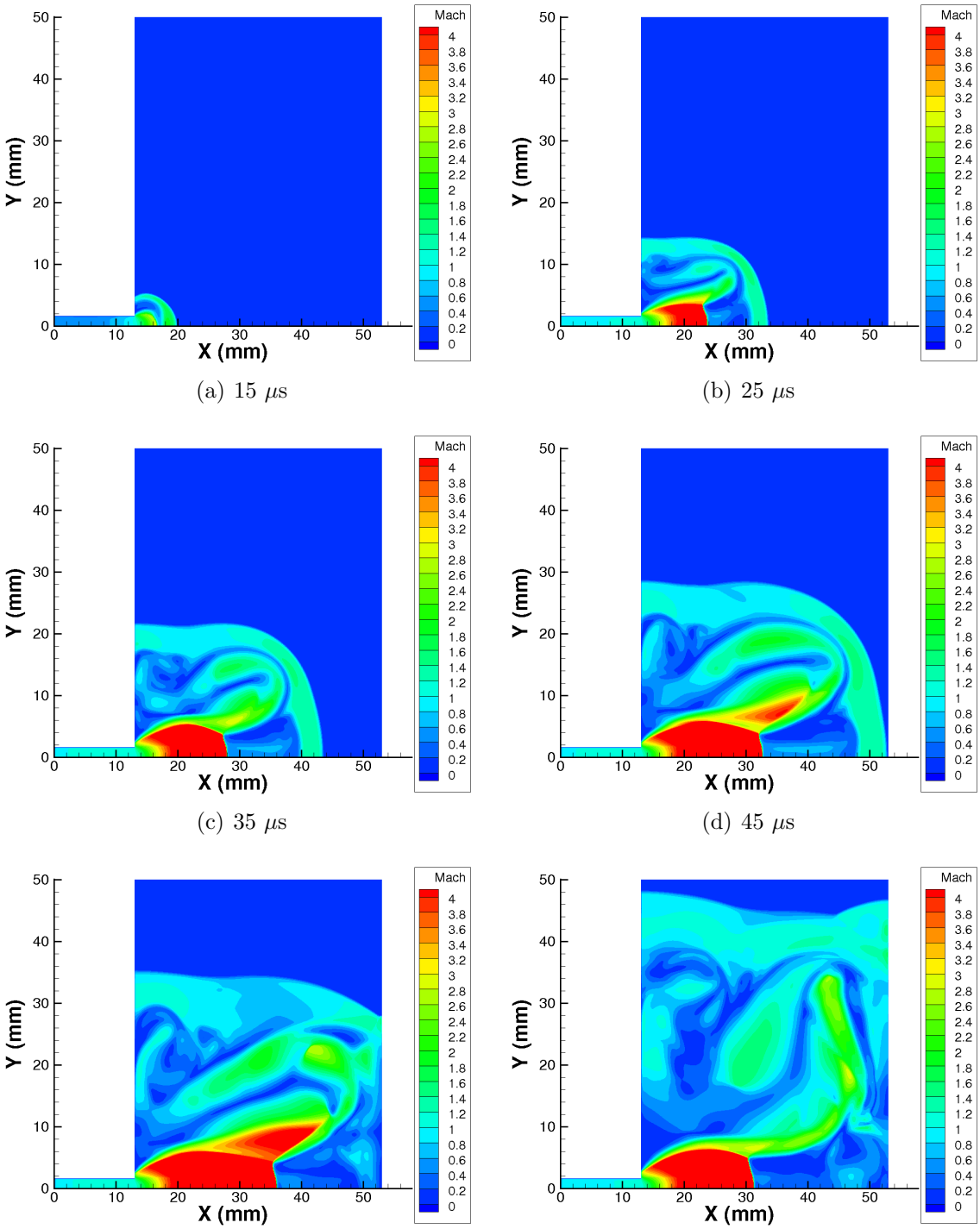

(a) 15 μs

(b) 25 μs

(c) 35 μs

(d) 45 μs

(e) 55 μs

(f) 74 μs

Figure 3.1: Snapshots of Mach number for Case S1.

The work at ARL simulating the plasma jet documented the expected structure of the jet exiting the capillary nozzle. Figure 3.2, and the accompanying description, are taken from [22].

> The efflux of plasma from the inlet generates a weak precursor shock (A) that expands spherically. Behind this shock is air; the plasma is entirely contained by this shock and is separated from the air by an irregularly shaped contact surface (B) across which pressure and velocity are preserved, but entropy changes discontinuously. Expansion waves (C), generated at the inlet, travel to the precursor shock (A), are reflected as weak compression waves, and coalesce into a strong oblique shock or barrel shock (D) within the plasma jet. This barrel shock (D) terminates in an irregular reflection that forms a triple-point (E), joining the barrel shock (D), it's reflection (F), and a normal shock (G) or Mach disk. Whereas the precursor shock (A) is relatively weak and diffuse, producing a mildly supersonic flow, the barrel shock (D) and Mach disk (G) are strong shocks that enclose a fully supersonic flow region. [22]

A number of these features are clearly visible in contour plots for Case S1. The precursor shock (A) can clearly be seen in Figs. 3.1b-d. The expansion region (C) is clearly visible in Figs. 3.1c-f. The barrel shock/Mach disk structure, (D) and (G), has clear and definite form in Figs. 3.1b-d, with the region contained being clearly supersonic. As will be discussed later, Fig. 3.5a illustrates the reaction region which is associated with contact surface (B).

Pressure versus time data are shown in Fig. 3.3. Experimental data indicates that the precursor shock should arrive at P0 at approximately t=60 μs, and have a peak of 1.4 MPa. The width at half height for the experimental profile at P0 is

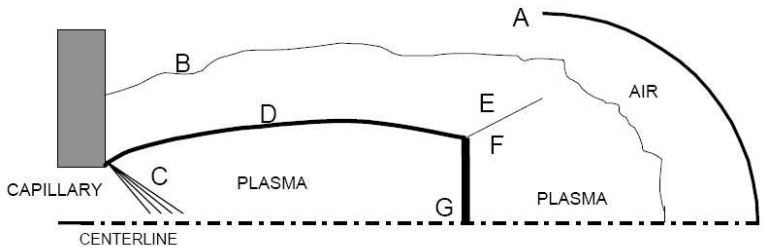

Figure 3.2: Diagram of the expected gas dynamic features of the expanding capillary plasma jet, taken from [22].

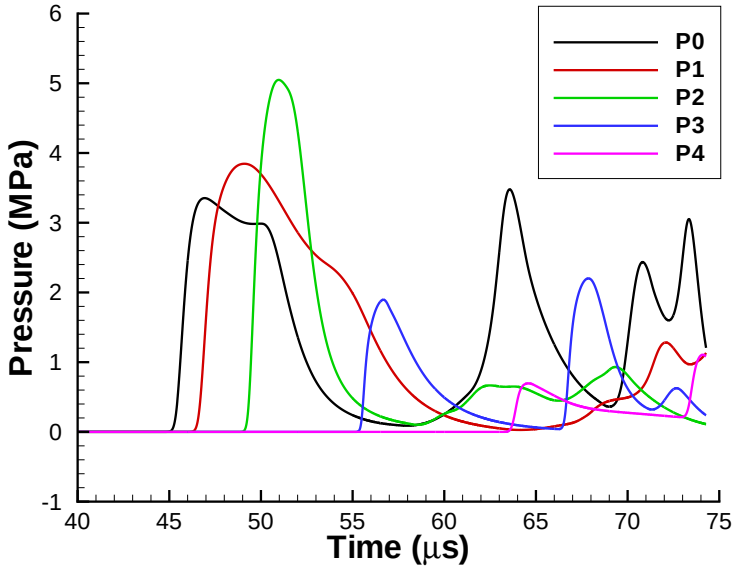

Figure 3.3: Pressure versus time at the five pressure sensors for Case S1.

approximately 20 μs [6]. Case S1 gives a P0 arrival time of 45 μs, a peak of 3.2 MPa and width of approximately 7 μs. Experimental data exists for the chamber pressure versus time in the plasma holding chamber of Case S2 [7]. The experiment shows a peak pressure of around 2.5 MPa, whereas Case S2 indicates that chamber pressure can reach more than twice that. These data indicate that perhaps the capillary model is overestimating the pressure. As discussed in Chapter II, there is no experimental data available for the capillary outflow pressure. Thus evaluation of this hypothesis can not be directly performed at this time.

In terms of the pressure pulse arriving early in Case S1 there is a possible expla-

nation beyond the overestimation of the capillary pressure. A change of slope in the current profile is visible in Fig. 2.5 at approximately 10 μs. In a typical capillary, an exploding wire is used to create the initial plasma used to trigger the self-sustaining ablation, and this bump is due to the wire exploding [6]. The capillary code does not model the exploding wire, and instead initializes with a plasma density typical of an exploding wire plasma. With this initial density the capillary begins ablation within the first 3 μs of the simulation due to the high current load. It is possible that the correct start time would be after the wire explodes, adding a further shift of 10-15 μs. This demonstrates how difficult it can be to estimate the start time in this type of simulation. Experimentally it is logical to measure time from the initiation of the current pulse, however, the initiation of the current pulse may not correspond to the start of capillary ablation on a timescale of a few microseconds. Further work may be needed to more accurately determine the delay time between initiation of the current pulse and the start of capillary ablation.

Pressure and temperature contours for Case S1, taken at t=35 μs, are shown in Fig. 3.4. The pressure in the capillary nozzle can exceed 180 atm, while the temperature can exceed 17,000 K. Combined with the Mach number contours in the nozzle, it is easy to see that Case S1 is a pressure driven jet.

Mole fraction contours, taken at t=35 μs, for selected significant species are shown in Fig. 3.5. The contour shape of Fig. 3.5a is representative of molecular compounds produced by the plasma-air interaction. The products of these reactions are contained in a thin region where the plasma comes in contact with the air, preheated by the precursor shock. Figures 3.5b-3.5f show where most of the hydrogen is going chemically. Most of the hydrogen remains atomic, and a significant portion remains ionized in the jet. Very little hydrogen has recombined to H_2, the maximum OH mole

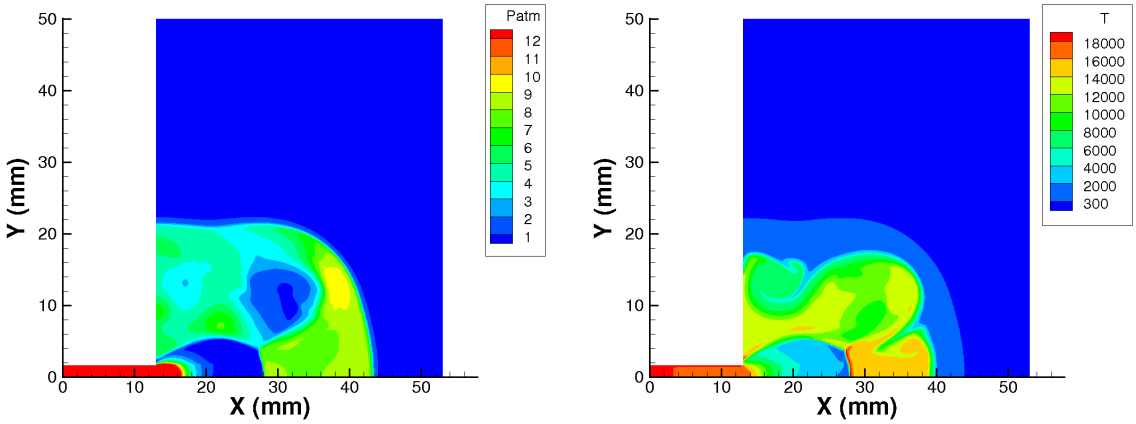

(a) Pressure in atm.

(b) Temperature in Kelvin.

Figure 3.4: Case S1 pressure and temperature contours at t=35 μs.

fraction is 0.022, with the peak H_2O mole fraction below 0.01. Although chemistry is occurring in the plasma-air reaction zone, the jet remains at such a high temperature that it is still composed primarily of hydrogen and carbon atoms and ions. In the reaction zone, oxygen and nitrogen are heated to a point where atomic oxygen has a peak mole fraction of 0.25, similarly atomic nitrogen reaches a peak of 0.3. Complex air ion species, such as NO^+, remain negligible, with mole fractions below 10^{-5}. Air ionization reaches a peak mole fraction of 0.01 and 0.003 for N^+ and O^+, respectively.

The main conclusion that can be drawn from the Case S1 chemistry is that the primary result of the plasma-air reaction in the jet is not the creation of diatomic chemical species, although this does occur to some extent. The main result is ionization and recombination and the dissociation of O_2 and N_2 into atomic form. As will be discussed later, in practical ETC application the capillary-propellant distance will be minimized, thus one can expect this minimal chemistry to occur.

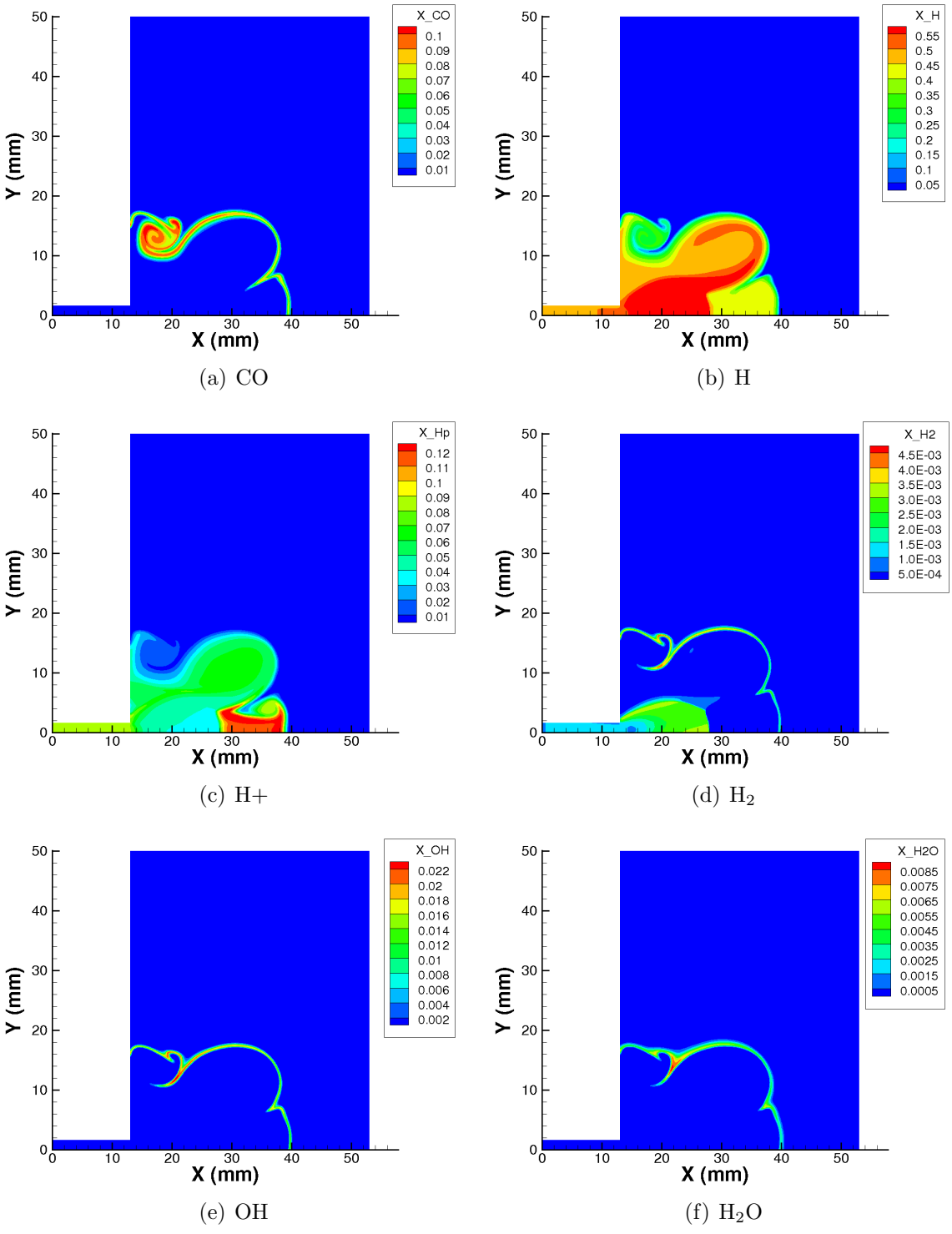

(a) CO (b) H

(c) H+ (d) H_2

(e) OH (f) H_2O

Figure 3.5: Case S1 mole fractions for selected species at t=35 μs.

3.3.2 Case S2

For Case S2 a grid spacing of Δx=0.2 mm is used, which results in a total of 100,570 grid cells. This allows for faster computational times while still capturing the chemistry. Case S2 also ran on thirty 2 GHz processors with a timestep of $\Delta t = 5 \times 10^{-9}$ s, having a total runtime of 174 hours to simulate 110 μs of real time.

To provide a sense of scale, Mach number and temperature contours for the entire Case S2 computational domain at t=115 μs are shown in Fig. 3.6. Mach number contours for the secondary jet at different flow times are shown in Fig. 3.7. Chemistry data is referenced to Case S1 at 115 μs, as the jet is fully developed at this time. The secondary jet emerges from the 1 mm diameter nozzle 75-80 μs after capillary firing. The pressure in the precursor shock behind the nozzle prior to expulsion is approximately 55 atm. As the jet emerges from the second nozzle the temperature drops several thousand Kelvin, as shown in Fig. 3.8b. At 85 μs the pressure in the nozzle is still 50 atm, but this drops to below 7 atm in the rest of the jet. Figure 3.8 also shows that although the pressure in the nozzle is still roughly 50 atm, this drops to no higher than 3 atm within 10 mm of the exit.

The temperature in the bulk of the jet remains below 5,000 K at all times, with the region farthest from the nozzle typically maintaining a temperature below 3,000 K. With such relatively low temperatures it is not surprising that mole fractions of all ionic species are negligible (below 10^{-10}) in the secondary jet. The discrete plasma-air reaction zone, clearly visible in Case S1, can not be seen here. The lack of a discrete plasma-air reaction zone is only partially due to the lower jet temperature. Because the plasma holding chamber was filled with 1 atm air (0.79 N_2, 0.21 O_2 by mole fraction) the plasma-air chemistry was saturated while in the holding chamber. Mach number contours in the holding chamber in Fig. 3.6 show pulsations, due to

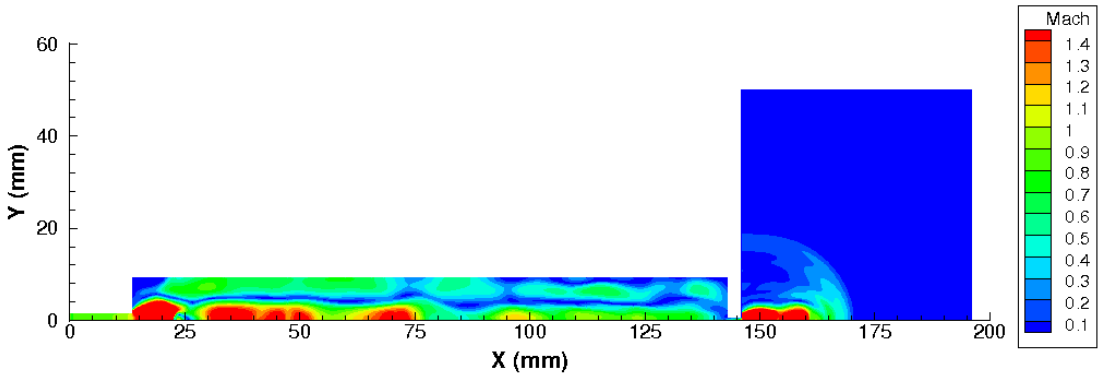

(a) Mach number.

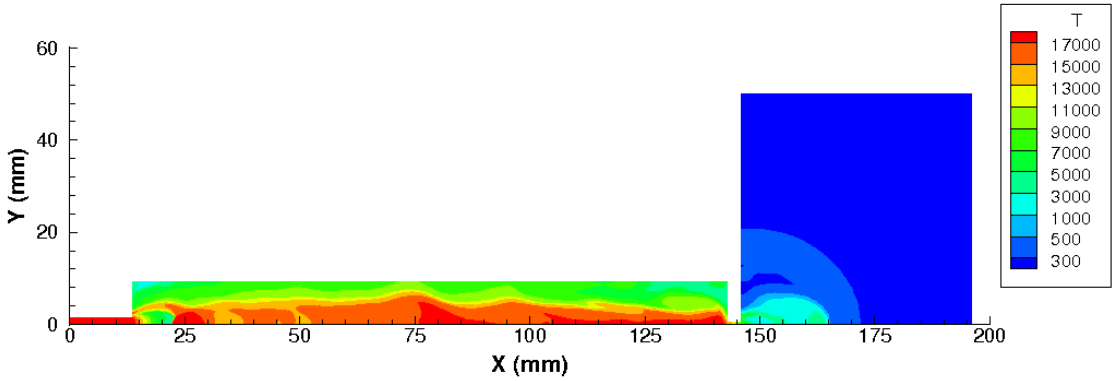

(b) Temperature in Kelvin.

Figure 3.6: Full computational domain for Case S2 showing Mach number and temperature contours at t=115 μs.

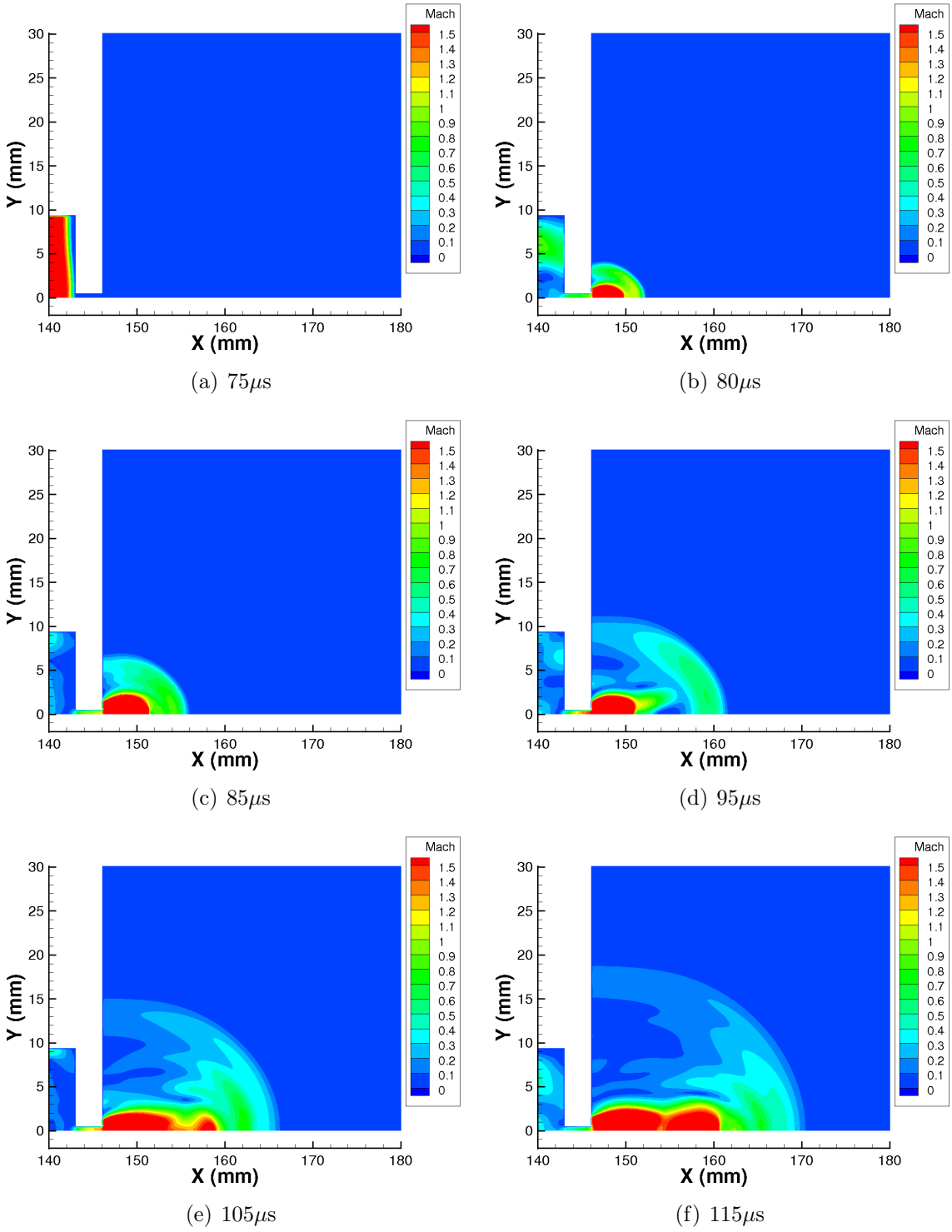

(a) 75μs (b) 80μs

(c) 85μs (d) 95μs

(e) 105μs (f) 115μs

Figure 3.7: Snapshots of Mach number for the Case S2 secondary jet.

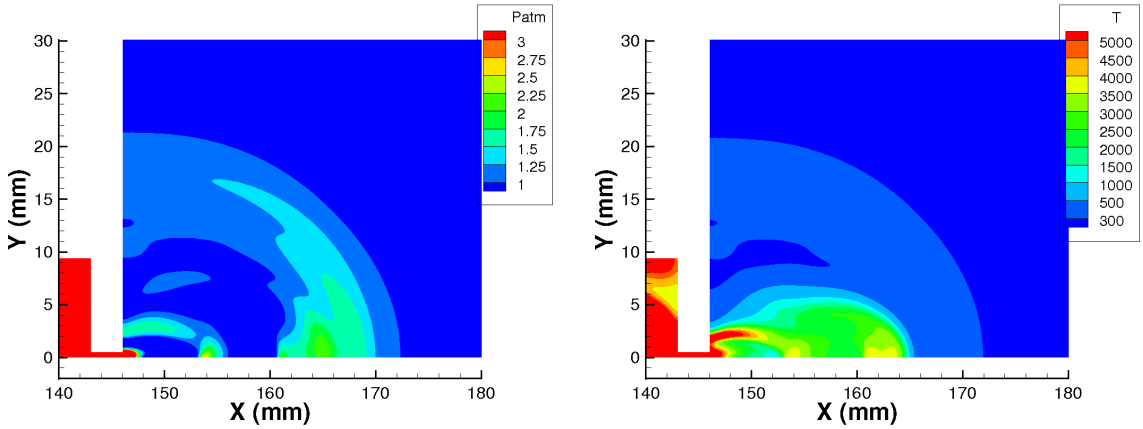

(a) Pressure in atm.

(b) Temperature in Kelvin.

Figure 3.8: Case S2 pressure and temperature contours at t=115 μs.

compression and expansion waves reflecting from the holding chamber walls. This causes the reaction zone to be perturbed, increasing mixing. For these reasons one can not expect to see the same chemistry, and thus the same reaction products, in the primary jet of Case S1 and the secondary jet of Case S2. Future attempts to measure the species present in the plasma jet must take these considerations into account.

As previously mentioned, in the experiment a polyethylene liner was used in the holding chamber, which drastically increased the hydrocarbon-air ratio in the experiment. This leads to the expected result that the experiment detected far more hydrocarbon and hydrocarbon-air species than are found in Case S2. Figure 3.9 shows that atomic hydrogen exits the nozzle but as it begins to cool it becomes depleted. Analysis shows that although there is a halo of H_2 circling the region of depleted atomic hydrogen with a peak mole fraction of 0.002, most of the hydrogen goes toward the creation of OH.

Almost the opposite is true for oxygen. There is so much oxygen available thanks to the holding chamber that the atomic oxygen in the jet goes toward essentially every

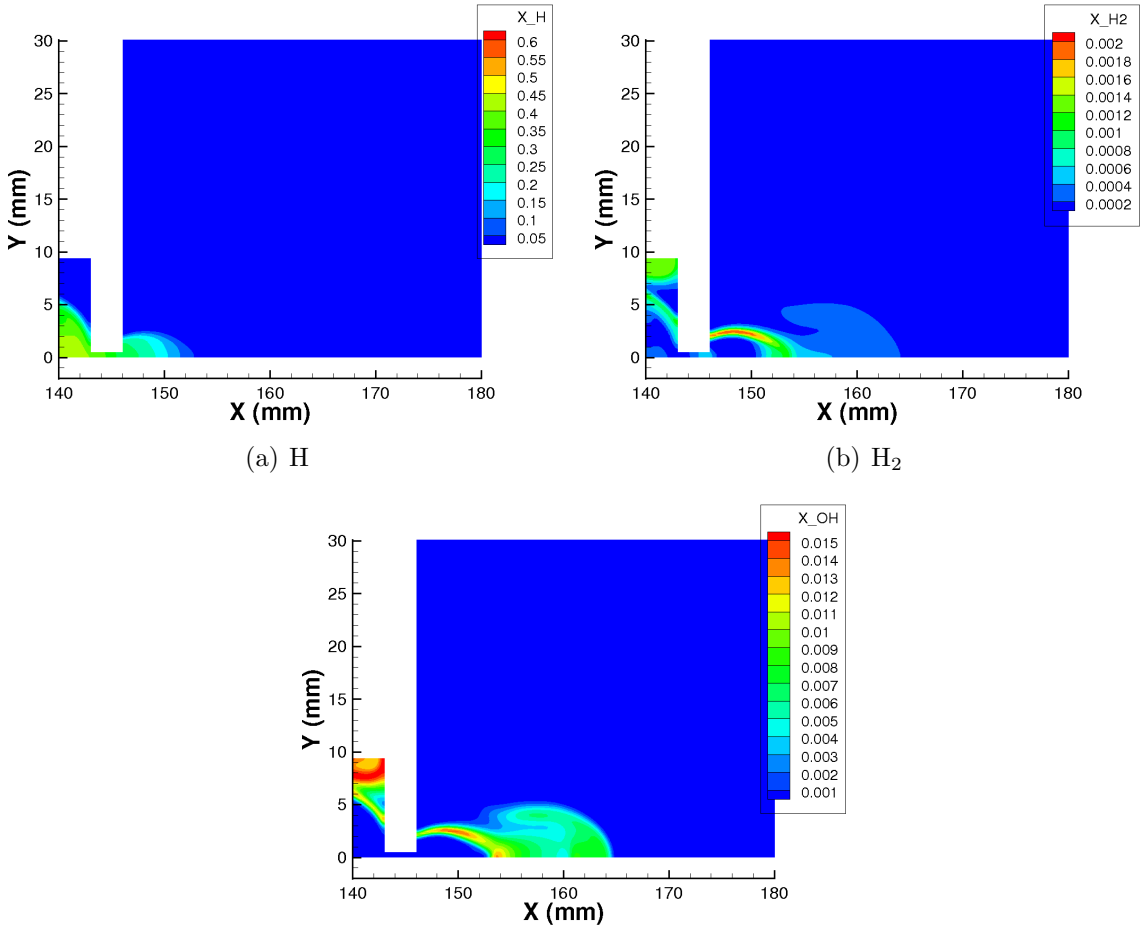

(a) H

(b) H_2

(c) OH

Figure 3.9: Case S2 mole fractions for selected hydrogen species at t=115 μs.

species that contains oxygen, with the limiting factor being the presence of carbon or hydrogen. Figure 3.10 shows that significant atomic oxygen reaction mechanisms are the recombination to O_2, the production of CO, and as this cools the further recombination to CO_2. As the atomic oxygen and nitrogen begin to simultaneously cool, they also recombine to form a relatively high amount of NO in the jet.

It is interesting to note that in the experiment the most abundant species, both with and without the polyethylene liner, was CO. Essentially no CO_2 was detected in the experiment, while a large abundance of C_xH_y species was detected. In both Case S1 and Case S2, the mole fractions remained below 10^{-7} and 10^{-10} for C_2H_2 and C_2H_3, respectively. This disagreement with experiment can not be explained by Case S2, other than to say that it seems unlikely that CO would not recombine to CO_2 while carbon and hydrogen would form such a large amount of C_xH_y species given the abundance of oxygen. Perhaps the measurement method employed was not particularly sensitive to the presence of CO_2, it seems based on the results of Case S2 and the presence of C_xH_y species in the experiment that most of the CO should be depleted.

The main conclusion from the results of Case S2 is that the plasma holding chamber is not a viable option for obtaining measurements of the chemical species present in the plasma jet. The changes in temperature and pressure, as well as the increased interaction time, resulting from the slowing of the flow by the use of a holding chamber means that the species emerging from the secondary nozzle are not directly relatable to the species coming from the capillary.

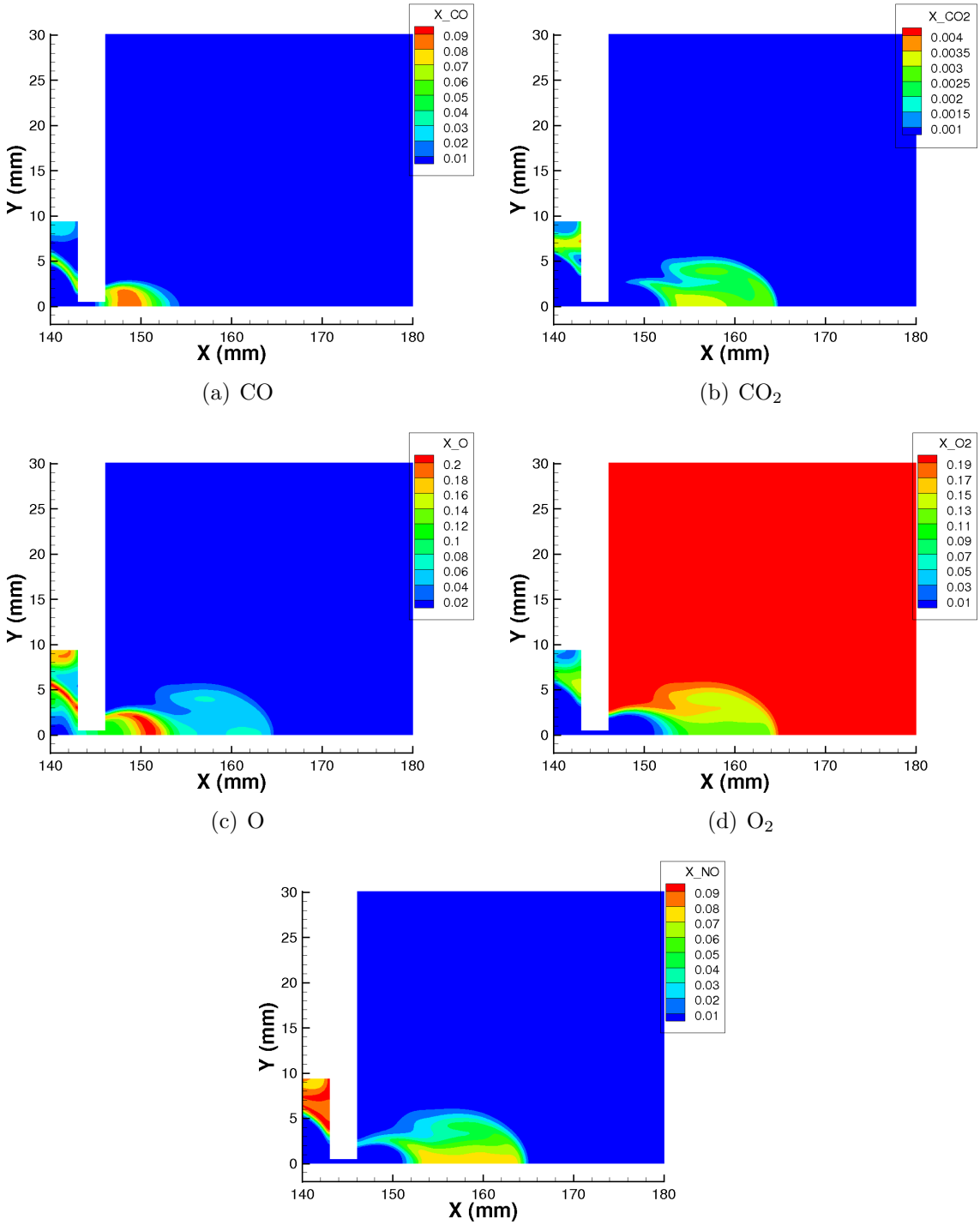

(a) CO

(b) CO_2

(c) O

(d) O_2

(e) NO

Figure 3.10: Case S2 mole fractions for selected oxygen species at t=115 μs.

3.4 Simplification of the Chemical Model

With information from Case S1 and Case S2 it is possible to refine the chemical model. Refinement is possible by simply eliminating species that do not contribute significantly to the plasma-air interaction, thus allowing for a great increase in computational speed. Presented here is what could be considered a minimal model for the chemistry of the plasma-air interaction.

The simulations clearly indicate that all C_xH_y species can be eliminated, as they never present in abundance. Although CH does not present in the jet, it does appear in significant quantities in the capillary nozzle. However, CH_2 does not present significantly even in the nozzle, so could be eliminated. Some of Park's model can be neglected for ETC application. Although their neutral forms are prevalent, O_2^+, N_2^+, and NO^+ do not present significantly. The reason for this being that when temperatures are high enough these molecular species tend to dissociate rather than ionize under these conditions.

For 26 chemical species the implicit CFD method has a 29×29 matrix to solve at every grid point, where 29 comes from 26 species plus two velocities plus energy. The elimination of six species reduces the implicit submatrix to 23×23, a reduction of 312 elements, or a reduction of 60%. Of course, all chemical reactions including these species would also be eliminated, resulting in a further increase in computational speed. The reactions eliminated from Table 3.1 are 4, 8, 15, 20, 23, 26, 27, 29, 30, 41, 42, 50, and 52-58, leaving a total of 41 reactions. These simplifications represent a significant speedup for the code. This simplified model is used throughout the rest of this thesis.

3.5 Plasma-Air Chemistry in Practical ETC Application

All previous work on the expansion of the plasma jet and plasma-air chemistry for ETC application has had a major aspect in common: relatively large capillary-wall, or capillary-propellant, spacings. In the case of capillary-propellant spacing, there is typically a desire to inspect the propellant surface after it has been exposed to the plasma as this is highly informative [2]. It has been found in experiments, however, that for small capillary-propellant distances the propellant is cracked or shattered by the initial pressure wave from the capillary firing [5], leading to typical experimental capillary-propellant distances greater than 20 mm. When a large capillary-wall distance is used it is typically because there are pressure sensors located in the wall, as in Case S1, which are easily damaged by the high temperature, velocity and pressure of the jet near the capillary exit [5], again leading to larger sample distances.

In real ETC application, the geometry of the plasma jet expansion region is much different. There are a number of different propellant packing options, but they primarily reduce to one of two choices, as discussed in Section 1.1. Figure 3.11 illustrates a "tight" propellant packing option [3]. Illustrated on the left of Fig. 3.11 is a coaxial plasma injector, however the principle is the same for a capillary plasma source. On the right is the projectile. The propellant is cut into discs and loose blocks of varying sizes to ensure that little space remains in the artillery shell. Small gaps are left that allow the igniting plasma to expand between the propellant blocks. This packing option yields a large surface area and high density of propellant. Figure 3.12 shows an alternative packing option utilizing a bayonet tube [4]. A cylindrical bore is drilled in a propellant block. A bayonet tube is inserted into this bore. The tube contains holes at regular intervals that allow the igniting plasma to reach the

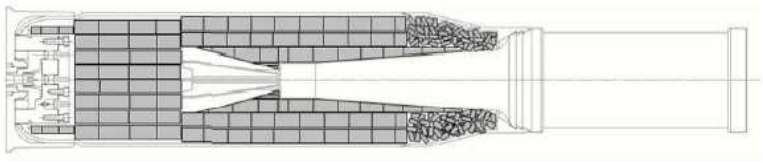

Figure 3.11: Diagram of a tight propellant packing choice, taken from [3].

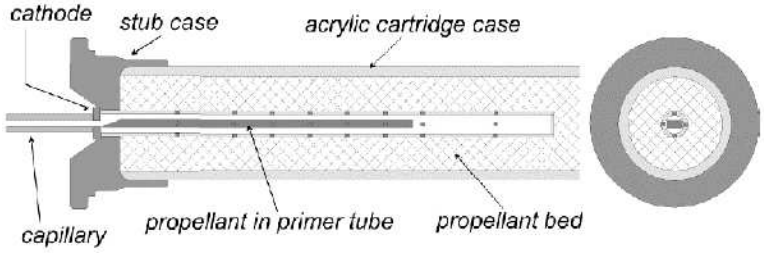

Figure 3.12: Diagram of a bayonet tube packing choice, taken from [4].

propellant bed. The purpose of the tube is to provide regular injection/ignition sites along the length of the propellant bed. Without the tube, and in the case of the tight packing option, ignition starts at the capillary end of the bed and proceeds toward the projectile end. The bayonet tube attempts to induce a more uniform ignition.

With the first method, it is easy to see that plasma-air chemistry will have little effect, as there is little air present in the regions between the tightly packed propellant blocks. The primary chemical mechanism will be the interaction between the capillary plasma and the propellant surface and ablated propellant gases and particulates. A similar conclusion is not so straight forward for the second method. As the plasma advances down the tube the plasma-air reaction zone will be pushed with it, which should severely limit the high temperature air-propellant reaction zone.

Evaluation of Case S1 at t=15 μs indicates that if the capillary-propellant distance is small ($<$ 10 mm), then there will be little to no plasma-air chemistry before the plasma-propellant interaction begins. Furthermore, any ionized, or otherwise affected, air species that are present will be transient, as the reaction zone will

sweep past the propellant surface followed by the capillary plasma jet. The above information for practical ETC application, along with the results for plasma-air reaction rates from Case S1, suggest that in real ETC application the plasma-air interaction is perhaps completely negligible.

To test the importance of the plasma-air interaction in the second propellant packing (bayonet tube) option, a simulation is conducted using the reduced chemistry model. The geometry for this simulation, labeled below as Case S3, is taken from Beyer *et al.* [4]. The capillary inflow is the same as used in Case S1 and Case S2. In the experiment, a tube (6.3 mm diameter, 152 mm length) was inserted into the cylindrical propellant grain. The tube had eight sets of four holes to allow hot ignition gases to escape. Gas flows into the tube from the capillary and exits out the 32 vent holes.

To simulate this geometry the eight sets of holes are converted to eight axisymmetric slits of equal surface area, giving an individual slit width of 0.4 mm. A cell spacing of Δx=0.05 mm is used due to the small size of the outflow slits. A time step of $\Delta t = 5 \times 10^{-9}$ s is used. In the experiment there was no capillary nozzle, thus the simulation geometry is simply an axisymmetric rectangle of dimensions 3.15 mm by 152 mm, with outflow slits every 16.9 mm, and the capillary inflow at x=0 mm. Shown in Fig. 3.13 is a contour plot of temperature taken at t=45 μs that illustrates the Case S3 geometry. Arrows have been added indicating the location of the eight outflow slits, labeled h1-h8, with h1 closest to the capillary inflow.

All flow properties are output at each of the outflow slits over time. Figure 3.14 shows pressure, temperature, and significant species exiting the first outflow slit (x=16.9 mm). Species data is presented in terms of number density. A strong initial spike of N_2 and O_2 is visible as the precursor shock is pushed past the outflow slit.

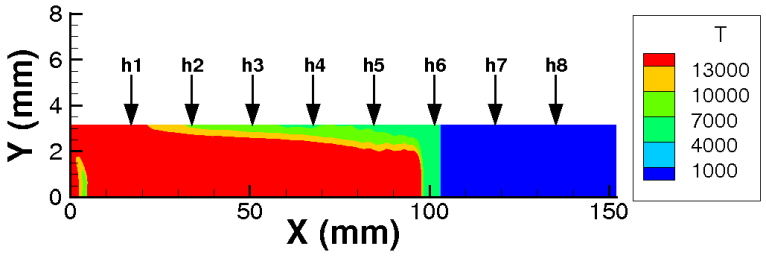

Figure 3.13: Temperature contours (Kelvin) of Case S3 taken at t=45 μs, illustrating the geometry. Note the aspect ratio.

As time progresses we see a steady rise in N, O, and NO as the temperature rises, while N^+ and O^+ remain negligible. When the temperature surpasses 10,000 K the air species have passed the slit and the capillary species have arrived. At this first slit we see a clear distinction between the precursor shock and the plasma jet. For small capillary-sample distances the high temperature gas reaching the propellant surface will be primarily composed of the capillary species, with little plasma-air chemistry taking effect.

Evaluating the outflow data at the remaining seven slits yields much insight. At the slits farthest from the capillary the distinction between the precursor shock's air species and the capillary's plasma species disappears. Outflow data for the final slit (x=135.2 mm) show that the temperature is a few hundred Kelvin lower than the inflow slit due to the chemical reactions happening in the tube. There are also fewer ionic species, but a higher abundance of atomic species. Essentially there is a similar effect at the later slits as was seen in Case S2 with the plasma holding chamber; more plasma-air mixing alters the chemistry of the jet.

This difference in species composition could lead to a different ignition mechanism for the propellant located at the holes further down the tube. At the very least, the plasma temperature is much lower, which will affect the ablation rate. The

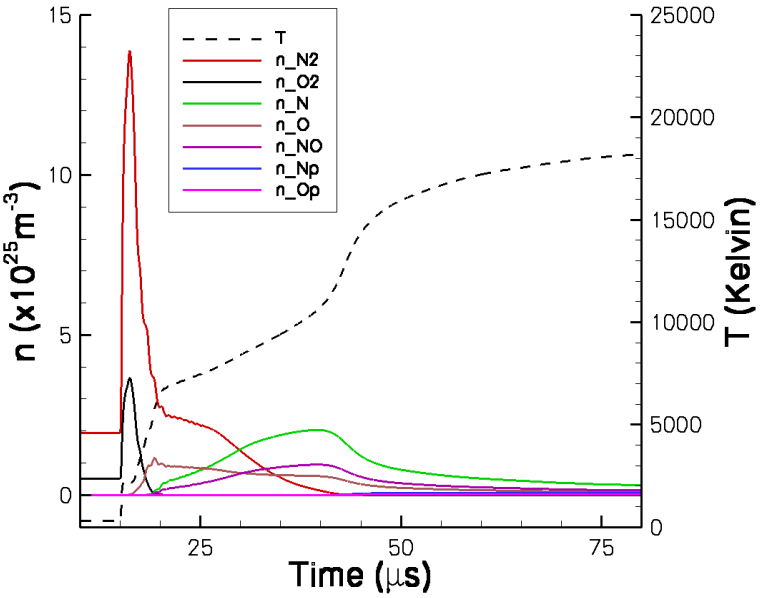

(a) Significant air species and temperature.

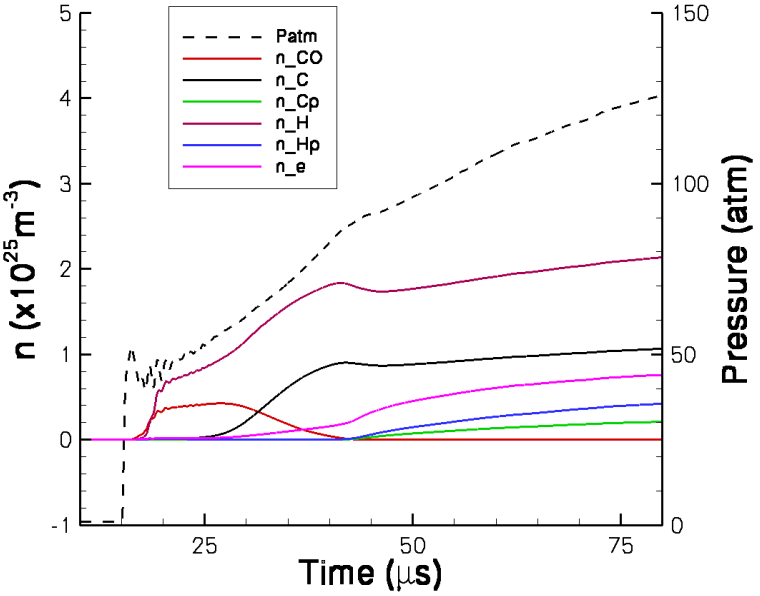

(b) Significant hydrocarbon species and pressure.

Figure 3.14: Outflow data for the first slit (h1) at x=16.9 mm in Case S3.

importance of the chemical composition of the plasma to the PPI ignition process is not well known, and will be discussed in Appendix C.

3.6 Conclusions

Presented was a plasma-air chemistry model designed and tested for ETC application. The results of these simulations allowed further refinements to the chemistry model, allowing for the elimination of some low abundance species and a decrease in computational time.

There are two major conclusions from this chapter. Direct comparisons of Case S1 and Case S2 clearly indicate that there are significant differences between the primary and secondary jets in the referenced experiments. Differences include jet pressure, temperature and chemical composition. It is thus clear that any experiments to measure the species present in the plasma jet must be very carefully designed, and that the use of a plasma holding chamber is not a viable option as it will not produce results representative of species present in the primary jet.

Secondly, an analysis of Case S1 indicates that for capillary-sample distances less than approximately 10 mm the plasma-air chemistry may be entirely negligible. A simulation of a practical ETC ignition mechanism was conducted to evaluate this hypothesis.

With a chemically reacting CFD code and model for plasma-air chemistry in-hand, combined with the computational model for the plasma generating capillary (Chapter II), inflow into a plasma-propellant interaction model can be generated. The PPI model is the primary focus of this thesis, and is discussed in detail in the next chapter.

CHAPTER IV

Plasma-Propellant Interaction Model

As stated in Chapter I, the primary goal of the U.S. Army's recent electrothermal chemical gun research project was to investigate the nature of the plasma-propellant interaction. All work previously discussed in this thesis has been leading up to the concepts, models, and results presented in this chapter. Chapter II introduced the computational model for the capillary plasma generator used in ETC application. The capillary model serves as input to the CFD code introduced in Chapter III that contains the plasma-air chemistry model used to determine the plasma density and temperature at the propellant surface. Chapter V will outline a plasma sheath model that attaches to the PPI model. In Chapter VI, the output from the CFD code will be used directly as input to the PPI model discussed here, however, in this chapter the PPI results are presented parametrically as a function of bulk plasma density and at a single plasma temperature of 1.5 eV, a temperature consistent with results found in Chapter II for typical ETC capillaries.

Previous modeling has not fully taken into account the dynamics of the plasma-propellant interaction, nor the properties of the capillary plasma source [35, 36]. A detailed understanding of the dynamics of the PPI is considered one of the key elements to the future success of practical ETC gun implementation [2]. For instance,

the optimum plasma/propellant pair for most efficient ETC gun design is not currently known. Throughout this thesis, the focus is placed on two solid propellants under consideration for future ETC gun implementation. The two propellants considered are a double-base propellant, JA2, and a nitramine composite propellant, XM39.

Details of the two propellants under consideration, JA2 and XM39, will be presented next. Following that the PPI model will be presented, namely the thermal model employed and how it couples to the ablation model outlined in Appendix A. The chapter will finish with discussion of the results from the PPI model as well as conclusions. Much of the work presented in this chapter first appeared in [37], however, a computational improvement to the thermal model slightly alters some of the numerical results. Those new results are presented here for the first time. While the numerical results differ slightly, none of the conclusions or hypothesis from [37] have changed.

4.1 JA2 and XM39, Propellants of Interest

There are a number of propellants under consideration for ETC application. In the present work the focus is on two in particular, JA2 and XM39. JA2 is a double-base, optically semi-transparent propellant, and is of much interest to the ETC community. It is often a propellant of choice in experiments as JA2 exhibits great response to the PPI phenomenon [1, 4, 5, 10, 38]. XM39, an optically opaque nitramine composite propellant, was selected as the comparison propellant for the PPI numerical modeling because experimental data were available for the ablated mass caused by the PPI [5]. This experimental data is of great importance to the PPI model, as will be explained later. Table 4.1 shows the percent chemical composition

Table 4.1: Composition of the propellant JA2, taken from [9].

Constituent	% by Weight
Nitrocellulose	58.21
Diethylene Glycol Dinitrate	25.18
Nitroglycerin	15.79
Akardit II	0.74
Magnesium Oxide	0.05
Graphite	0.03

Table 4.2: Composition of the propellant XM39, taken from [9].

Constituent	% by Weight
RDX	76.0
Cellulose Acetate Butyrate	12.0
Nitrocellulose	4.0
Acetyl Triethyl Citrate	7.6
Ethyl Centralite	0.4

of JA2, taken from [9]. Similar data for XM39 is presented in Table 4.2.

In order to model ablation of the propellants, a temperature dependent vapor pressure for each is needed, as per Eqn. A.10. Vapor pressure equations for the propellants are not available, thus they were estimated by percent composition. Vapor pressures of constituent compounds were taken from experimental data or modeled via the Clausius-Clapeyron relation using the enthalpy of sublimation and performing a fit to one or more known data points for vapor pressure when experimental data were unavailable. Experimental data were obtained from ARL with the assistance of Dr. Pesce-Rodriguez. The compound vapor pressures are then averaged via the

percent compositions in Tables 4.1 and 4.2 to yield an estimate of the vapor pressure of each propellant. For some constituent compounds, the vapor pressure was either negligible under the temperature range considered, such as for graphite, or there was no vapor pressure data to be found. If no vapor pressure data could be obtained it was assumed that these compounds had negligible vapor pressure, as no other options were available. Compounds with zero, or assumed zero, vapor pressure are: nitrocellulose, magnesium oxide, graphite, and cellulose acetate butyrate.

The resulting propellant vapor pressures are plotted in Fig. 4.1 over a surface temperature range found to be suitable based on the PPI numerical studies. The vapor pressure equations representing the curves in Fig. 4.1 are presented as Eqns. 4.1 and 4.2 for JA2 and XM39, respectively, with T_s in Kelvin and P in Pascals. Enthalpies of sublimation, ΔH, for the propellants were similarly calculated via percent composition. The resulting enthalpies are 4.41×10^5 J/kg for JA2 and 5.47×10^5 J/kg for XM39.

$$\begin{aligned} P_{JA2}(T_s) &= 0.2518\exp\left(36.5447 - 11222/T_s\right) \\ &\quad +0.1579\exp\left(32.9496 - 10715.4/T_s\right) \\ &\quad +0.0074\exp\left(17.2491 - 8005.77/T_s\right) \end{aligned} \tag{4.1}$$

$$\begin{aligned} P_{XM39}(T_s) &= 0.76\exp\left(37.5986 - 15648.3/T_s\right) \\ &\quad +0.076\exp\left(19.3853 - 6849.89/T_s\right) \\ &\quad +0.004\exp\left(18.1824 - 7541.5/T_s\right) \end{aligned} \tag{4.2}$$

In order to thermally model the propellants, the additional parameters of specific heat at constant pressure (C_p), thermal conductivity (λ), and thermal diffusivity (α)

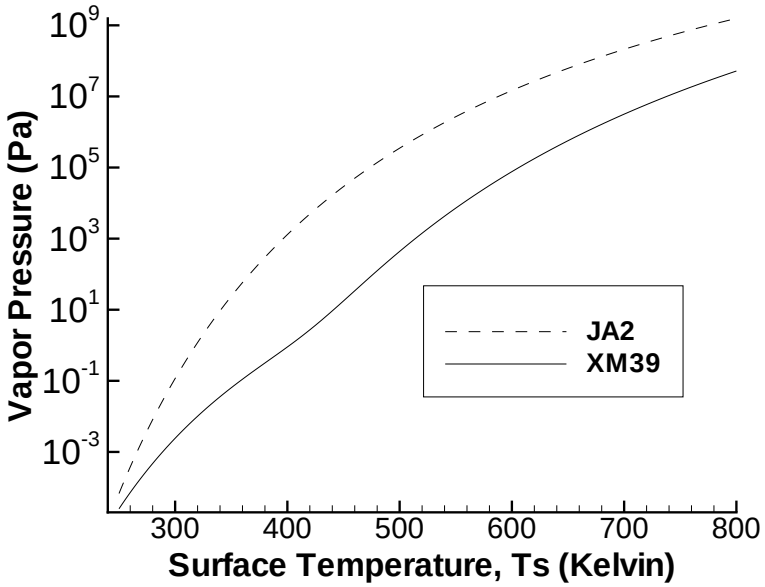

Figure 4.1: Calculated vapor pressure for each propellant.

Table 4.3: Thermophysical properties of the propellants, taken from [9].

	C_p (J/kgK)	λ (W/Km)	α (m^2/s)
JA2	$1520.45, 75°$ C	$0.280, 49°$ C	$1.30 \times 10^7, 49°$ C
XM39	$1296.35, 75°$ C	$0.246, 48°$ C	$1.21 \times 10^7, 48°$ C

are required. Constant values for these three parameters were obtained from [9] and are listed in Table 4.3. Although these three parameters are, in general, temperature dependent, experimental data did not include the range of temperatures experienced during the PPI. For that reason, values were taken at the highest temperature available. The temperatures the data are taken from is quoted along with the value in Table 4.3.

4.2 Plasma-Propellant Interaction Model

The kinetic ablation model of Keidar *et al.* [18], outlined fully in Appendix A, is used for all PPI modeling in this thesis. As discussed in Appendix A, while the

ablation model remains unchanged for a wide range of applications, the thermal model differs. Presented in this section is a brief overview of the ablation model, and a thorough overview of the thermal model that is coupled to the ablation model, as well as the conditions, dictated by experimental data, that the model is based on. This coupled ablation-thermal model is referred to throughout this thesis as the plasma-propellant interaction model.

4.2.1 Experimental Ablated Masses

As discussed in Section 1.2, experimental work of Li *et al.* directed a capillary plasma jet at samples of JA2 and XM39 [5]. Since these experiments were conducted in an open chamber, the pressure was not allowed to build to the point were propellant ignition occurred. This allowed for measurements of the mass lost due purely to the plasma-propellant interaction, with no propellant burning observed. The results of this experiment, and it's geometry, have been adopted here for modeling the plasma-propellant interaction.

In the experiment, the propellant sample was held in a large holder 25 mm from the capillary nozzle. The capillary was charged to a voltage of 4 kV, with a discharge time of Δt=280 μs. Note that Chapter III indicates that this capillary sample distance will yield a plasma-air interaction before the PPI begins, a fact that will be taken into account in Chapter VI, but is neglected in the simulations contained in this chapter. The sample was a disc 4 mm thick and 10.9 mm in diameter, with the flat surface directly facing the incoming capillary plasma jet [5]. These dimensions yield a surface area of 9.33×10^{-5} m^2, which is used to convert ablation rate into ablated mass throughout this work. The experiment yielded a total ablated mass of 5.3 mg and 2.8 mg for JA2 and XM39, respectively.

4.2.2 Brief Overview of the Ablation Model

Presented here, for completeness, is a brief overview of the ablation model developed by Keidar *et al.* that is used extensively in this work. A thorough explanation of the model is presented in Appendix A, and the reader is directed there if further details are required.

Keidar's model is based on the concept of coupling the kinetic laser ablation theory of Anisimov [39] with a hydrodynamic non-equilibrium layer to relate the wall properties to the bulk plasma properties. In the model, the Knudsen layer equations of Anisimov are coupled to a collision dominated non-equilibrium hydrodynamic layer, which in turn is attached to the bulk plasma. It is assumed in Anisimov's model, and also in Keidar's model, that the velocity distribution function in the Knudsen layer can be represented as a Maxwellian. Conservation integrals can then be applied to the Knudsen layer to yield a system of three coupled algebraic equations. The solution of the mass and momentum conservation equations in the hydrodynamic layer allows for the determination of the heavy particle (ion) velocity at the interface of the hydrodynamic and Knudsen layers. The system is closed with the propellant vapor pressure, which allows for the determination of the ablated gas number density at the propellant surface. The remaining parameters are the bulk plasma density and temperature, and the propellant surface temperature. The bulk plasma properties can be explored parametrically, as they are in this chapter, or solved for exactly via the CFD code of Chapter III, as they will be in Chapter VI. The propellant surface temperature is solved for via a thermal model. The coupled ablation-thermal model is outlined next.

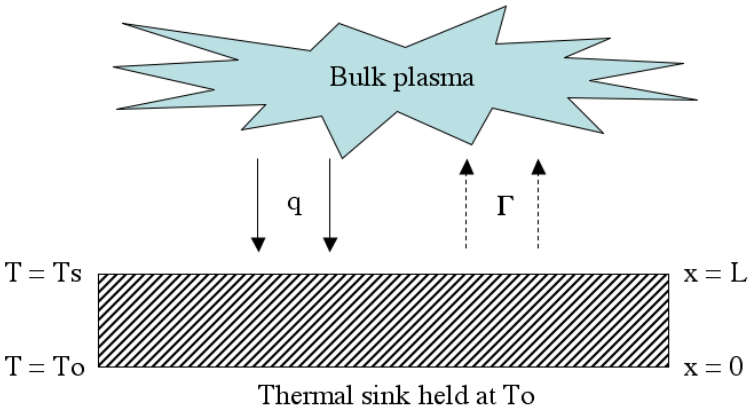

Figure 4.2: PPI model coordinate system.

4.2.3 Coupled Ablation-Thermal Model

The thermal model is based on the one dimensional heat flux equation with an ablation boundary condition. The geometry used in the ablation-thermal model is shown in Fig. 4.2. A total surface heat flux, q, flows from the bulk plasma to the surface of the propellant sample. This heat source causes a rise in the surface temperature, T_s, which triggers ablation, represented as the ablation rate Γ, which in turn carries heat away from the surface. The propellant sample has depth L=4 mm [5], with $x = L$ being the surface exposed to the plasma. The initial propellant temperature is taken to be T_o=298 K. The heat flux equation is given as

$$\frac{\partial T(x,t)}{\partial t} = \alpha \frac{\partial^2 T(x,t)}{\partial x^2}, \tag{4.3}$$

where α differs for each propellant and is given in Table 4.3. The thermal boundary conditions are

$$\frac{\partial T(L,t)}{\partial x} = -\lambda^{-1}(q - \Delta H\Gamma - C_p(T_s - T_o)\Gamma), \tag{4.4}$$

$$T(0,t) = T_o,\ T(x,0) = T_o, \tag{4.5}$$

where $T_s = T(L,t)$.

Note that Eqns. 4.4 and 4.5 are similar, but not identical, to those used in the thermal model of the capillary plasma source, Eqns. 2.6 and 2.7. The ablation rate in Eqn. 4.4 comes from the ablation model, and is a function of the surface temperature, plasma density and plasma temperature, thus $\Gamma = \Gamma(T_s, n_o, T_e)$, where n_o and T_e are the bulk plasma density and temperature. Keidar's ablation model allows for ablation tables to be generated that are functions of these three parameters. Based on the results of the capillary parameter study (Chapter II), a constant plasma temperature of T_e=1.5 eV was used for all simulations in this chapter, although a time varying plasma temperature, as determined by the CFD code, will be used in Chapter VI. Using reference tables for the ablation rate makes coupling the thermal and ablation models trivial from a programming standpoint.

The thermal model has been solved two different ways. In a previously published report, a semi-analytical method was used to rapidly solve for the temperature profile in the propellant sample [37]. In this chapter, and throughout the rest of this work, a numerical method is used to spatially discretize the propellant sample and solve for the temperature distribution. Although more computationally intensive, it was felt that this method would yield more accurate results. Indeed, the PPI model outlined in [37] was always viewed by the authors as a first order model, with room for computational improvement. The results presented here can be considered to be more accurate than those presented in [37], although none of the conclusions are changed between the reference and the present work. Numerically solving for the temperature distribution can be made less computationally intensive by using results from the semi-analytical model. Results of that method clearly show that over the course of the PPI the temperature change in the propellant only occurs within the top 1% of the propellant sample. In order to accurately capture the temperature

gradient, many grid points are needed near the propellant surface. However, since the temperature only changes within 1% of the propellant, most of the sample does not need to be simulated. Studies conducted with the numerical model showed that, for a representative range of heat flux, the top 2% of the propellant could be simulated and roughly half of the domain would still be at the initialization temperature, T_o, at the end of the PPI. This allowed for a 50-fold decrease in computation time.

Shown in Figs. 4.3 and 4.4 are ablation rate contours, generated purely by the ablation model, for each propellant. If the ablation rate was constant during the plasma pulse, the total ablated masses for JA2 and XM39 would be reproduced by ablation rates of 203 and 107 kg/m^{2}s, respectively. These plots clearly indicate that the same ablated mass can be achieved with various combinations of bulk plasma density and propellant surface temperature. For instance, following any of the curves shown in Fig. 4.3 will yield the exact same total ablated mass for a constant ablation rate configuration. If the surface temperature is time varying, as it is in the PPI model, then there are even more combinations of plasma density and surface temperature that will yield the same total ablated mass. As the surface temperature is determined by the model, it is clearly necessary to know the bulk plasma density to have a unique solution. However, the total surface heat flux still remains a parameter. In the PPI model, the ablated mass is known from experimentation and is used to find the total surface heat flux, as this heat flux can not easily be found experimentally and is of interest.

4.2.4 Post-PPI Surface Temperature

The thermal model, Eqns. 4.3–4.5, is used to find the surface temperature during the plasma pulse, when $0 \leq t \leq \Delta t$. During this time it is found that the surface

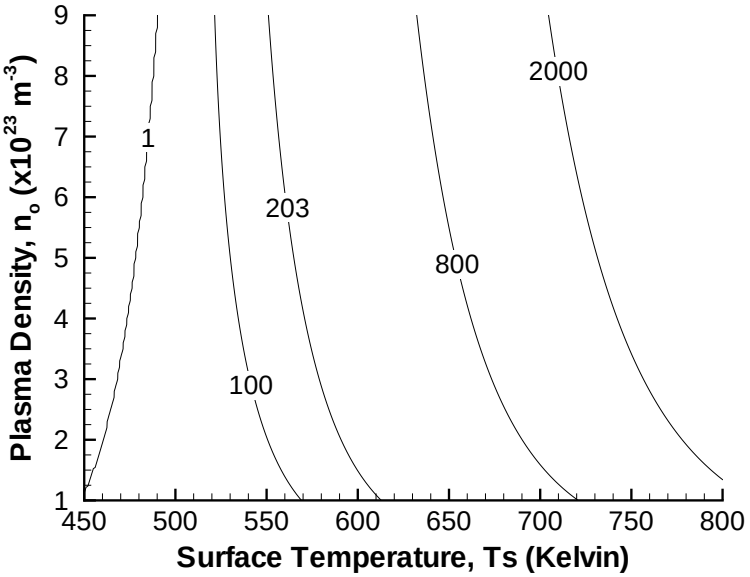

Figure 4.3: Sample ablation rate (kg/m^{2}s) contours for JA2.

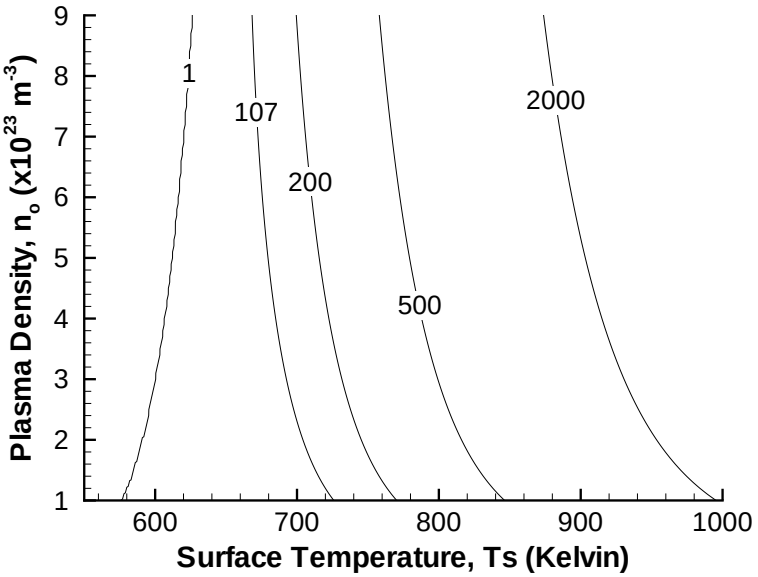

Figure 4.4: Sample ablation rate (kg/m^{2}s) contours for XM39.

temperature rises very slowly and does not reach a steady state value. It is assumed here that the PPI only lasts for the duration of the plasma pulse, which ends at $t{=}\Delta t$. Once the pulse is over, it is assumed that the plasma completely dissipates. The surface temperature after the plasma pulse is modeled by Eqn. 4.6, a relation which is commonly used in discharge modeling [20]. During cooling, there will be no ablation after the vapor pressure of the propellant reaches atmospheric pressure, giving an upper bound on t.

$$T_s = T(L, \Delta t)\sqrt{\frac{\Delta t}{t}},\ t \geq \Delta t \tag{4.6}$$

There are a number of reasons to expect the propellant to cool rapidly after the pulse. As previously mentioned, the thermal model indicates that at the end of the pulse the temperature gradient is contained within 1% of the surface, an effect that will lead to very rapid surface cooling. In addition, with 99% of the sample still at room temperature, there is much room within the propellant for the heat to dissipate. In the experiment [5], the propellant sample was held in place by an object of significantly larger thermal mass, which would act as a sink for cooling. Also, since the experiment was conducted in an open chamber, room temperature air would be pushed out of the experimental chamber by the plasma wave, with cool air rushing back into the chamber after the pulse, dropping the ambient temperature [5]. All these factors will contribute to rapid cooling in cases based on experimental configurations designed to observe the PPI.

The coupled ablation-thermal model can now be solved, generating as output the total propellant ablated mass (obtained from the ablation rate and the propellant surface area) as functions of bulk plasma density and total heat flux. Experimental data for the ablated mass caused by the PPI for JA2 and XM39 [5] allows for the

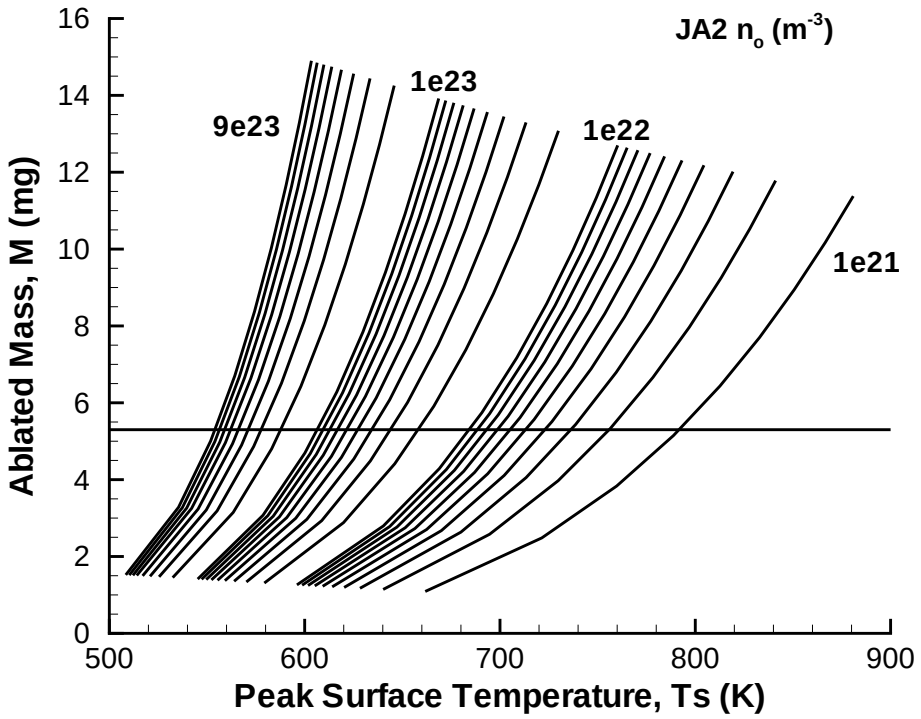

Figure 4.5: PPI model results for ablated mass versus peak JA2 surface temperature.

determination of the total heat flux incident on the propellant surface.

4.3 Results

The PPI model allows for the parametric study of the plasma-propellant interaction. By varying the bulk plasma density and surface heat flux, the total ablated mass can be found by time integrating the ablation rate over the experimentally known surface area of the propellant. Plotting the results as a function of peak surface temperature, that is $T_s = T(L, \Delta t)$, Figs. 4.5 and 4.6 can be generated. As previously mentioned, the experiments of Li *et al.* measured a total ablated mass of 5.3 mg and 2.8 mg for JA2 and XM39, respectively. These values are shown as horizontal lines in Figs. 4.5 and 4.6. The simulated range of bulk plasma number density was estimated from previous capillary simulations and the experimental geometry to likely be in the range 10^{21}–10^{24} m^{-3}.

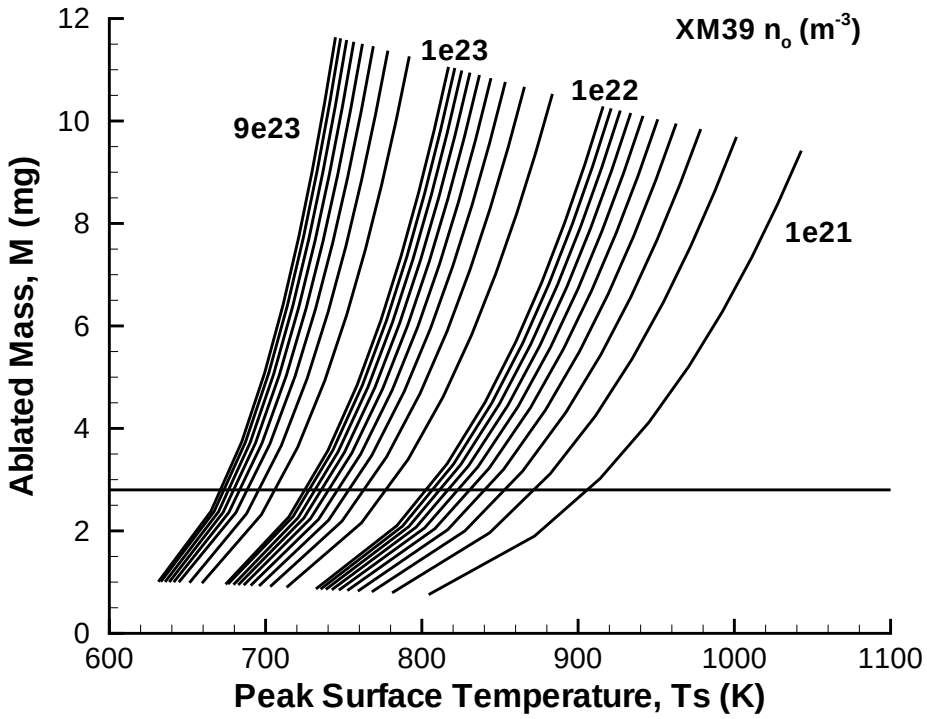

Figure 4.6: PPI model results for ablated mass versus peak XM39 surface temperature.

Linear interpolation is used to determine the exact heat flux that results in the experimental ablated mass for a given bulk plasma density. This can be visualized as the intersection point of the horizontal lines, representing the experimentally determined ablated mass, with the simulation curve at any chosen density in Fig. 4.5 or 4.6. This interpolated data is displayed in Fig. 4.7, where there is now only one curve for each propellant that perfectly matches the experimental total ablated mass at each plasma density. The total heat flux for both propellants is on the order of 1×10^8 W/m^2. Again, as the plasma density in the experiment is not known it is treated parametrically here. Bulk plasma density and temperature will be solved for directly in Chapter VI using the models outlined in Chapter III.

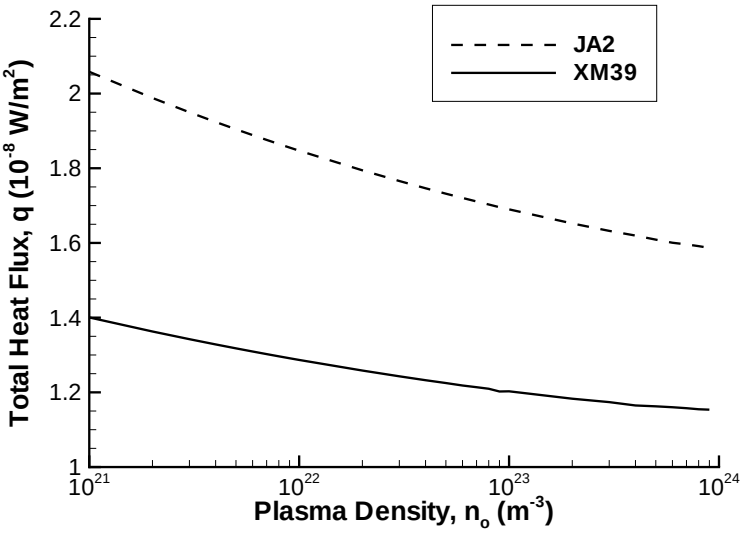

Figure 4.7: Total surface heat flux to each propellant needed to reproduce the experimental ablated mass.

4.4 Discussion

Since it is assumed that the capillary plasma source generates an identical plasma for each propellant, any differences in the incident heat fluxes must be due to differences in the propellants themselves. It can clearly be seen from Fig. 4.7 that JA2 will consistently have a higher heat flux than XM39. Careful inspection of Figs. 4.5 and 4.6 shows that XM39 will have a higher surface temperature at a given plasma density, but this clearly does not translate into a higher ablated mass.

The downward slope of the curves in Fig. 4.7 is readily explained by the ablation rate contours. As plasma density increases in Fig. 4.7, total heat flux (or peak surface temperature) decreases. This is analogous to what is seen in Figs. 4.3 and 4.4. Following the 200 kg/m^{2}s curve in Fig. 4.4 shows that as plasma density increases the surface temperature must decrease. Thus it is clear that the shape in Fig. 4.7 is due to the fact that the total ablated mass is fixed at each plasma density, forcing the heat flux to decrease as plasma density increases in order to preserve the total

ablated mass.

Figure 4.7 raises the question that if the bulk plasma is identical for each propellant, why is the total heat flux different? Indeed, one would initially expect that the heat flux would be the same for each propellant, with the difference in ablated masses due to the differences in thermal conductivities and vapor pressures of the propellants. A comparison of the optical properties of the two propellants yields insight into the differences between the total heat fluxes of JA2 and XM39. Nitramine composite propellants, such as XM39, are opaque to most wavelengths, and studies indicate that they do not allow radiation to penetrate and affect change in-depth. As previously discussed, it has been demonstrated that JA2 allows radiation to penetrate in-depth, with physical and chemical changes occurring up to approximately 1 mm into the propellant [10, 2]. In addition, it has been determined in experiments that XM39's reflectivity may be as high as 50% [11]. This information suggests that the difference between the heat flux to JA2 and XM39 is due to the optical properties of each propellant, specifically to the suceptibility to penetrating radiation from the plasma. Since JA2 is semi-transparent, radiation absorption would allow for an additional heating mechanism during the PPI. While XM39's opacity and high reflectivity would block most, if not all, of the radiative energy from heating the propellant bed. Much research has been done studying the radiation from the plasma and what effect it could have on the PPI [10, 2], so this suggestion is not surprising.

If the difference in total heat flux between the two propellants is indeed due to plasma radiation, it is possible to calculate a preliminary estimate of the magnitude of the radiative heat flux. Assuming that XM39 receives no radiative energy from the plasma—which is not a very good assumption, but will suffice for this simple estimate—it is possible to define $\Delta q = q_{\mathrm{JA2}} - q_{\mathrm{XM39}}$ as the amount of heat flux JA2

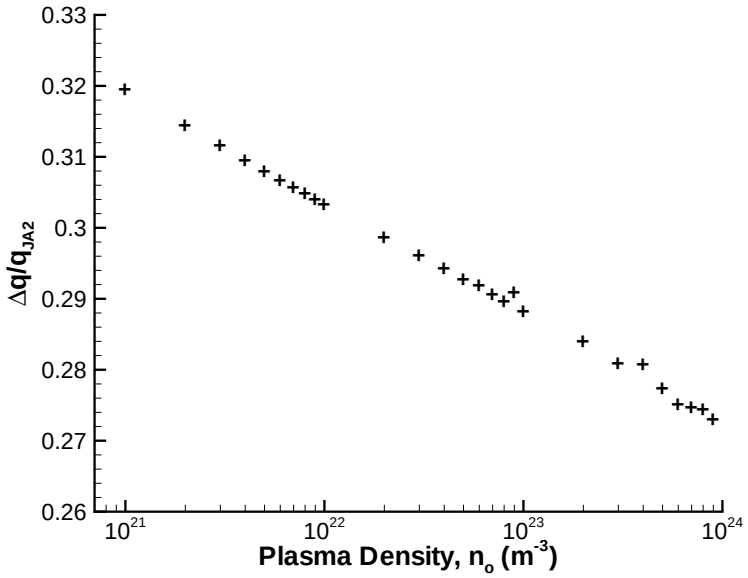

Figure 4.8: The approximate JA2 radiation fraction, $\Delta q/q_{JA2}$, as a function of plasma density.

receives by absorption of penetrating plasma radiation. It should be noted that Δq represents only a small fraction of the radiative heat flux available in a black body plasma at T_e=1.5 eV. This difference can be partially explained by indications that vaporized propellant can act as a plasma radiation shield, helping to block some of the radiation flux coming from the plasma from ever reaching the propellant bed [5]. Thus, the quantity $\Delta q/q_{\mathrm{JA2}}$ should roughly approximate the contribution to JA2's total heat flux made by plasma radiation. Under these assumptions, Fig. 4.8 indicates that radiation constitutes 27–32% of JA2's total heat flux. Although only a rough estimate, when this work was originally presented [37] it represented the first time such an estimate could be made. This estimate is refined further in the next chapter with the inclusion of a plasma sheath model for the determination of the convective heat flux to the propellant bed. Assuming a two element heating mechanism (convective and radiative), it is possible to determine what fraction of the total heat flux is made up of radiative heat flux, for each propellant.

Experimental work by Das *et al.* indicates that the radiative heat flux estimate (Δq) lies at least within an order of magnitude of reality [12]. In the experiment, temperature sensors were placed behind an optically transparent stagnation plate, which only allowed radiative heat flux to affect the sensors. When a capillary discharge plasma was directed at the plate, the surface temperature as a function of time was determined. A thermal model, similar to the one employed here but obviously neglecting ablation, was used to determine the radiative heat flux incident on the surface. For a capillary-sample distance of 50 mm and capillary charging voltage of 2.5 kV, a peak heat flux of 1.4×10^7 W/m^2 was found. Increasing the sample distance to 75 mm decreased the peak heat flux to 3.8×10^6 W/m^2 [12]. In the present work, the radiative heat flux is on the order of $\Delta q = 5 \times 10^7$ W/m^2. It is well within reason that a decrease in capillary-sample distance to 25 mm and an increase in charging voltage to 4 kV (to match the conditions in [5]) could readily yield a radiative heat flux on the order of Δq.

4.5 Conclusions

The PPI model presented in this chapter is the first such model to solve for the total heat flux to the propellant bed. This is significant as the total heat flux can not readily be measured in experiments. This is accomplished by using experimental data for the total ablated mass after the PPI to parametrically close the model. It should be noted that experiments to determine this total ablated mass are relatively simple when compared to attempts to measure the heat flux to the propellant bed.

The results of the PPI model indicate that radiative heat flux from the plasma constitutes a non-trivial heat source for the plasma-propellant interaction. This means that the optical properties of the propellants can not be ignored, and that the

best propellant choice for ETC application is one that allows plasma radiation to penetrate in-depth, tapping a significant heating mechanism. The results presented here seem to agree well with experimental data, although comparison in this regard is limited due to the aforementioned difficulty in conducting heat flux measurements.

This chapter clearly indicates the need to determine what mechanisms are contributing to the total heat flux that reaches the propellant bed. What percentage of the heat flux is due to convective flux from the plasma? What percentage is due to radiation? Is plasma-surface chemistry significant? The first two questions will be addressed in the next chapter with the development of a plasma sheath model, while the last question will be addressed briefly in Appendix C.

CHAPTER V

Collisional Plasma Sheath Model

While the plasma-propellant interaction model, outlined in the previous chapter, provided the average total heat flux to the propellant bed, it did not yield any quantitative information concerning where this total comes from. What fraction of the total heat flux is made up of radiation? What fraction comes from convective particle flux? For the reasons outlined in Section 1.2.3, radiation modeling in the case of the plasma-propellant interaction is not attempted in the present work. However, modeling the convective particle flux can be performed by means of a collisional plasma sheath model attached to the ablating propellant surface.

This chapter outlines the collisional plasma sheath model developed for ETC application. Results are discussed for constant neutral density, before results with a time varying neutral density, obtained from the PPI model, are presented. By using the total heat flux obtained from Chapter IV, and the convective heat flux obtained in this chapter, the fraction of the total heat flux due to the convective heat flux is determined as a function of bulk plasma density. The results in Section 5.3.1 were first published in [40], while the results of Section 5.3.2 use the updated PPI model, and are presented here for the first time.

5.1 Introduction to Plasma Sheaths

A plasma sheath forms at any solid boundary in contact with a plasma. In the quasi-neutral bulk plasma, the ion and electron densities are equal everywhere, $n_i = n_e = n_o$, and the ions and electrons are thermalized, meaning they have the same temperature. If the heavy ions and light electrons have the same temperature, then that means the electrons are moving much faster than the heavy ions, otherwise their kinetic energies would not be the same. As the bulk plasma approaches the wall, the fast moving electrons strike the wall before the slow moving ions. The electrons striking the wall establish a negative potential on the wall with respect to the plasma. This negative potential, ϕ_w, repels some electrons from the vicinity of the wall, while attracting ions. The wall potential will continue to drop until the ion and electron fluxes balance, creating a condition known as a floating potential (see Eqn. 5.7 below). In the plasma sheath, $n_i > n_e$, thus quasi-neutrality no longer holds.

In most sheath models, the electron density is computed directly from the sheath potential under the assumption of Boltzmann electrons. As the sheath potential is a function of space, $\phi = \phi(x)$, the electron density in the plasma sheath, under the assumption of Boltzmann electrons, is given by

$$n_e = n_e(x) = n_o \exp(\phi(x)/T_e), \tag{5.1}$$

where T_e and ϕ have units of Volts [19]. Inherent in the assumption of Boltzmann electrons is that the electrons are bound strongly to the electric potential. Although this was first derived for collisionless sheaths, it is found that, due to the small collision cross section of electrons, this assumption holds even in highly collisional plasma sheaths [41].

In the type of plasmas encountered in ETC application, the plasma density is high enough that ion-ion and ion-electron collisions in the bulk plasma are frequent enough that the plasma can be treated hydrodynamically, as it was in Chapter III. The collisionality of a plasma sheath, however, concerns the ion-neutral collision frequency. For ETC application, the neutrals come from the ablating propellant surface, and are made up of the propellant gas itself. Collisions with neutrals will decrease the ion velocity in the sheath, via drag. Thus, the ion-wall impact velocity of a collisional sheath will be less than the ion-wall impact velocity of a collisionless sheath, an effect which will have great importance here. The dynamics of a collisional plasma sheath is a topic of interest in a wide range of applications from analysis of probe measurements [42] to fusion devices [43].

5.1.1 The Need for a Sheath Model in ETC Application

Due to the negative wall potential, the ion-wall impact velocity will be higher than it would be without the plasma sheath. Higher ion velocity means higher ion kinetic energy, thus the plasma sheath will increase the kinetic energy of ions striking the wall, increasing the convective heat flux. However, as discussed above, the collisionality of the sheath will also affect the ion-wall impact velocity. Thus a computational sheath model must be used to determine the exact ion-wall impact velocity, as direct analytical sheath results can not be used over the entire range of conditions encountered in ETC application, as will be seen in Section 5.3.1.

5.2 The ETC Sheath Model

The one-dimensional, mono-energetic sheath model implemented here assumes Boltzmann electrons and uniform background neutral density. The geometry of the sheath model is shown in Fig. 5.1. The sheath model is coupled to the PPI

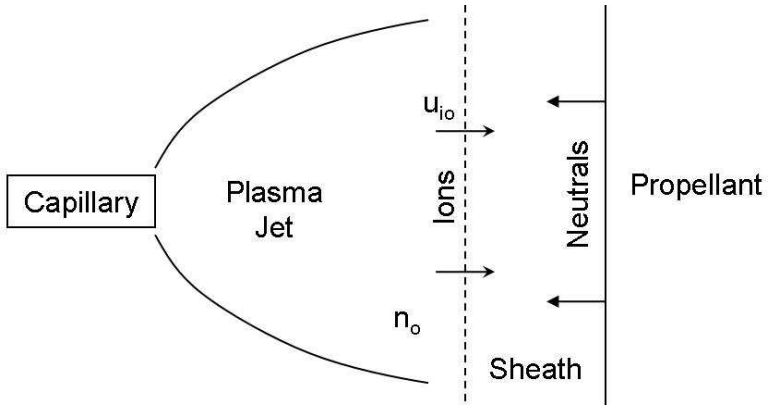

Figure 5.1: Diagram of sheath model geometry. Present model represents the region of the sheath coupled to the PPI model for propellant ablation.

model presented in Chapter IV. The ablated propellant gas forms a uniform neutral background density which makes the sheath collisional. Ions enter the sheath at non-dimensional speed u_{io}.

The capillary discharge model of Chapter II indicates a plasma temperature of T_e=1.5 eV is appropriate. Chapter VI will use a time varying plasma temperature, as determined by the CFD work of Chapter III. The equations to be solved are ion continuity (Eqn. 5.4) and momentum (Eqn. 5.5), and the Poisson equation for the electrostatic potential (Eqn. 5.3) . By making the cold ion assumption the ion density gradient in the momentum equation can be neglected, and the resulting equations can be solved by numerical integration via the Runge-Kutta method [44], starting at the bulk plasma and proceeding toward the wall. This numerical method requires an additional equation for completeness, which is given by the relation between electric field and potential, listed as Eqn. 5.2 below.

For generality of solution, the equations are non-dimensionalized. All densities are non-dimensionalized by the bulk plasma density, n_o, thus the ion density is given by $N_i = n_i/n_o$, and the neutral density by $N_n = n_n/n_o$. The electric potential is given as $\eta = \phi/T_e$, with T_e in Volts. Velocities are non-dimensionalized by the

Bohm velocity, C_s, thus $u_i = v_i/C_s$, where $C_s = \sqrt{eT_e/m_i}$ and m_i is the average atomic mass of the propellant in question. Spatial dimension uses Debye length for normalization, thus $y = x/\lambda$, where $\lambda = \sqrt{\epsilon_o T_e/(en_o)}$, and ϵ_o is the permittivity of free space. Lastly, electric field is non-dimensionalized to $\varepsilon = E\ \lambda/T_e$. The sheath is thus represented by the following equations, presented in the form needed for Runge-Kutta solution:

$$\frac{\partial \eta}{\partial y} = -\varepsilon, \tag{5.2}$$

$$\frac{\partial \varepsilon}{\partial y} = N_i - \exp \eta, \tag{5.3}$$

$$\frac{\partial N_i}{\partial y} = -\frac{N_i}{u_i}\frac{\partial u_i}{\partial y} + \frac{N_n N_e}{u_i}\tilde{R}_i, \tag{5.4}$$

$$\frac{\partial u_i}{\partial y} = \frac{\varepsilon}{u_i} - u_i \alpha \tilde{\sigma} N_n, \tag{5.5}$$

where $\alpha = n_o \lambda^3$, and $\tilde{\sigma}$ is the non-dimensional momentum exchange collision cross section for the propellant, given by

$$\tilde{\sigma} = \frac{\pi^2}{2\lambda^2} \sum_j d_j^2 X_j, \tag{5.6}$$

where the extra factor of $\pi/2$ in the cross section forces the hydrodynamic sheath treatment to match the kinetic treatment [45]. Due to lack of knowledge of the chemical makeup of the ablated propellant during the PPI, it is assumed throughout this work that the ions and neutrals have the same elemental makeup, being that of the ablated propellant. In Eqn. 5.6, d_j is the variable hard sphere diameter of elemental compound j present in the propellant, and X_j is the mass fraction of element j in the propellant. Table 5.1 contains the mass fractions and diameters used that are taken from [9] (X_j values) and [46] (d_j values).

The $\tilde{R}_i$ in Eqn. 5.4 is the non-dimensional ionization rate. It was found after a series of representative cases that the effect of ionization collisions on the dynamics

Table 5.1: Propellant composition by mass, and variable hard sphere diameters used for momentum exchange collisions.

Species	X_j, JA2	X_j, XM39	$d(\times 10^{-10}$ m)
H	0.02345	0.03646	2.92 (H_2)
C	0.09251	0.2248	1.544[a]
N	0.1955	0.2969	4.17 (N_2)
O	0.6883	0.4418	4.07 (O_2)

[a]Atomic diameter used for carbon as variable hard sphere value could not be found.

of the plasma sheath was negligible for the range of conditions encountered here. For simplicity, ionization in the sheath has been neglected throughout this work.

For a collisional plasma sheath the ion inflow velocity at the bulk plasma interface, u_{io}, is not known [47]. The physical range will be at or below the Bohm velocity, $u_{io} = 1$. The exact ion inflow speed depends on the characteristics of the plasma source and the plasma-air interaction happening between that source and the sheath edge. For this reason the ion inflow speed is not known, but a reasonable range can be assumed. In this chapter, values for u_{io} of 0.3, 0.6, and 1 are used to see the effect that inflow velocity has on the sheath dynamics, specifically the convective heat flux reaching the propellant bed. It must be noted that changing the inflow velocity changes the ion flux into the sheath, as $N_i = 1$ at the sheath edge for all cases.

The propellant bed is taken to be a floating wall, with the potential at the bulk plasma interface defined as $\eta_o = 0$. With the variable ion flux, the derivation of the floating potential yields

$$\eta_w = -\ln\left(\frac{1}{N_i u_i}\sqrt{\frac{m_i}{2\pi m_e}}\right), \tag{5.7}$$

where m_e is the electron mass. Note that with ionization neglected, the ion flux is constant across the sheath, such that $N_i u_i = u_{io}$. The Runge-Kutta method stops integrating when $\eta = \eta_w$.

A non-zero initial electric field is assumed to obtain the initial potential gradient that is consistent with a sheath solution. An initial value was used for a number of representative simulations in the range $10^{-8} \leq \varepsilon_o \leq 10^{-4}$, with there being no change in the simulation results over this variation. Thus the initial electric field is arbitrary for the solution as long as it lies within this broad range.

5.2.1 Results at Fixed Neutral Density

Before coupling the sheath to the ablation model it is beneficial to examine some results for fixed background neutral density, N_n, as they warrant discussion. The initial conditions assume a bulk plasma ($y = 0$) in the vicinity of the sheath with a small electric field, $\varepsilon_o = 10^{-5}$; grounded potential, $\eta_o = 0$; no charge separation, $N_i = N_e$; and no background neutrals, $N_n = 0$. At the beginning of the simulation the ions begin to experience a drag force due to the second term on the right hand side of Eqn. 5.5. If this drag force is not immediately overcome by the electrostatic acceleration term in Eqn. 5.5 then the ions slow down. Due to continuity (Eqn. 5.4) the ions begin to pile up near the interface. Since the electrons are non-collisional, eventually the charge separation is great enough that the electrostatic term in Eqn. 5.5 overcomes the drag term and the ion density begins to drop off again.

In Figs. 5.2 and 5.3, representative sheath solutions for fixed neutral density are shown. Figure 5.2 represents a classic sheath solution, with only a small rise in ion density after the inflow, due to the ion-neutral collisions. Figure 5.3 shows a typical buildup in ion density for the sheath model in the strongly collisional regime. As

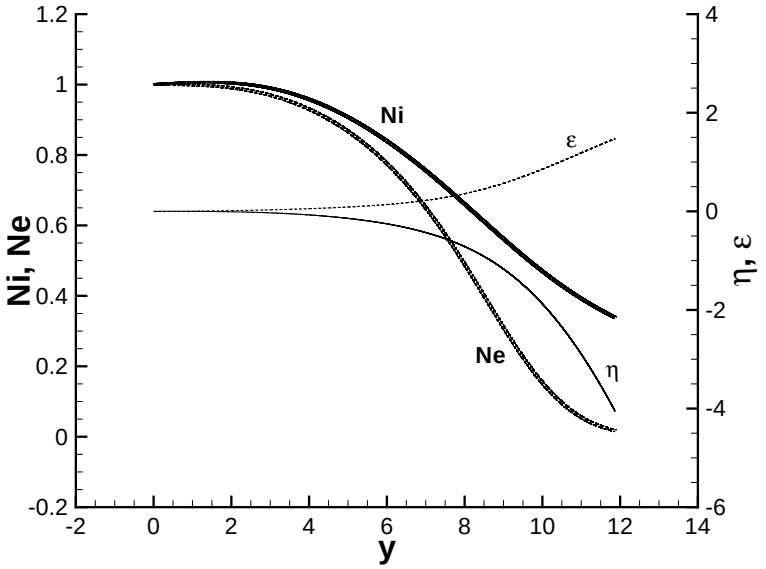

Figure 5.2: Sheath solutions at constant neutral density for JA2 where $u_{io} = 1$, $n_o = 10^{22}$ m^{-3}, and $N_n = 10$.

the neutral density is increased, the ion density peak becomes higher and thinner. Sheridan and Goree briefly mention this effect in [48], however these profiles had not been published prior to [40]. The cold ion, Runge-Kutta formatted model employed here is common in collisional sheath modeling, and these results, although physical for the conditions imposed, can be considered a limitation in this approach. It should be noted that for strongly collisional sheaths, this model returns the analytical results for a fully collisional sheath, as expected.

5.2.2 Coupling to the PPI Model

Coupling the sheath model to the ablation model allows for the determination of the sheath dynamics over the course of the plasma pulse, Δt=280 μs [37]. With the propellant surface temperature profile and a model for the vapor pressure of each propellant (Chapter IV), the neutral density in the sheath is given as

$$n_n = \frac{P(T_s)}{kT_s},$$

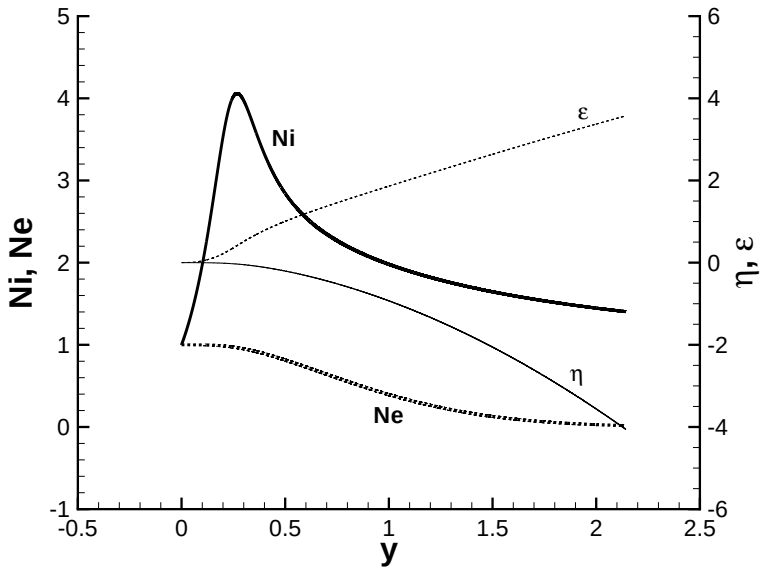

Figure 5.3: Sheath solutions at constant neutral density for JA2 where $u_{io} = 1$, $n_o = 10^{22}$ m^{-3}, and $N_n = 10^4$.

where $P(T_s)$ is the propellant vapor pressure at surface temperature T_s, and k is Boltzmann's constant. Since T_s is a function of time in the PPI model, the background neutral density is thus given as a function of time during the plasma pulse. By discretizing the pulse time it is possible to solve the steady state sheath equations under each neutral density condition and patch these solutions together to obtain the time evolution of the sheath. Implicit in this assumption is that the formation time of the sheath is much less than the discretization of the pulse duration. The formation time of the sheath can be estimated as λ/v_i, which is on the order of 10^{-11} seconds, or less, for the cases shown here. The pulse discretization is typically on the order of 10^{-9} seconds or more.

The convective heat flux reaching the propellant bed, q_{conv}, as a function of time during the plasma pulse can now be calculated for a range of bulk plasma densities. The convective heat flux to the propellant bed, under the assumption of no ionization

in the sheath, is

$$q_{\text{conv}} = (n_o C_s u_{io}) \left(\frac{m_i}{2} (C_s u_{iw})^2 + 2eT_e - eT_e \eta_w \right), \tag{5.8}$$

where u_{iw} is the ion-wall impact velocity [20]. The first term in Eqn. 5.8 is the kinetic energy of the ions impacting the wall. The second and third terms represent the electron impact energy, with the former being the kinetic energy of Maxwellian electrons, and the latter an energy bias, as only electrons that can overcome the potential hill of the sheath can strike the wall [20]. A full derivation of Eqn. 5.8 is presented in Appendix B.

5.3 Coupled Model Results

In this section the sheath model is coupled to the PPI model developed in Chapter IV. Section 5.3.1 presents results first published in [40] using the semi-analytical ablation model discussed in the previous chapter and originally published in [37]. Due to the fact that the data presented is illustrative in nature, these figures are not regenerated using the surface temperature profiles from the updated PPI model data, as differences are minor. Section 5.3.2 presents the results utilized in the ETC model, which are obtained from the updated PPI model data outlined and presented in Chapter IV, as direct conclusions regarding the PPI are drawn from these results. In Section 5.3.1 the plasma pulse is discretized into ten segments, resulting in a timestep of 2.80×10^{-5} s. In Section 5.3.2 the sheath model is integrated directly into the PPI code, rather than executed in post-processing, thus it is possible to use a much smaller timestep. The timestep for the coupled sheath/PPI model is 2.80×10^{-9} s. Since the sheath model calculates the average convective heat flux by averaging the convective heat flux at each timestep, the primary result of a smaller timestep is a more accurate estimate of the convective heat flux over the course of

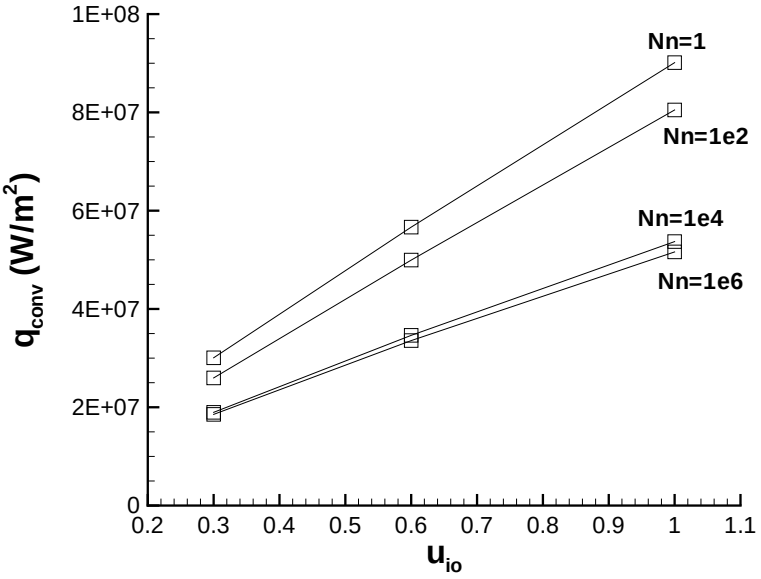

Figure 5.4: Representative convective heat flux versus ion inflow velocity at fixed neutral density for JA2 at $n_o = 10^{22}$ m^{-3}.

the PPI, provided that the formation time of the sheath is still much less than the timestep in the sheath model.

5.3.1 Time Accurate Sheath Limits

A representative plot of the convective heat flux versus ion inflow velocity at a range of constant background neutral densities for JA2 is shown in Fig. 5.4. Clearly, there is a correlation between neutral density and convective heat flux; as neutral density increases, the convective heat flux decreases. This has a large impact when coupled with the ablation model, since as time progresses the surface temperature increases, which increases the vapor pressure and thus the neutral density. This can clearly be seen for the representative case presented in Fig. 5.5, which shows the propellant surface temperature and associated neutral density for JA2 taken from [37], while Fig. 5.6 shows the model results for convective heat flux versus time over the course of the plasma pulse.

The corresponding plots of surface temperature, neutral density and convective

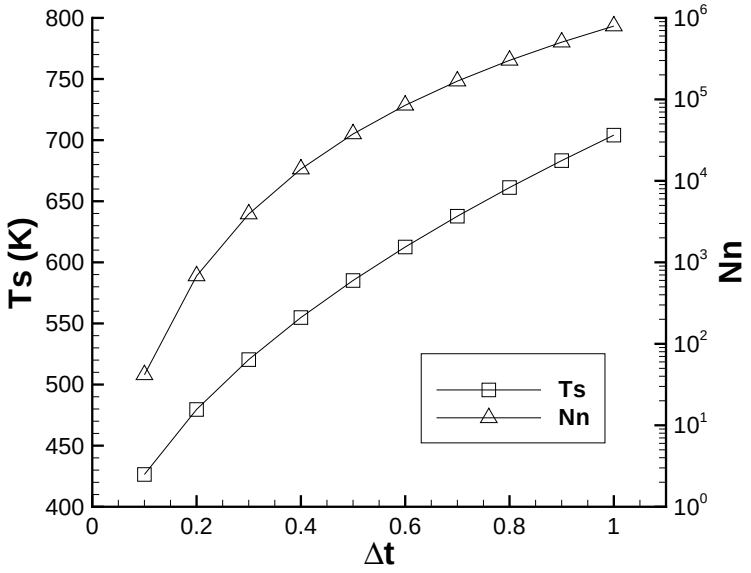

Figure 5.5: Surface temperature and neutral density for JA2 at $n_o = 3 \times 10^{22}$ m^{-3}.

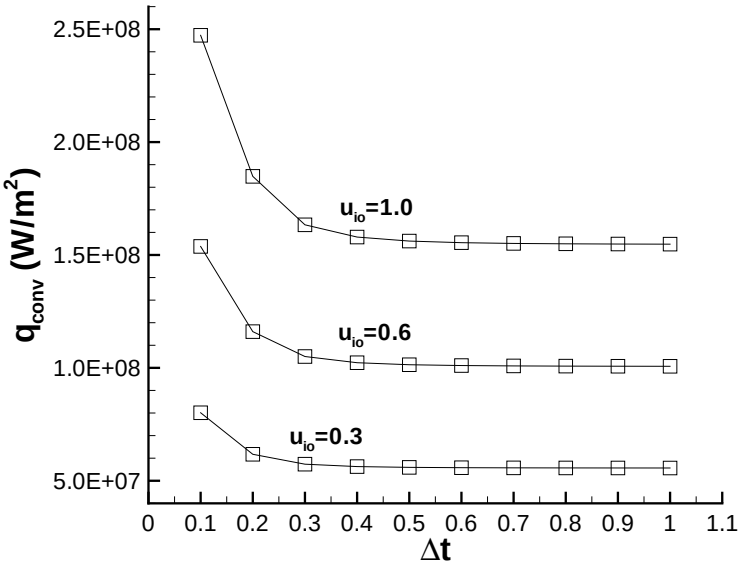

Figure 5.6: Convective heat flux for different ion inflow velocities for JA2 at $n_o = 3 \times 10^{22}$ m^{-3}.

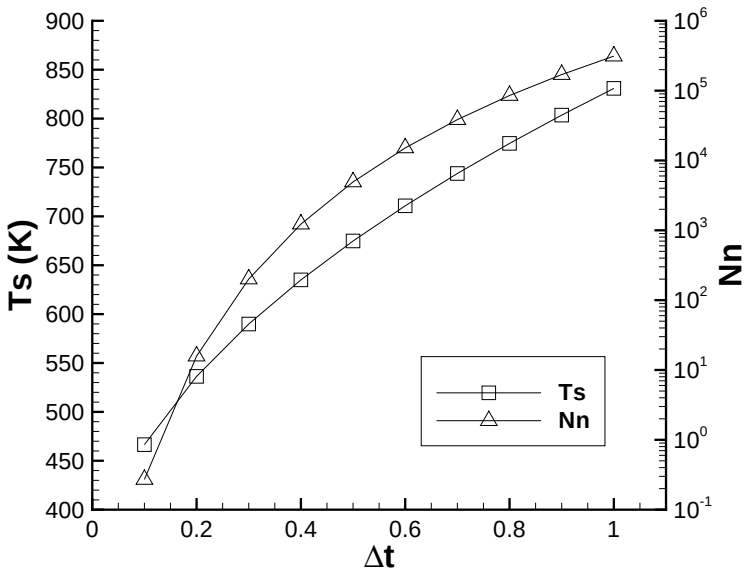

Figure 5.7: Surface temperature and neutral density for XM39 at $n_o = 3 \times 10^{22}$ m^{-3}.

heat flux for XM39 are shown in Figs. 5.7 and 5.8, for the same bulk plasma density. Note that XM39 exhibits a higher convective heat flux than does JA2. In these illustrative cases there is a noticeable difference in the curvature of the convective heat flux for XM39 compared with that of JA2 early in the plasma pulse. This is easily explained by examining the neutral density near the start of the pulse. The initial neutral density is on the order of $N_n = 0.1$ for XM39, indicating that the plateau approached on the left hand side of Fig. 5.8 is actually the collisionless sheath limit. It stands to reason that the level plane reached on the right of Fig. 5.8 is the fully collisional sheath limit.

Examining Eqn. 5.8, one discovers that all variables are defined analytically, such as η_w, or found from the PPI model, as N_n is. The only unknown that is needed from the sheath model is u_{iw}, the ion-wall impact velocity. Analytical solutions exist for the ion-wall impact velocity in the extremes of collisionless and fully collisional sheaths [48]. With these values known, the analytical solutions can simply be substituted into Eqn. 5.8 to calculate the convective heat flux for these two limiting cases

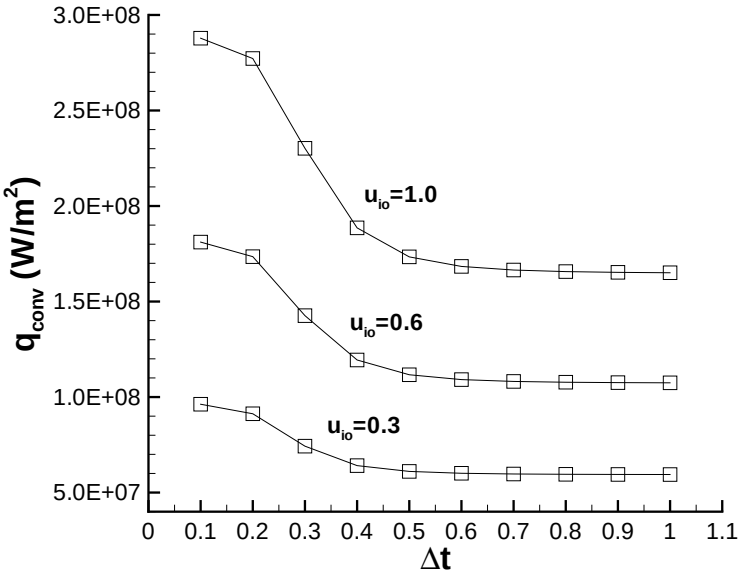

Figure 5.8: Convective heat flux for different ion inflow velocities for XM39 at $n_o = 3 \times 10^{22}$ m^{-3}.

at each timestep. In the fully collisional sheath limit, the ion-wall impact velocity is given by

$$u_{iw} = \left(\frac{5}{2} \frac{-\eta_w u_{io}}{(\alpha N_n \tilde{\sigma})^2} \right)^{1/5} . \tag{5.9}$$

For the collisionless limit the result is more complicated, yielding

$$u_{iw} = \left[2 \left(\frac{u_{io}^2}{2} - \eta_w \right) \left(1 - \frac{4\sqrt[4]{2}}{7} \, \alpha N_n \tilde{\sigma} \, \frac{(-\eta_w)^{3/4}}{\sqrt{u_{io}}} \right) \right]^{1/2} , \tag{5.10}$$

which relies heavily on analysis from Child's Law [48]. These asymptotic values are compared to the simulation results and are found to yield excellent agreement for the highly collisional end of the heat flux, indicating that toward the end of the plasma pulse the sheath belongs to the fully collisional regime. For most cases the sheath is never collisionless, as the non-dimensional neutral density is generally greater than one at all timesteps. The sheath is in a transition regime, neither collisionless nor fully collisional, for a significant fraction of the plasma pulse for most data sets.

One of the best cases for illustration is shown in Fig. 5.9, which is the $u_{io} = 1$ case from Fig. 5.8. At Δt=0.1 the sheath is nearly collisionless. At Δt=0.2 the

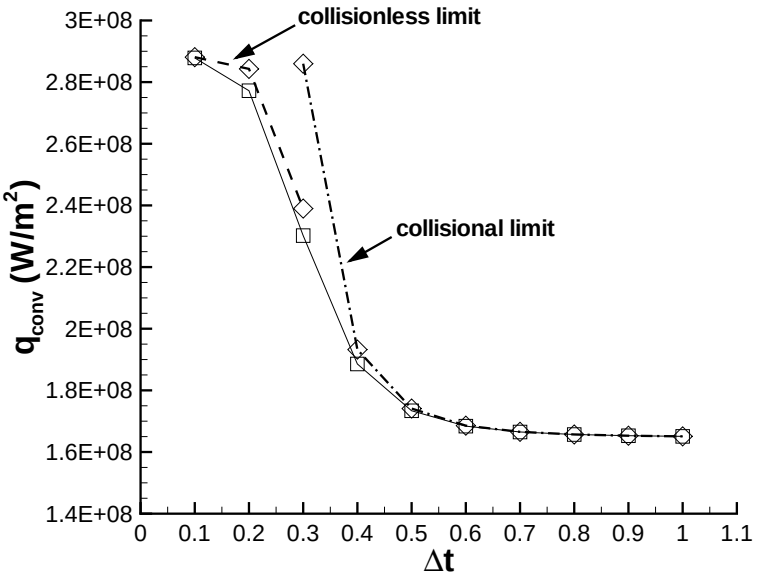

Figure 5.9: XM39 at $n_o = 3 \times 10^{22}$ m^{-3}, $u_{io} = 1$. A representative simulation result as compared to the convective heat fluxes for a collisionless sheath and a fully collisional sheath.

simulation result has deviated from the collisionless solution, indicating that the sheath has entered a transition regime that continues until Δt=0.6. The simulation makes a smooth transition from near collisionless to fully collisional.

5.3.2 Average Convective Heat Flux

Since the total heat flux, q_{total}, obtained from the PPI model of Chapter IV, is constant over the course of the plasma pulse, the relevant convective heat flux needed for comparison is the time average. The time average convective heat flux, $q_{\text{conv,avg}}$, obtained from the coupled sheath/PPI model is shown in Fig. 5.10 for ion inflow velocities of u_{io}=0.3 and 1.0. For a given combination of bulk plasma density and ion inflow velocity, XM39 has a higher convective heat flux than JA2. However, as discussed in Chapter IV, JA2 has a higher total heat flux than XM39 at a given bulk plasma density. Since JA2 is susceptible to plasma radiation, and XM39 is not, it is expected that JA2 will have a higher radiative heat flux. The data presented here

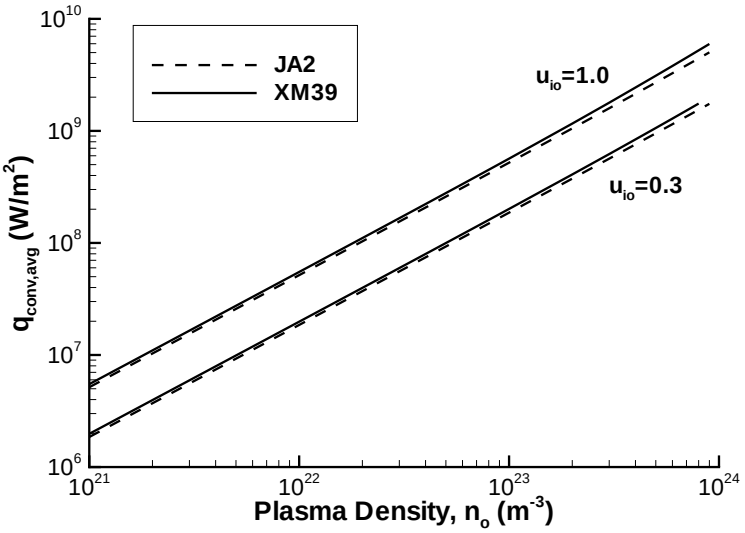

Figure 5.10: Time average convective heat flux for each propellant as a function of bulk plasma density and ion inflow velocity.

indicates that the importance of radiation is even more pronounced. Not only does JA2 have a higher radiative heat flux than XM39, but the fact that JA2 has a lower convective heat flux requires that JA2 receives even more of it's total energy from radiation than previously thought. JA2 must absorb enough radiative energy to not only meet, but exceed, the amount of energy XM39 receives from convective heat flux alone.

As ion inflow velocity decreases, so does the convective heat flux. This can be easily understood by examining Eqn. 5.8. Recall that the particle flux into the sheath is given by $n_o C_s u_{io}$. As u_{io} decreases, the particle flux into the sheath decreases, which intuitively will decrease the convective heat flux to the wall. Of course, u_{iw} will also change in the sheath solution if a lower initial velocity is used, however, the main contribution to the difference seen between ion inflow velocities in Fig. 5.10 is due to the change in particle flux entering the sheath.

Knowing the total heat flux from Chapter IV, and the average convective heat

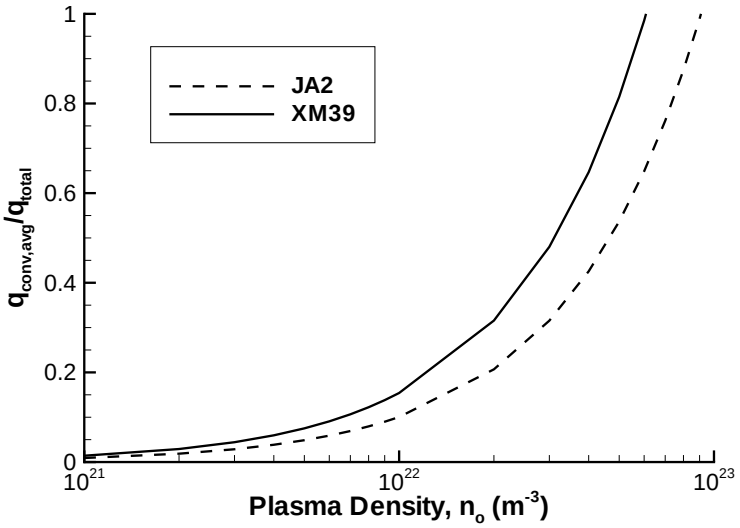

Figure 5.11: Fraction of the total heat flux that is accounted for by the convective heat flux for u_{io}=0.3.

flux, it is now possible to determine what fraction of the propellant's total heat flux is made up of convective heat flux. Figures 5.11 and 5.12 show the fraction $q_{\text{conv,avg}}/q_{\text{total}}$ for u_{io}=0.3 and 1.0, respectively. Data is only shown up to $q_{\text{conv,avg}}/q_{\text{total}}$=1, since any value above this point is contradictory, as the convective heat flux would be higher than the total heat flux. Here, as in Chapter IV, the bulk plasma density is treated parametrically. In the next chapter, concerning the combined ETC model, the bulk plasma density will be solved for exactly.

5.4 Conclusions

In this chapter, a collisional plasma sheath model was developed for ETC application. The model finds that XM39, an optically opaque propellant, has a higher convective heat flux than JA2, which is semi-transparent. Since the PPI model indicates that JA2 has a higher total heat flux than XM39, it is concluded that plasma radiation is an important heat source in the plasma-propellant interaction.

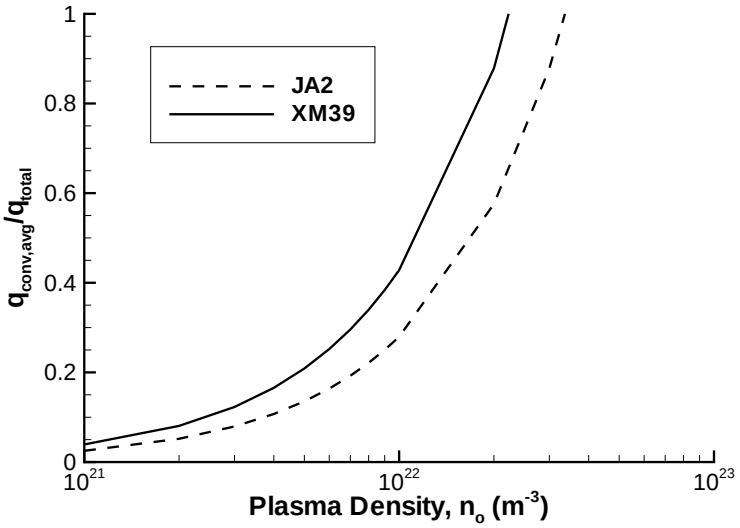

Figure 5.12: Fraction of the total heat flux that is accounted for by the convective heat flux for u_{io}=1.

This simulation data reaffirms previous conclusions from modeling and experimental work that when picking a propellant for ETC application, the optical properties can not be ignored, and that the best choice for ETC gun propellant is one which allows plasma radiation to penetrate it's interior.

Results clearly show that the sheath can begin in the near collisionless regime, undergoing a smooth transition to the fully collisional regime before the end of the plasma pulse. In all cases, most of the time the sheath is fully collisional, thus if an analytical limit must be used to calculate the convective heat flux, the fully collisional limit (Eqn. 5.9 with Eqn. 5.8) is the best option. Although this study indicates that having a low vapor pressure would increase the convective heating of the propellant, it is known that this would also result in a lower ablation rate, which is a negative effect to ETC ignition overall. It is also unknown how much radiation shielding is occurring due to ablated propellant neutrals, and perhaps there is an optimum balance between ablation and radiation shielding to yield the ideal vapor

pressure for ETC application.

The results of this chapter, and the previous one, treat bulk plasma density parametrically. In the next chapter the work of Chapters II—V will be combined to yield the end-to-end electrothermal chemical gun model that is the final result of this thesis. In this final model, the bulk plasma density will be solved for via CFD, and will no longer be treated parametrically.

CHAPTER VI

Model Integration

This chapter presents the combined end-to-end electrothermal chemical gun model that is the major result of this thesis. The models presented in Chapters II—V are combined to determine the total and convective heat flux reaching JA2 and XM39 in an experiment that measured the total mass loss after the plasma-propellant interaction. The data and conclusions presented in this chapter are given here for the first time.

6.1 The Combined (E3TC) Model

A flowchart, outlining the coupling and data flow in the end-to-end electrothermal chemical gun model, is shown in Fig. 6.1. For ease, the combined end-to-end electrothermal chemical gun model is abbreviated throughout the rest of this thesis as the E3TC model. This section will outline how the previously presented models are coupled, as well as briefly recapping the input and output of each. Note that data in the combined model only flows in one direction, allowing each submodel, represented as blocks in Fig. 6.1, to run independently of the other models, thus requiring only weak coupling in terms of programming.

The capillary model (Chapter II) simulates the polyethylene capillary plasma

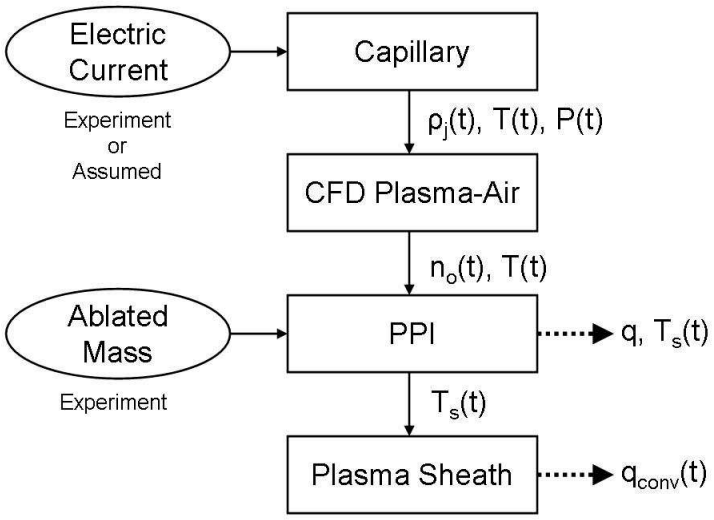

Figure 6.1: Diagram of the E3TC model.

generator that is used to ignite the solid propellant, and is the source of the plasma in the plasma-propellant interaction. As input, the capillary model requires the supplied electrical discharge current. This can come either from an experiment, as is the case in this chapter, or it's shape can be assumed, as it was in Chapter II for the capillary parameter study. As output, the capillary model generates time varying data for outflow temperature, T, outflow pressure, P, and the mass density of each fluid species (C, C^+, H, H^+, e^-).

The CFD plasma-air chemistry model (Chapter III) simulates the expanding capillary plasma jet before interaction with the propellant surface. As inflow boundary conditions, it only requires the output from the capillary model, fitted to high order polynomials. The CFD model provides an abundance of information on the plasma-air chemistry happening in the jet. This chemistry information may be used in a future model to analyze possible plasma-surface chemistry and how it affects the PPI; a possibility that will be discussed in Appendix C. In the E3TC model as it now exists, this detailed chemistry information is passed out of the CFD code, but

is not used by the PPI model, as only the total ion number density is needed. The fluid temperature and species number density at the location that the propellant is located (further explained in Section 6.2), as a function of time, is output. The number density of ions—or alternatively, the number density of the electrons, as the plasma is quasi-neutral—is defined as the bulk plasma density, n_o, in the PPI model. As it is assumed that the plasma is in equilibrium. The single temperature simulated in the CFD model is taken to be the plasma temperature in the PPI model.

With the bulk plasma density known, the parametric nature of the PPI model solutions, illustrated in Figs. 4.5 and 4.6, is eliminated. Furthermore, a time varying plasma temperature is incorporated into the model, which had previously not been used, as a constant T_e=1.5 eV had been assumed based on the results of the capillary parameter study. As emphasized in Chapter IV, the PPI model requires the experimentally determined ablated mass due to the plasma-propellant interaction in order to find the total heat flux to the propellant surface. The PPI model generates the total heat flux to the propellant surface, q, which is the primary output of the E3TC model. In order to perform the calculation necessary to find q, the propellant surface temperature as a function of time must be found, and is itself useful in analysis of the PPI. The PPI model then passes this time varying propellant surface temperature to the sheath model for determination of the convective heat flux reaching the propellant bed, q_{conv}. This convective heat flux is then time averaged for direct comparison to the total convective heat flux.

6.2 Experimental Setup

The results presented in this chapter model the experiment that determined the propellant ablated masses used throughout this thesis [5]. The capillary inflow used

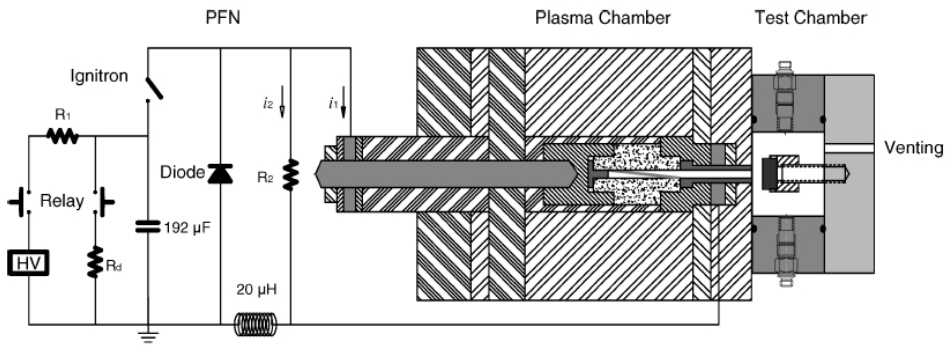

Figure 6.2: Experimental geometry used in the E3TC model, taken from [5].

in this chapter is the same as that used in Chapter III, and is covered in detail in Section 2.4, with no further elaboration needed or presented here.

The CFD geometry used is designed to match the experimental plasma jet expansion chamber. Figure 6.2 shows a diagram of the experimental setup, taken from [5], where the CFD simulation covers the area labeled "Test Chamber". Based on the dimensions of the test chamber, the following CFD geometry, shown in Fig. 6.3, was used in the E3TC model. A capillary nozzle is simulated, with a radius of 1.6 mm and length of 26 mm. The temperature at the wall boundary condition in the nozzle was set such that the wall temperature is the same as the temperature in the adjacent cell, resulting in no thermal gradients at the wall. This was done because the nozzle wall temperature is not known, and this option is preferable to imposing an arbitrary temperature. In the future, estimates of this wall temperature could be made and used in the simulation, providing the nozzle material is known.

The distance from the capillary nozzle exit to the right boundary of the simulation is 25 mm. Again, the axisymmetric nature of the problem is exploited, with an axisymmetric boundary condition at y=0, and a wall located at x=26 mm. The far right and top boundaries are outflow. An outflow condition was used at the right boundary where the data is collected because it was felt that a wall boundary

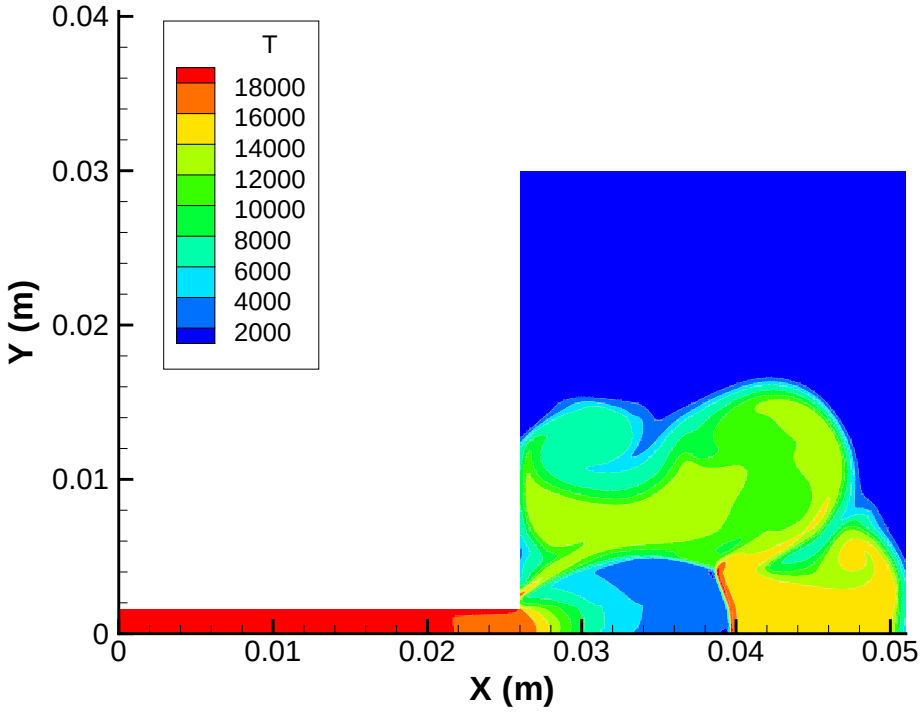

Figure 6.3: Plasma jet temperature contours (K) taken at t=35 μs, used to illustrate the CFD geometry.

condition could alter the results due to imposed CFD boundary conditions that would artificially affect the plasma temperature and density.

Based on the CFD simulations of Chapter III, a uniform grid spacing of Δx=0.1 mm, and a timestep of Δt=2.5×10^{-9} s are used. Outflow data is recorded at each timestep from the first cell above the symmetry line at x=51 mm. It was decided that simulating the propellant sample holder and extracting wall data, rather than outflow data, would result in undesirable phenomena. The wall boundary conditions force the plasma temperature and pressure to meet certain CFD conditions that may not be meaningful here. For instance, the plasma temperature would drop and the plasma pressure would increase. Since the PPI and sheath models require the bulk properties, it is questionable to use these results. Thus, unimpeded jet flow was modeled here.

The output from this CFD cell is then used to determine the bulk plasma density and temperature for use in the PPI model. The bulk plasma density is defined as

$$n_o = n_{N^+} + n_{O^+} + n_{C^+} + n_{H^+}. \tag{6.1}$$

Results of the simulation clearly show that n_{N^+} and n_{O^+} contribute a negligible fraction to the total plasma number density, however, they are included in the calculation of n_o for completeness. As in Chapter IV, the total propellant ablated masses of 5.3 mg for JA2 and 2.8 mg for XM39 are obtained from the experiment [5] and used to fix the total heat flux.

The propellant surface temperature as a function of time, generated by the PPI model, is used to calculate the convective heat flux at a range of ion inflow velocities via the plasma sheath model developed in Chapter V.

6.3 Results

This section presents the results of the E3TC model. Detailed discussion of the results are postponed until Section 6.4, when the results of the model can be viewed as a whole. No discussion of the results obtained purely from the capillary model is presented, as this same input was used in Chapter III, and discussion can be found there.

6.3.1 CFD Plasma Jet Chemistry

The relevant output obtained from the CFD code is shown in Fig. 6.4. Although only n_o and T are required, the data for n_{C^+} and n_{H^+} is included to show how the bulk plasma density is decomposed. Clearly, a majority of the plasma is made up of hydrogen ions. Peak plasma density is on the order of 2×10^{24} m^{-3}.

Ideally, the data shown in Fig. 6.4 would be coded directly into the PPI model.

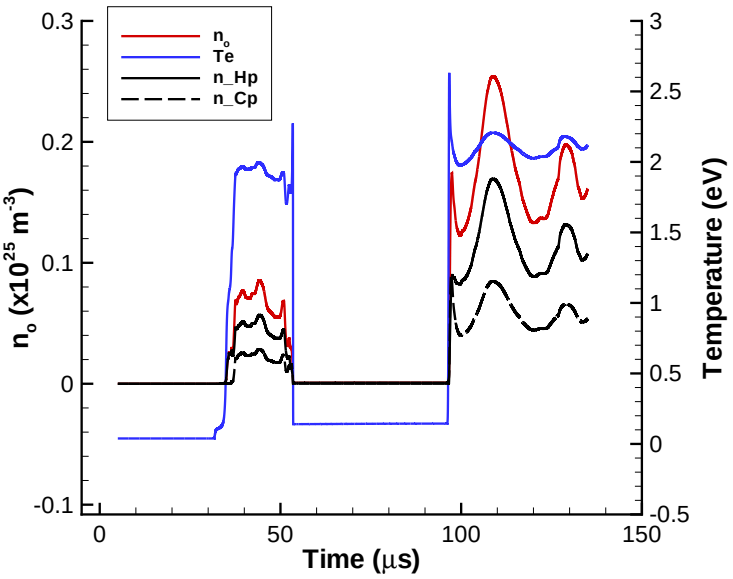

Figure 6.4: Bulk plasma density and temperature, as determined by the CFD code in the E3TC model.

Although there is nothing in the model or the data that prohibits this, an alternative method was selected for a number of reasons. Due to the fluctuations and spikes visible in the data, a series of plateaus were used in which each has a single plasma density and temperature. The values of the plateaus were found by averaging the values in each region, avoiding any significant spikes in the data, which would skew the averages. Secondly, due to time constraints, the CFD simulation was not able to run to completion. Ideally, the plasma density and temperature, as a function of time, would be found over the course of the entire capillary discharge. The approximately 140 μs of time simulated here required over 158 hours of computation time running on thirty 2 GHz processors. Since the simulation could not be concluded, an approximation was made that the value of the last plateau continues until the end of the plasma discharge, 280 μs after the plateau begins. The plateaus are shown in Figs. 6.5 and 6.6 for plasma density and temperature, respectively.

Careful examination of the CFD temperature and density contours at various

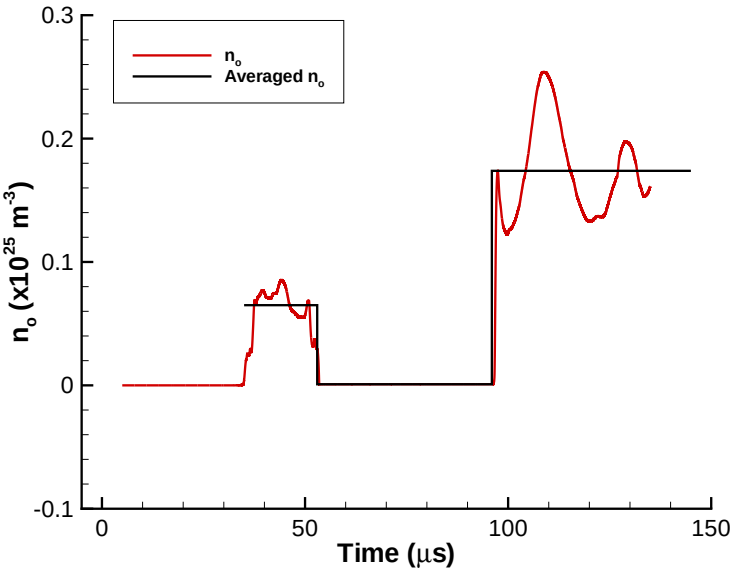

Figure 6.5: Bulk plasma density raw data and plateau fits for use in the PPI model.

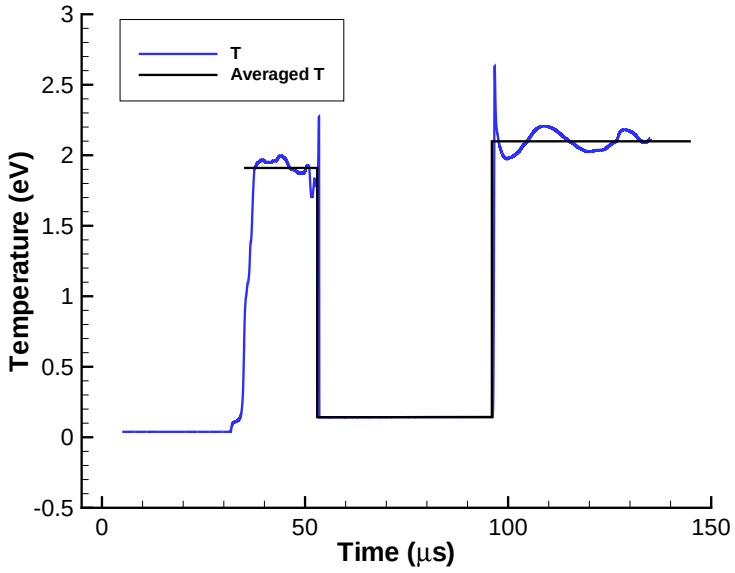

Figure 6.6: Plasma temperature raw data and plateau fits for use in the PPI model.

Table 6.1: Plateau values and times used in the PPI model. Times are shifted from the CFD data of Fig. 6.4 so that t=0 is the start of the PPI.

Start Time (μs)	End Time (μs)	n_o(m^{-3})	T(eV)
0	18	6.48×10^{23}	1.91
18	60	8.85×10^{21}	0.143
60	340	1.74×10^{24}	2.10

times during the simulation show that the first plateau, starting at t=35 μs, corresponds to the arrival of the precursor shock, and is the beginning of the plasma-propellant interaction. The second plateau has a significantly lower density and temperature than the first plateau, but is still able to cause propellant ablation. The third plateau represents the bulk of the plasma, as the preshock structure has completely passed at this time. The third plateau continues for 280 μs. The exact values obtained for the plateaus are shown in Table 6.1, where the times have been shifted such that t=0 is the start of the plasma-propellant interaction.

6.3.2 The Plasma-Propellant Interaction

With the plateaus listed in Table 6.1 programmed into the PPI model, the range of heat flux is iterated over to find the total heat flux that matches the experimentally determined ablated mass, for each propellant. The range of total ablated mass, as a function of the surface temperature at the end of the PPI, is shown in Fig. 6.7 for each propellant. The horizontal lines that intersect the curves correspond to the experimental ablated mass for each propellant. The total heat flux matching the experimental ablated mass is 1.29×10^8 W/m^2 for JA2 and 9.67×10^7 W/m^2 for XM39. The conclusion from Chapter IV that JA2 always has a higher total heat flux clearly continues to hold here. So does the conclusion that XM39 consistently

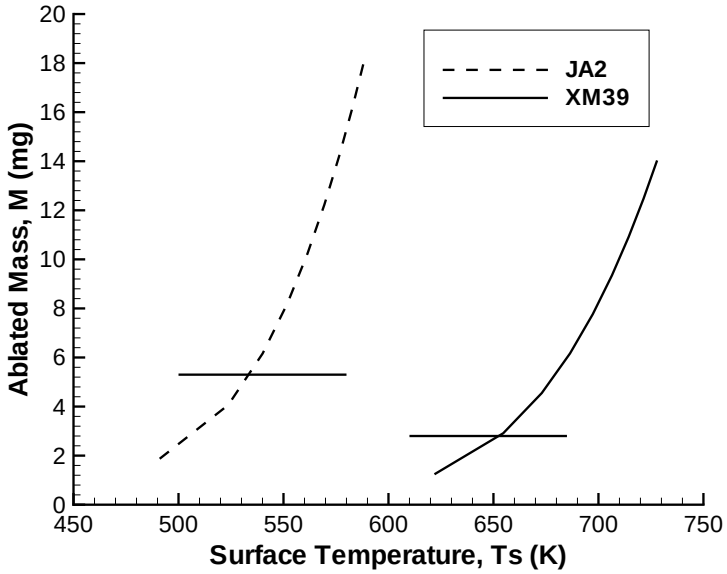

Figure 6.7: Total ablated mass for each propellant as a function of the surface temperature at the end of the PPI.

has a higher surface temperature, illustrated by Fig. 6.7.

Due to the varying plasma density and electron temperature, the propellant surface temperature versus time profiles are worth noting. In order to reproduce the exact surface temperature profiles, the PPI model was run using the heat flux found via interpolation of Fig. 6.7 that reproduced the experimental total ablated mass. The propellant surface temperature profiles are shown in Fig. 6.8. The divisions between the three plateau regions are clearly visible. An interesting change happens after the second plateau; the surface temperature drops significantly and appears to reach an equilibrium value. This can be explained by the changes in bulk plasma density. At the same surface temperature, a higher bulk plasma density yields a higher ablation rate, as evidenced by the ablation rate contours show in Figs. 4.3 and 4.4. As the ablation rate increases, the equilibrium surface temperature decreases, as evidenced in the PPI thermal model boundary condition of Eqn. 4.4, and

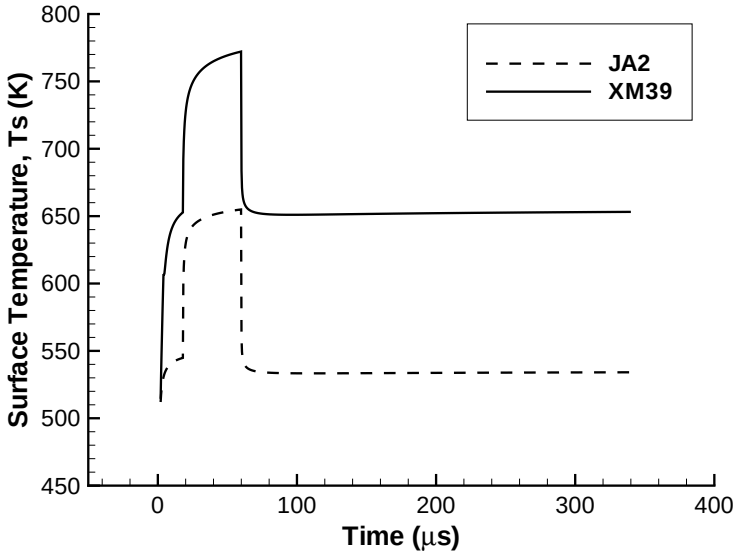

Figure 6.8: Propellant surface temperature as a function of time.

reproduced below.

$$\frac{\partial T_s}{\partial x} = -\lambda^{-1}(q - \Delta H\Gamma - C_p(T_s - T_o)\Gamma)$$

As the ablation rate, Γ, increases, heat is carried away from the surface at an increasing rate. Since the total heat flux, q, is constant, the only way to reach an equilibrium is to settle onto a new equilibrium surface temperature. The ablation rate for each propellant is shown in Figs. 6.9 and 6.10, for JA2 and XM39, respectively. Note that XM39 has a lower ablation rate than JA2, resulting in it's higher surface temperature. The phenomenon that occurs when the PPI model reaches the third plateau is quite interesting. The surface temperature is high, but when the plasma density increases the ablation rate increases. This new ablation rate then rapidly carries away a large amount of heat from the surface, dropping the ablation rate (see Figs. 6.9 and 6.10 at $t \approx 65$ μs). Since the temperature was much higher than the "new" equilibrium temperature for the third plateau, the surface temperature drops rapidly until it hits the equilibrium temperature, remaining there for the

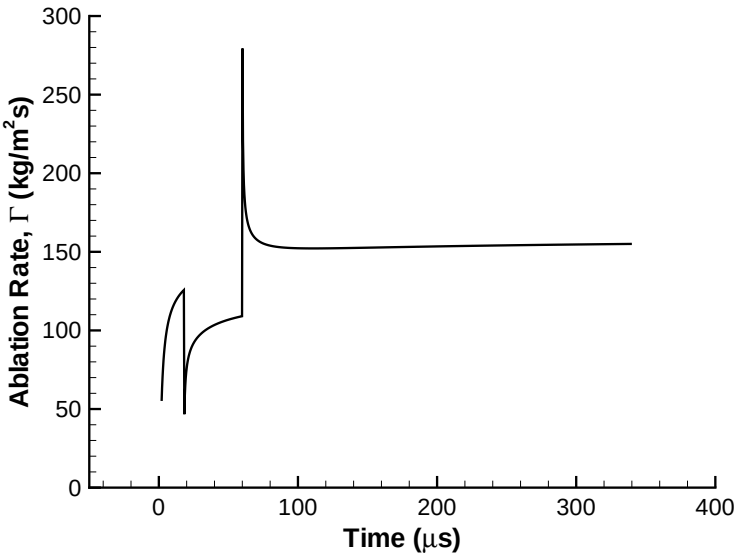

Figure 6.9: Ablation rate for JA2 as a function of time.

rest of the PPI. Note that Fig. 6.8 shows that the peak surface temperature is not at the end of the PPI, but occurs in the first one third of the PPI, a fact that should be taken into account when viewing Fig. 6.7, although the relative difference between propellant temperatures remains approximately the same.

6.3.3 Convective Heat Flux

The convective heat flux reaching each propellant was calculated from the plasma sheath model at ion inflow velocities of u_{io}=0.3 and 1.0. The exact total heat flux needed to reproduce the experimental total ablated mass for each propellant was used, so that time accurate data on the convective heat flux could be obtained.

The results for the average convective heat flux are displayed in Table 6.2 for both propellants and ion inflow velocities. The sheath simulation indicates that, for the plasma density and temperature profiles used, the convective heat flux is higher than the total heat flux for each propellant, which is not physically possible. Theories as to what is happening are presented in Section 6.4. One general trend to note is

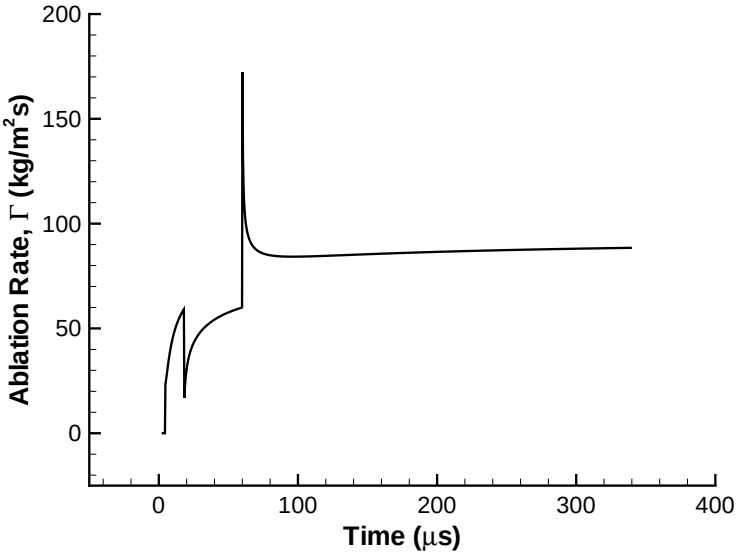

Figure 6.10: Ablation rate for XM39 as a function of time.

Table 6.2: Total and convective heat flux at different ion inflow velocities for both propellants.

Propellant	q_{total} (W/m^2)	$q_{\text{conv,avg}}$ (W/m^2)		$q_{\text{conv,avg}}/q_{\text{total}}$	
		u_{io}=0.3	u_{io}=1.0	u_{io}=0.3	u_{io}=1.0
JA2	1.29×10^8	4.87×10^9	1.44×10^{10}	37.6	111
XM39	9.67×10^7	5.68×10^9	1.74×10^{10}	58.8	180

that XM39 continues to have a higher convective heat flux than JA2, as previously observed in Chapter V.

The convective heat flux as a function of time during the PPI is shown in Fig. 6.11 for u_{io}=0.3, and in Fig. 6.12 for u_{io}=1.0. The transitional sheath is clearly visible as the curve at the beginning of the PPI in the convective heat flux for XM39. It is not surprising that, at such high bulk plasma density, the sheath is fully collisional for the bulk of the PPI. A very small transitional sheath is barely visible for JA2 in the figures.

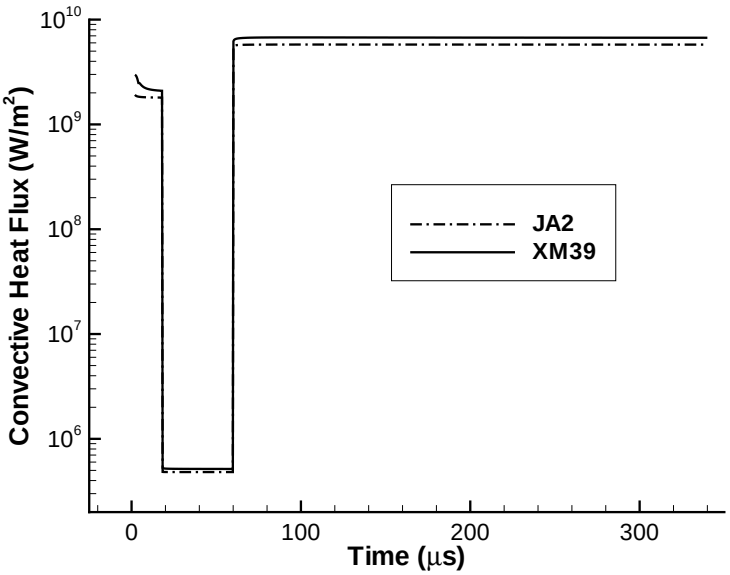

Figure 6.11: Convective heat flux for u_{io}=0.3, as a function of time.

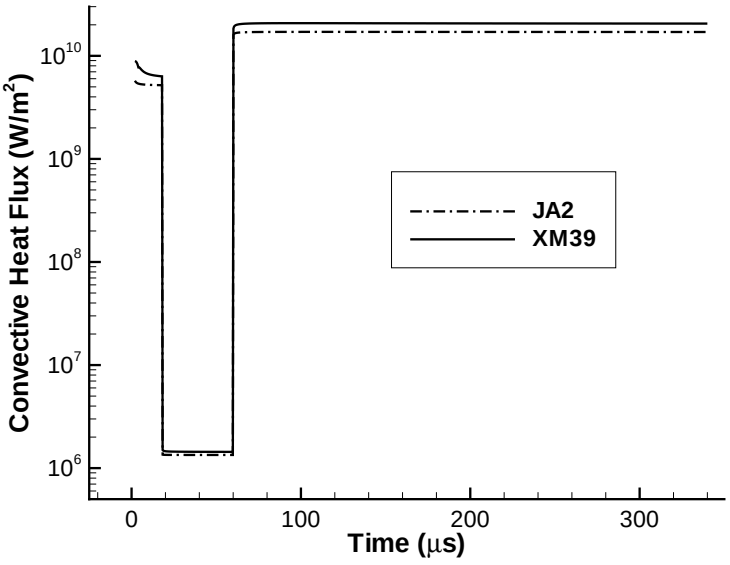

Figure 6.12: Convective heat flux for u_{io}=1.0, as a function of time.

6.4 Discussion of E3TC Model Results

This section contains discussion of the results from the E3TC simulation presented above. Theories are proposed to explain the anomalous results of the convective heat flux calculation.

One interesting result of the CFD submodel is that the plasma jet, even with a capillary-sample distance of greater than 10 mm, contains a negligible fraction of ionized air species. Based on the results of Case S3 in Chapter III, it was expected that there would be an initial spike in ionized air species as the precursor shock passed. This is not the case, and it is clear from Fig. 6.4 that the plasma in the jet is composed entirely of carbon and hydrogen ions. The fluctuations visible in the CFD output of Fig. 6.4 indicate the difficulty in using CFD data from a complex flowfield with the gas passing through numerous shock and expansion features (recall the discussion of the jet structure accompanying Fig. 3.2). The need to use average values for the plasma density and temperature can be considered a limitation in the current simulation, but not in the model as a whole, as time accurate data could be used in the E3TC model, if there was sufficient time for the CFD simulation to complete. That being said, the computational expense of the CFD portion of the E3TC model can be considered a major limitation, as it is the bottleneck for computational speed in the model.

The propellant surface temperature, as a function of time, obtained from the PPI model, demonstrates one of the limitations in using a constant total heat flux. There is no reason to expect the total heat flux to remain constant during the PPI. In fact, there are many reasons to expect it to change; the change in ablated particle density over time would very likely lead to time varying radiation shielding, just as

the convective heat flux changes over time. Unfortunately, there is at present no way to accurately tell how the total heat flux will change during the PPI. If such a measurement were possible then the model would be able to use that data to determine the total ablated mass, rather than the total heat flux. This need to use a constant total heat flux is a major limitation in the E3TC model, with no foreseeable correction, short of modeling all other heat sources in the PPI in a time accurate manner.

The E3TC model provides an estimate of the total heat flux that reached the propellant bed in the experiment [5]. It supports previous conclusions that JA2 receives more energy from the plasma than does XM39, with the most likely source of the additional energy being penetrating plasma radiation. The resulting total heat fluxes fall in the range established by treating the bulk plasma density parametrically in Chapter IV, which fall within an order of magnitude of estimates made via experimental data regarding the total radiation heat flux.

The results regarding convective heat flux require further examination. The sheath model predicts that the convective heat is higher than the total heat flux for the range of reasonable ion inflow velocities. There are four possible explanations for this discrepancy, outlined below. The true explanation could be any one of these theories, or a combination of the four.

1. The sheath model (Chapter V), is failing to take into account some features of the actual plasma sheath attached to the propellant surface. This explanation is very likely, as numerous assumptions are made in the sheath model. As is typical in sheath models, the cold ion assumption is made. This eliminates the density gradient term in the momentum conservation equation, allowing for the solution of the sheath equations via numerical integration. The CFD

simulation indicates that the ions are likely very hot, on the order of an electron volt. Secondly, the sheath model assumes a constant background neutral density, which may not be accurate. With high collisionality in the sheath, momentum transfer would likely occur in two directions (constant background density assumes momentum exchange from ions to neutrals, without the neutrals recoiling from the collision), which would affect the neutral density distribution over time. Furthermore, there is a different neutral density at each sheath timestep (calculated from the instantaneous surface temperature), with no hysteresis in the neutral density. An upgrade to a more complex sheath model that takes these factors into account could result in a more accurate estimate of the convective heat flux reaching the propellant bed. Additionally, the wall temperature boundary condition in the nozzle mentioned previously could alter the end temperature and plasma density from the CFD simulation.

2. As shown in Chapter V and Table 6.2, reducing the ion inflow velocity to the sheath, u_{io}, can drastically reduce the convective heat flux. As stated in Chapter V, this is mostly due to the reduction in the ion flux into the sheath, which scales as $n_o C_s u_{io}$. Although it was felt that u_{io}=0.3 was a good estimate for the lower limit for ion inflow velocity, it is possible that the real value could be lower. It should also be noted that it is possible that each propellant will have a different ion inflow velocity, resulting in further differences in convective heat flux for each propellant. It is possible to estimate, by extrapolation from existing simulation data, what ion inflow velocity will result in a convective heat flux equal to the total heat flux, for each propellant. This estimate can then be refined and confirmed by simulation. Conducting this study finds that the ion inflow velocity needed to force the time average convective heat flux to

match the total heat flux is $u_{io} \approx 0.005$ for JA2 and $u_{io} \approx 0.001$ for XM39. A number of factors, including a large number of ion-neutral collisions near the sheath edge, could reduce the ion inflow velocity much below sonic conditions. There is no reason to consider these velocities unreasonable.

3. There is evidence [21] that the capillary model may generate an outflow density and pressure that is higher than reality. Results from Case S2 (Chapter III) indicate that the pressure in the plasma holding chamber is more than twice the experimental pressure. A capillary density that is higher than in the experiment would yield a higher convective heat flux simply due to the presence of the plasma density (n_o) in Eqn. 5.8. Further experimental validation of the capillary model may be required to find how well the model predicts capillary outflow pressure. It is possible that the sonic boundary condition might yield an inaccurate result, as it is possible that the outflow velocity is greater than sonic speed.

4. The final theory as to why the convective heat flux is larger than the total heat flux is more unorthodox, yet has a foundation in experimental data. It has long been suspected that radiation is a significant source of heat flux in the PPI [2]. Experimental data [12], discussed in Section 4.4, indicates that the radiative heat flux in this case may be on the order of the total heat flux estimated by the E3TC model. The final theory to explain the convective heat flux anomaly is thus that the plasma does not come into physical contact with the propellant surface. There is evidence that the ablated propellant particles provide radiation shielding to the propellant surface [5]. Any gas dense enough to provide a significant amount of radiation shielding would also likely shield

heavy particle flux. It is possible that, after a very brief transient time, the ablated propellant gas near the surface shields the propellant surface from physical contact with the plasma. Although a small percentage of plasma ions would likely reach the surface, it is possible that they would form a small, or negligible, heat flux. If this were the case, then the plasma-propellant chemistry effects discussed in Appendix C would be entirely negligible.

6.5 Conclusions

Presented was the end-to-end electrothermal chemical gun model, abbreviated as the E3TC model, that is the major result of this thesis. The E3TC model is composed of the numerical models outlined in Chapters II—V, along with experimental data outlined in Chapter I. The main result of the model is the simulation of the plasma-propellant interaction, leading to an estimate of the total heat flux reaching the propellant bed during the PPI. Estimates for the convective heat flux reaching the propellant surface are shown to be non-physical, and theories are presented to explain this discrepancy. The estimate of the total heat flux to the propellant bed falls within the expected values based on available experimental data. Although average values were used for the plasma density and temperature obtained from CFD, this should be viewed as a limitation of the present simulation, and not the model as a whole, as time accurate data could be used if time permitted.

CHAPTER VII

Conclusion

This chapter provides a brief overview of the entire thesis, singles out original contributions of this work, and outlines potential future work.

7.1 Summary

Presented in this thesis were the components of an end-to-end electrothermal chemical gun model. Each component is itself a complete model that yields results that provide insight into the physical phenomena encountered in ETC guns. The models presented allow for the simulation of an electrothermal chemical gun, from the generation of the ignition plasma, to the interaction of the plasma jet with the solid propellant. The individual models presented cover the capillary plasma generator (Chapter II), the expanding plasma jet undergoing plasma-air chemistry (Chapter III), the plasma-propellant interaction itself (Chapter IV), and a collisional plasma sheath model (Chapter V) that becomes part of the PPI model. These four sub-models were combined to form the end-to-end electrothermal chemical gun (E3TC) model in Chapter VI.

7.2 Original Contributions

It is of great importance to outline the original contributions made by any doctoral thesis, as it is the ultimate goal of the researcher to make original contributions to the field of their endeavor. Outlined below is a numbered list of major original contributions, made by the present work, in the field of electrothermal chemical gun modeling.

1. **ETC capillary parameter study performed to find how varying peak discharge current and internal capillary radius affect total capillary ablated mass, peak pressure, and plasma temperature. (Chapter II)** The previously developed capillary model [14, 15] was utilized for the parameter study. It was found that the variation in peak pressure and capillary ablated mass as a function of peak discharge current show linear behavior. The greatest variation in peak pressure and ablated mass came not from varying the capillary internal radius, but by changing the peak discharge current. The study conclusively shows that for the range of conditions commonly used in ETC capillaries, a plasma temperature of $T_e \approx 1.4 - 1.5$ eV can be assumed. This information can aid in the design of capillaries for many applications.

2. **Capillary study revealed a non-linear correlation between total deposited electrical energy and total ablated mass or peak pressure. (Chapter II)** By holding the total electrical energy deposited to the capillary constant by varying the peak electrical current at a range of internal capillary radii, a non-linear relation was found in the results for total ablated mass and peak pressure. For the same electrical energy, a higher capillary outflow pressure and total ablated mass can be obtained by using a capillary of smaller

internal radius. This result can be of great use in the design of capillaries for ETC use, where the total energy deposited to the capillary is an important variable, as the power system must be compact and mobile in practical ETC gun implementation. This study would be very costly and time consuming to conduct experimentally, as multiple capillaries of different radii would have to be constructed and fired.

3. **A CFD plasma-air chemistry model for ETC application was developed based on prior experimental and theoretical work. (Chapter III)** The species used in the plasma-air chemistry model were selected based on previous modeling work conducted at ARL, as well as experimental measurements of the capillary plasma jet performed at Penn State by Li *et al.* Although previous modeling was performed at ARL, careful evaluation of the published data shows that their CFD model failed to maintain quasi-neutrality at the end point of the simulation, which could result in inaccurate chemical recombination rates. The CFD model used in the present work ensures quasi-neutrality via the implementation of a diffusion limiter for electrons. Reaction rates come from Park's model for all oxygen and nitrogen chemistry, and the GRI-Mech project for hydrocarbon-air chemistry. The species list was then refined by simulating a typical capillary plasma jet, with the final model containing 20 species and 41 reactions.

4. **CFD simulation shows that using a plasma holding chamber yields misleading results for the composition of the capillary plasma jet. (Chapter III)** Previous experimental results from Li *et al.* [7] used a plasma holding chamber to slow the plasma flow over a mass spectrometer probe in

an attempt to determine the chemical composition of the plasma jet. Results from simulations designed to match the experimental configuration show conclusively that using a plasma holding chamber fundamentally alters the chemistry happening in the plasma jet, resulting in a chemical composition for the secondary jet that can not be related back to the original plasma jet composition. The use of a plasma holding chamber to find the chemical composition of the capillary plasma jet is concluded to not be a viable option.

5. **Bayonet tube simulation shows that drastically different chemical species are present near the capillary nozzle and the back of the tube. (Chapter III)** Simulation of a proposed ignition geometry for ETC application yields data that shows that locations near the capillary nozzle are exposed to plasma that has undergone negligible plasma-air chemical interactions, while locations far from the capillary are exposed to plasma species that have undergone significant plasma-air chemical interactions, which also affects the plasma temperature. How the difference in plasma chemical composition will affect the plasma-propellant interaction is not known, but this simulation highlights the existence of such a non-uniformity.

6. **The development of a plasma-propellant interaction model, based on analytical ablation and computational thermal models. (Chapter IV)** This is the main contribution of the present work. Prior modeling of the ETC phenomenon had neglected the PPI entirely, focusing on plasma jet or plasma radiation modeling. The coupling of the analytical ablation model to a simple thermal model yields a powerful tool for modeling ETC guns. Utilizing simple experimental data concerning the propellant total ablated mass caused by the

PPI, the constant heat flux received by the propellant can be found for a range of bulk plasma densities. The ability to determine even an approximate value for the heat flux reaching the propellant is significant, as this quantity is difficult, and potentially impossible, to measure. By comparing the results for two different propellants, JA2 and XM39, which have different optical properties, evidence was found that indicates penetrating plasma radiation is a significant heat source in the plasma-propellant interaction.

7. **Design and use of a collisional plasma sheath model to determine the convective heat flux to the propellant bed. (Chapters V and VI)** A collisional plasma sheath model tailored for ETC application is implemented as a module in the PPI model. The sheath model allows for the calculation of the convective heat flux reaching the propellant bed during the PPI. It is found that, for a reasonable range of ion inflow velocities, the convective heat flux is higher than the total heat flux, a physically contradictory result. Potential explanations for this discrepancy are outlined. In brief, the possible explanations are: 1) the sheath model does not capture all of the relevant physics; 2) the ion inflow velocity is much smaller than the previously estimated "reasonable range"; 3) the plasma does not come into physical contact with the propellant bed, making the actual convective heat flux approximately zero. The actual explanation could be a combination of any of the three of the above possibilities. As this result was unexpected, it highlights the complexity of the plasma-propellant interaction, while the third possibility emboldens the widely held belief in the ETC community that plasma radiation is a significant heating mechanism in the PPI.

8. **The development of an end-to-end electrothermal chemical gun model. (Chapter VI)** The E3TC model is the first attempt to simulate the ETC phenomenon, starting from the capillary plasma source, through the expanding plasma jet, to the plasma-propellant interaction. Utilizing the models outlined in this thesis, the E3TC model calculates the heat flux reaching the propellant bed in a specific experimental setup. This heat flux is found to be on the order of the radiative heat flux estimated to reach the propellant bed, as determined experimentally [12]. The best use of this model would be to conduct an experiment and use that geometry and resulting data to perform the simulation to determine the total heat flux to the propellant bed.

7.3 Future Work

The following is a list of suggested future works. It includes additional models to be developed and incorporated into the E3TC model, as well as simulations that can be run with the current model.

1. Performing a series of additional studies, similar to that of Chapter VI, to determine how total heat flux is dependent on capillary radius, current profile, and the capillary-sample distance would be useful. The experimental data for propellant ablated mass due to the PPI that was utilized throughout this thesis was for a fixed capillary-sample distance of 25 mm, although data for smaller capillary-sample distances was available. The reason this one distance was used was because it was the only case for which there was no propellant fracturing due to the plasma front striking the propellant sample. If the experiment outlined in [5] could be repeated for larger capillary-sample distances and different peak discharge currents, the dependence of the total heat flux on

these parameters could be explored.

2. Plasma-surface chemistry should be explored, both in terms of possible film deposition and catalytic chemical reactions that can occur on the surface. A simple model for the heat transfer due to film deposition is outlined in Appendix C, but the bulk of the research needed to be done in this regard is left as future work.

3. Additional validation of the capillary model should be performed. Pressure output from the plasma holding chamber of Case S2 from Chapter III indicates that the pressure from the capillary model may be higher than reality. Additional validation experiments could be performed, where the capillary is fired into a closed chamber and the resulting pressure is detected, and then simulated. This would address questions regarding the accuracy of the capillary model.

4. Although there has been limited success in the past, radiation modeling for ETC application should still be pursued. One possibility is to use NASA's NEQAIR code [49]. NEQAIR requires "line of sight" data for temperature and species number densities to the point of interest, which would be the propellant sample here. A line normal to the surface of the propellant sample could be generated from the CFD data of Chapter III and input into the NEQAIR code. As it currently exists, NEQAIR only includes nitrogen and oxygen species, but has the framework and capability to incorporate hydrogen and carbon species. NEQAIR could then provide an estimate of the radiation reaching the propellant surface. LeMANS, the CFD code used throughout this thesis, has successfully been paired with NEQAIR in the past for determination

of the radiative heating of reentry capsule heat shields [50].

APPENDIX

APPENDIX A

Ablation Model

This appendix contains a detailed description of the ablation model used extensively in Chapters II and IV, and referred to elsewhere in this thesis. The model was originally developed by Keidar *et al.* for the modeling of Teflon ablation in pulsed plasma thrusters [18]. Keidar's model is based on the concept of coupling the kinetic laser ablation theory of Anisimov [39] with a hydrodynamic non-equilibrium layer to relate the wall properties to the bulk plasma properties. Keidar's model has been successfully applied to modeling ablation in Teflon pulsed plasma thrusters [16], ETC polyethylene capillaries [14, 15, 13] (as discussed in Chapter II), as well as circuit breaker ablation [51]. In Chapter IV, the ablation model was used to simulate the plasma-propellant interaction that occurs before propellant ignition. In each use, the basics of the model do not change. However, model implementation varies between applications. Keidar's model, which is the same for all of the above cases and throughout this work, is presented below.

The geometry used in the ablation model is shown in Fig. A.1. On the left is the wall material (shown in the figure as Teflon) attached to the Knudsen layer. The coordinate frame is such that $x = 0$ at the surface of the wall, with $x = \infty$ in the bulk plasma. The Knudsen layer is the same as in Anisimov's model [39],

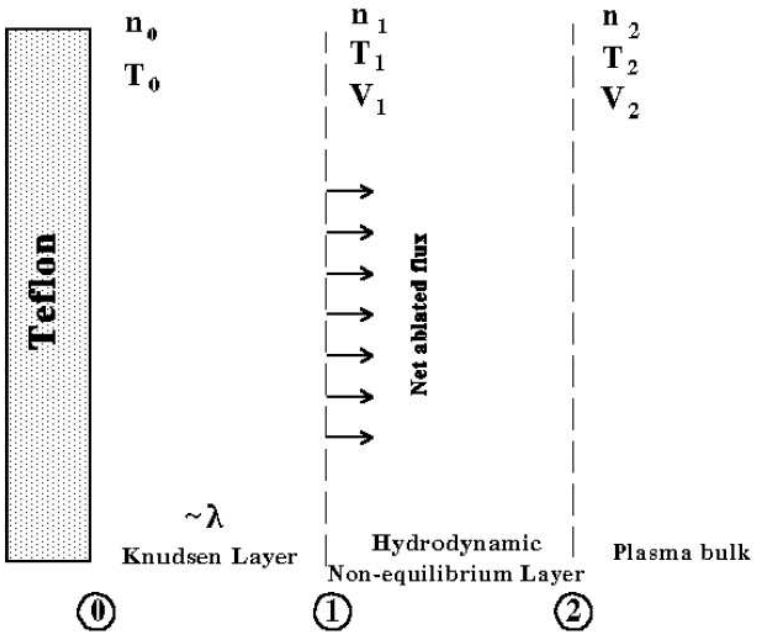

Figure A.1: Diagram of the ablation geometry, taken from [18].

but is attached to a collision dominated non-equilibrium hydrodynamic layer in Keidar's model [18]. Per Anisimov's model, it is assumed that the velocity distribution function in the Knudsen layer can be accurately represented as a Maxwellian, $f(\mathbf{v})$, provided the heavy particle flux is in the direction of the non-equilibrium layer. If the heavy particle flux is in the opposite direction (returned wall flux) then the velocity distribution function is given by $\beta f_1(\mathbf{v})$, where β is a proportionality constant to be found numerically, and $f_1(\mathbf{v})$ is a Maxwellian distribution shifted by velocity V_1 in the direction of the wall. Thus

$$f(\mathbf{v}) = n_0 \left(\frac{m}{2\pi k T_0}\right)^{3/2} \exp\left(-\frac{mv^2}{2kT_0}\right), \quad v_x \geq 0,$$

$$\beta f_1(\mathbf{v}) = \beta n_0 \left(\frac{m}{2\pi k T_0}\right)^{3/2} \exp\left(-m\frac{(v_x - V_1)^2 + v_y^2 + v_z^2}{2kT_0}\right), \quad v_x < 0.$$

The following conservation integrals can then be used in the Knudsen layer, where the limits are over all velocity space.

$$C_1 = \int_{-\infty}^{\infty} v_x f(x, \mathbf{v}) d^3v \tag{A.1}$$

$$C_2 = \int_{-\infty}^{\infty} v_x^2 f(x, \mathbf{v}) d^3v \tag{A.2}$$

$$C_3 = \int_{-\infty}^{\infty} v_x v^2 f(x, \mathbf{v}) d^3v \tag{A.3}$$

When evaluated across the Knudsen layer the following system of equations results,

$$\frac{n_0}{2\sqrt{\pi d_0}} = n_1 V_1 + \beta \frac{n_1}{2\sqrt{\pi d_1}} \left(\exp(-\alpha^2) - \alpha\sqrt{\pi}\, \mathrm{erfc}(\alpha) \right), \tag{A.4}$$

$$\frac{n_0}{4d_0} = \frac{n_1}{2d_1} \left((1 + 2\alpha^2) - \beta \left[(0.5 + \alpha^2)\, \mathrm{erfc}(\alpha) - \frac{\alpha \exp(-\alpha^2)}{\sqrt{\pi}} \right] \right), \tag{A.5}$$

$$\frac{n_0}{(\pi d_0)^{1.5}} = \frac{\alpha\, n_1}{\pi (d_1)^{1.5}} \left[(\alpha^2 + 2.5) - \frac{\beta}{2} \left((\alpha^2 + 2.5)\, \mathrm{erfc}(\alpha) - (2 + \alpha^2) \frac{\exp(-\alpha^2)}{\alpha\sqrt{\pi}} \right) \right], \tag{A.6}$$

where $d_0 = m/2kT_0$, $d_1 = m/2kT_1$, $\alpha = V_1/\sqrt{2kT_1/m}$, $\mathrm{erfc}(\alpha) = 1 - \mathrm{erf}(\alpha)$, $\mathrm{erf}(\alpha)$ is the error function, T_0 is the surface temperature, and n_0 is the equilibrium surface density.

Applying the mass and momentum conservation equations for a single heavy particle fluid in the non-equilibrium hydrodynamic layer, under the assumption of a quasi-neutral plasma, yields the following relations,

$$n_1 V_1 = n_2 V_2, \tag{A.7}$$

$$n_1 k T_1 + m n_1 V_1^2 = n_2 k T_2 + m n_2 V_2^2. \tag{A.8}$$

The velocity at the outer boundary, V_2 can be eliminated by combining Eqs. A.7 and A.8, yielding

$$\alpha^2 = \frac{n_2 T_2 / 2T_1 - n_1/2}{n_1 (1 - n_1/n_2)}\ . \tag{A.9}$$

The system of equations is closed if the equilibrium density at the ablating wall, n_0, can be specified. For this parameter, the equilibrium vapor pressure is employed, along with the idea gas law. The system is thus closed via the relation

$$P_V = n_0 k T_0, \tag{A.10}$$

where P_V is the equilibrium vapor pressure of the ablating material at temperature T_0. The vapor pressure is different for each application, as it changes from one wall material to another, and is usually modeled via a Clausius-Clapeyron relation [18, 37, 51].

The system to be solved contains five equations (A.4, A.5, A.6, A.9, A.10), and five unknowns (n_0, n_1, T_1, V_1, β). The remaining variables (n_2, T_2, T_0) are parameters of the solution. The bulk plasma properties, n_2 and T_2, are easily specified. The ablating surface temperature, T_0, can either be incremented parametrically, or solved for using a thermal model for the ablating surface, as done in Chapters II and IV, and references [14, 37, 51]. The ablation code solves the five coupled equations numerically. When the solution is found the ablation rate can be calculated as

$$\Gamma = m n_1 V_1 = m n_1 \sqrt{\frac{n_2 k T_2 - n_1 k T_1}{m n_1 (1 - n_1/n_2)}} \ . \tag{A.11}$$

Due to the analytical nature of the model, computation times are low. It's generality and wide range of applicability make it useful in a number of ablation applications, as previously cited.

APPENDIX B

Derivation of Eqn. 5.8

The derivation of the equation for the convective heat flux reaching the propellant surface, in the collisional plasma sheath model, is presented below. Although this expression is commonly used in discharge modeling, locating a derivation can prove elusive, and it's end form can be confusing for those not familiar with it's usage. It is presented here for completeness.

The derivation begins with the Maxwellian velocity distribution function for electrons in the bulk plasma, which is

$$f(v) = n\left(\frac{m_e}{2\pi e T_e}\right)^{3/2} \exp\left(-\frac{m_e v^2}{2eT_e}\right), \tag{B.1}$$

where m_e is the electron mass, e is the fundamental charge, v is velocity, n is the plasma number density, and T_e is the electron temperature in Volts. The electron velocity distribution function is normalized such that integrating over all velocities yields the bulk plasma density, shown below.

$$\int_{-\infty}^{\infty} f(v) d^3v = \int_0^{2\pi}\int_0^{\pi}\int_0^{\infty} f(v) v^2 \sin(\theta) dv d\theta d\tau = n, \tag{B.2}$$

where the integration is performed in spherical coordinates.

The electron energy flux to the surface, in the absence of a plasma sheath, is

$$2\pi \int_0^{\pi/2}\int_0^{\infty} f(v)\left(v\cos(\theta)\frac{1}{2}m_e v^2\right) v^2 \sin(\theta) dv d\theta = 2eT_e F_e, \tag{B.3}$$

where $F_e = n\sqrt{eT_e/(2\pi m_e)}$ is the electron flux to the surface. The kinetic energy per electron striking the surface is thus $2eT_e$. Equation B.3 is a common result found in many plasma textbooks [19]. Note that the substitutions $\int_0^{2\pi} d\tau = 2\pi$ and $v_x = v\cos(\theta)$ have been made. The third term in Eqn. 5.8 appears due to the presence of the plasma sheath potential, affecting the kinetic energy of the electrons. Since electrons have a potential hill to climb in order to reach the wall, only electrons with sufficient kinetic energy can be included in the integral. Rather than the limits $v \in [0, \infty]$ in Eqn. B.3, the minimum velocity, in the x direction, is now v_ϕ, which is the velocity required to reach the top of the potential hill. One can find v_ϕ by equating the electron kinetic energy to the wall potential, such that $\frac{1}{2}m_e v_\phi^2 = e\phi$, where $\phi = |\phi_w|$ for simplicity. The new minimum acceptable velocity is

$$v_\phi = \sqrt{\frac{2e\phi}{m_e}}\ . \tag{B.4}$$

The lower limit of Eqn. B.3 is now $v_\phi/\cos(\theta)$. The electron energy flux to the surface is then

$$2\pi \int_0^{\pi/2} \int_{v_\phi/\cos(\theta)}^{\infty} f(v) \left(v\cos(\theta)\frac{1}{2}m_e v^2 \right) v^2 \sin(\theta) dv d\theta = (2eT_e + e\phi)F_e, \tag{B.5}$$

where $F_e = n\sqrt{eT_e/(2\pi m_e)}\exp(-\phi/T_e)$ is again the electron flux, but it has been reduced by an exponential factor due to the plasma sheath potential. The average energy per particle to the surface, due to the electrons, is now $(2eT_e + e\phi)$, where the per particle energy has been increased by the presense of the plasma sheath.

The ion energy flux to the surface is simply $(\frac{1}{2}m_i v_{iw}^2)F_i$, where F_i is the ion flux to the surface, and v_{iw} is the ion-wall impact velocity, as determined by the computational sheath model. The convective heat flux to the wall is then

$$q_{\text{conv}} = F_i \left(\frac{1}{2}m_i v_{iw}^2 \right) + F_e \left(2eT_e + e|\phi_w| \right). \tag{B.6}$$

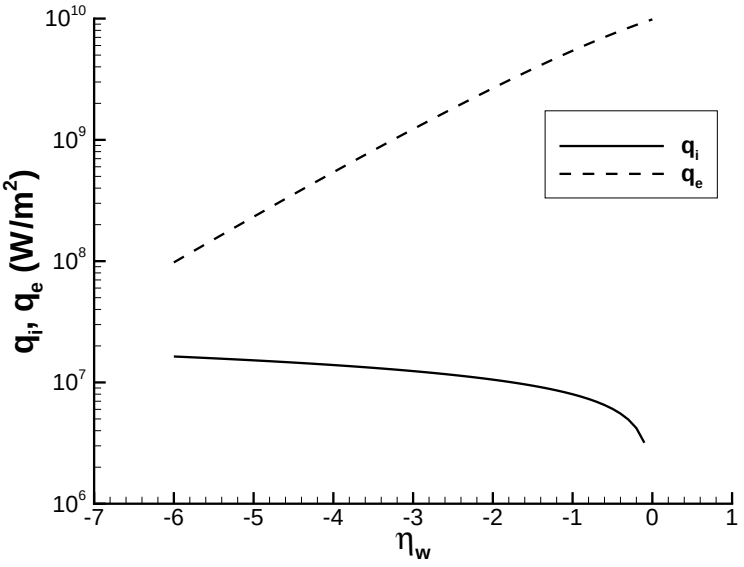

Figure B.1: Comparison of ion and electron heat fluxes at a range of wall potential.

Figure B.1 shows the convective heat flux due to ions (q_i) and electrons (q_e) for a typical plasma density and collisionality, where the fully collisional ion-wall impact velocity (Eqn. 5.9) has been used. The non-dimensional sheath potential, $\eta_w = \phi_w/T_e$, is varied over a range typically encountered in this work. Note that as the wall potential increases in magnitude, the ion heat flux increases and the electron heat flux decreases.

In the steady state sheath assumption, neglecting ionization in the sheath, the ion and electron fluxes into the sheath are equal. Thus, $F_i = F_e = n_o v_{io}$, where n_o is the bulk plasma density at the sheath edge and v_{io} is the ion inflow velocity to the sheath. Substitution of the non-dimensional variables, defined in Chapter V, yields Eqn. 5.8.

APPENDIX C

Chemistry Effects in the Plasma-Propellant Interaction

Due to the complex chemical nature of the propellants used in ETC application, the possibility arises that there are chemical interactions between the plasma and the propellant surface; or with the ablated propellant gas and the propellant surface. Modeling these interactions poses many difficulties, however, as the exact state of the propellant chemicals at the surface is not known. This appendix presents concepts for a model to include chemical effects in the PPI simulation. Although the following discussion is mostly qualitative in nature, it is presented to outline the current thinking regarding modeling this challenging aspect of the plasma-propellant interaction, which has not previously been addressed.

C.1 Ablated Propellant Gas Chemistry

It is generally believed that the ablated propellant gas exists in an atomic, or simple molecular state, and that these chemical species can contain radicals, or even become ionized themselves [2]. The difficulty in modeling arises because the propellant is chemically very complex, with tens of bonds per constituent chemical species. Determining how these species will dissociate, and at what energies, is a complex "chemical mechanism" problem. Table C.1 contains the chemical makeup of the

Table C.1: Composition of the propellant JA2, with chemical formulas, taken from [9].

Constituent	% by Weight	Chemical Formula
Nitrocellulose	58.21	HNO_3
Diethylene Glycol Dinitrate	25.18	$C_4H_8N_2O_7$
Nitroglycerin	15.79	$C_3H_5(NO_3)_3$
Akardit II	0.74	$C_{14}H_{14}N_2O$
Magnesium Oxide	0.05	MgO
Graphite	0.03	C

propellant JA2, along with the chemical formula for each constituent species. Although JA2 is comprised of only five atomic species, the structure of it's constituent compounds can be exceedingly complex.

The chemical structure of Akardit II is shown in Fig. C.1. It becomes apparent that the mechanism by which Akardit II will dissociate is not trivial, especially when considering the two benzene rings. Therefore, in order to conduct even simple simulations of the chemical effects with the ablated propellant gas, a mechanism model for each constituent species must be found. With that knowledge, the ablation model outlined in Appendix A—and used in the PPI model—can easily be modified to ablate each constituent species separately, allowing for this chemical data to be fully utilized.

C.2 Film Growth

One way that propellant surface chemistry could affect the PPI is if film growth were possible. When the propellant ablates, there is the potential that some fraction of the ablated propellant will backflux onto the surface. This film deposition would

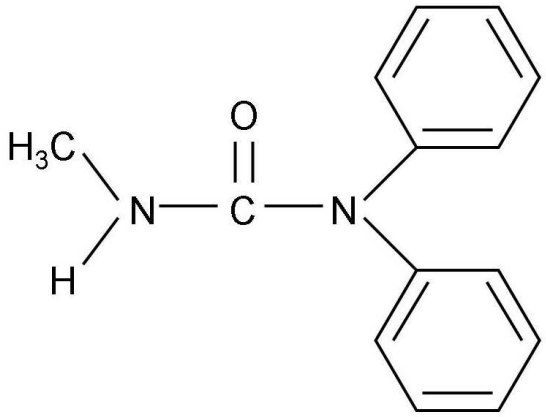

Figure C.1: Chemical structure of Akardit II.

likely happen with dissociated carbon atoms, as this is a common occurrence observed in pulsed plasma thrusters [52]. The deposited carbon will not re-ablate, however. Figure C.2 shows the vapor pressure of carbon, compared to that of the propellants JA2 and XM39, over a range of surface temperatures encountered during the PPI. Note the difference in scales. The vapor pressure of carbon, over this temperature range, is many orders of magnitude lower than the vapor pressure of JA2 or XM39. Recall that, in general, a material will not ablate if it's vapor pressure is lower than ambient pressure, taken here to be 101325 Pa. Indeed, an ablation simulation conducted for pure carbon indicates that no ablation will occur over this temperature range. Thus, any film that might grow during the PPI will persist until combustion is initiated.

The formation of (exothermic) chemical bonds on the surface would serve as an energy source in the PPI, increasing the propellant surface temperature. If the bond formed during film growth is taken to be simply $C+C \rightarrow C_2$, then every mole of carbon that reattaches to the propellant surface contributes 6.36 eV of energy to the PPI [53].

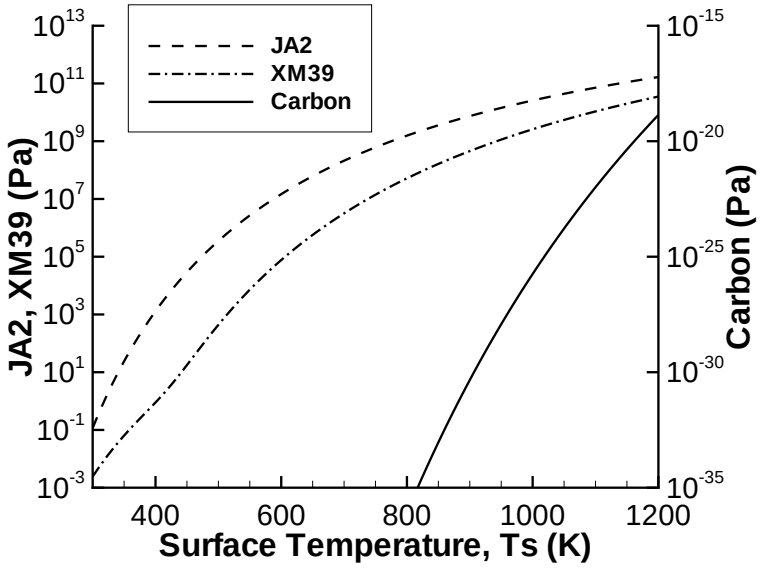

Figure C.2: Vapor pressure of carbon, and how it compares to that of JA2 and XM39.

The following simple model can be used in the PPI model to simulate the energy deposition due to film growth. The initial propellant surface area, exposed to the plasma, is given as A. The carbon film will form a patchy cover over some fraction of the surface, resulting in a decrease in PPI surface area. One can assume the fraction of the propellant surface area that is covered by film to be X. The new PPI surface area that ablates is thus $(1 - X)A$. Recall that the PPI model has a timestep Δt, where at each timestep a propellant mass of ΔM is ablated. Some fraction of this ablated mass will backflux to the surface. It could be all the carbon of the ablated mass, or only some small fraction of it. One can denote the amount of propellant backflux as $\Delta M_b = b\Delta M$, where $0 \leq b \leq 1$ takes into account the fact that certain chemical species, such as hydrogen, are unlikely to backflux. In a simple model, one can assume that only carbon will backflux, thus b is the fraction, by mass, of the propellant that is carbon. Some fraction of this returned flux, ΔM_b, will form a film. Here it is assumed that only carbon will form the film. Thus, the total mass of

carbon, at each timestep, that is added to the film is denoted as ΔM_f.

As previously mentioned, the exothermic energy of the carbon bonding reaction is Θ=6.36 eV/mole=1.693×10^{-42} J/particle. The heat flux to the surface, given originally as Eqn. 4.4, is reproduced below.

$$\frac{\partial T_s}{\partial x} = -\lambda^{-1}(q - \Delta H\Gamma - C_p(T_s - T_o)\Gamma)$$

The above modeling assumptions can be used to add a new heat source to Eqn. 4.4 to account for the exothermic carbon-carbon bonds formed during the film growth. Adding this new term results in Eqn. C.1 below.

$$\frac{\partial T_s}{\partial x} = -\lambda^{-1}\left[q - \Delta H\Gamma - C_p(T_s - T_o)\Gamma + \frac{\Theta}{(XA)\Delta t}\left(\frac{\Delta M_f}{m_c}\right)\right] , \qquad \text{(C.1)}$$

where m_c is the mass of an individual carbon atom. The expression $\Theta/(XA\Delta t)$ is the energy added by film growth per carbon atom bonding to the surface. The expression $\Delta M_f/m_c$ is simply the number of carbon atoms, per timestep, that bond to the film.

The remaining difficulty lies in the determination of ΔM_f, which is essentially the rate of film growth, from ΔM_b. The most reliable way to determine ΔM_f would be to conduct a molecular dynamics simulation, as this computational method has been used before to successfully model film growth [54] and ablation [55]. Molecular dynamics simulations model the motion of groups of atoms by simulating the interatomic forces that facilitate particle-particle interactions. This allows for modeling film growth by directly modeling the bond potential between carbon atoms. The probability of bond formation can thus be directly simulated, resulting in an expression for ΔM_f. Although the development of this film growth model is left as future work, an approximate calculation can be done now. If it is assumed that all carbon in the propellant returns to the surface and forms a film, with $X = 1$ in Eqn. C.1,

then the heat flux due to film growth in the experiment outlined in Chapter IV can be estimated.

By examining the chemical formulas and percent composition of the constituent compounds in JA2 and XM39, the fraction of the propellant mass that comes from carbon can be found. The mass fraction of JA2 that is carbon is 9.25×10^{-2}, and 2.25×10^{-1} for XM39. Assume a discharge time of t=280 μs, and let ΔM_f be the total film mass, rather than the film mass at each timestep, thus $(\Delta M_f/\Delta t) \rightarrow (M_f/t) = (M \times (\text{propellant carbon fraction}))/280\ \mu\text{s}$, where M is the total ablated propellant mass. Using these assumptions in the fourth term of Eqn. C.1 yields a heat flux due to carbon film growth of 1.59×10^{-15} W/m^2 for JA2 and 2.05×10^{-15} W/m^2 for XM39. Although these heat fluxes are very small, it should be noted that the total mass and surface area is also very small. The propellant surface area in this case is $A = 9.33 \times 10^{-5}$ m^2, with M=5.3 or 2.8 mg for JA2 or XM39, respectively. In actual ETC application, the surface chemistry heat flux will increase as the surface area and total ablated mass increases, yet the radiation and convective heat fluxes will remain the same. It is left as future work to determine the level of importance of this heat source in practical ETC application.

BIBLIOGRAPHY

BIBLIOGRAPHY

[1] Koleczko, A., Ehrhardt, W., Kelzenberg, S., and Eisenreich, N., "Plasma Ignition and Combustion," *Propellants, Explosives, Pyrotechnics*, Vol. 26, 2001, pp. 75–83.

[2] Pesce-Rodriguez, R. A. and Beyer, R. A., "A Theory of Plasma-Propellant Interactions," *ARL-TR-3286*, 2004.

[3] Dyvik, J., Herbig, J., Appleton, R., O'Reilly, J., and Shin, J., "Recent Activities in Electrothermal Chemical Launcher Technologies at BAE Systems," *IEEE Transactions on Magnetics*, Vol. 43, No. 1, 2007, pp. 303–307.

[4] Beyer, R. A. and Brant, A. L., "Plasma Ignition in a 30-mm Cannon," *IEEE Transactions on Magnetics*, Vol. 43, No. 1, 2007, pp. 294–298.

[5] Li, J., Litzinger, T. A., and Thynell, S. T., "Interaction of Capillary Plasma with Double-Base and Composite Propellants," *Journal of Propulsion and Power*, Vol. 20, No. 4, 2004, pp. 675–683.

[6] Li, J., Litzinger, T. A., Das, M., and Thynell, S. T., "Study of Plasma-Propellant Interaction During Normal Impingement," *Journal of Propulsion and Power*, Vol. 22, No. 5, 2006, pp. 929–937.

[7] Li, J., Litzinger, T. A., Das, M., and Thynell, S. T., "Recombination of Electrothermal Plasma and Decomposition of Plasma-Exposed Propellants," *Journal of Propulsion and Power*, Vol. 22, No. 6, 2006, pp. 1353–1361.

[8] Li, J., private communication, March 2007.

[9] Miller, M. S., "Thermophysical Properties of Six Solid Gun Propellants," *ARL-TR-1322*, 1997.

[10] Beyer, R. A. and Pesce-Rodriguez, R. A., "The Response of Propellants to Plasma Radiation," *IEEE Transactions on Magnetics*, Vol. 41, No. 1, 2005, pp. 344–349.

[11] Beyer, R. A., private communication, November 2005.

[12] Das, M., Thynell, S. T., Li, J., and Litzinger, T. A., "Transient Radiative Heat Transfer from a Plasma Produced by a Capillary Discharge," *Journal of Thermophysics and Heat Transfer*, Vol. 19, No. 4, 2005, pp. 572–580.

[13] Porwitzky, A. J., Keidar, M., and Boyd, I. D., "Numerical Parametric Study of the Capillary Plasma Source for Electrothermal Chemical Guns," *EML paper number 72*, 2008, presented at the 14th Electromagnetic Launch Symposium, Victoria, British Columbia, Canada.

[14] Keidar, M. and Boyd, I. D., "Ablation Study in the Capillary Discharge of an Electrothermal Gun," *Journal of Applied Physics*, Vol. 99, 2006, 053301.

[15] Keidar, M., Boyd, I. D., Williams, A., and Beyer, R. A., "Ablation Study in a Capillary Sustained Discharge," *IEEE Transactions on Magnetics*, Vol. 43, No. 1, 2007, pp. 308–312.

[16] Keidar, M., Boyd, I. D., and Beilis, I. I., "Model of an Electrothermal Pulsed Plasma Thruster," *Journal of Propulsion and Power*, Vol. 19, No. 3, 2003, pp. 424–430.

[17] Keidar, M., Fan, J., Boyd, I. D., and Beilis, I. I., "Vaporization of Heated Materials into Discharge Plasmas," *Journal of Applied Physics*, Vol. 89, No. 6, 2001, pp. 3095–3098.

[18] Keidar, M., Boyd, I. D., and Beilis, I. I., "On the Model of Teflon Ablation in an Ablation-Controlled Discharge," *Journal of Physics D*, Vol. 34, 2001, pp. 1675–1677.

[19] Lieberman, M. A. and Lichtenberg, A. J., *Principles of Plasma Discharges and Materials Processing*, 2005, Wiley-Interscience, New Jersey, Second Edition.

[20] Keidar, M., Boyd, I. D., and Beilis, I. I., "Electrical Discharge in the Teflon Cavity of a Coaxial Pulsed Plasma Thruster," *IEEE Transactions on Plasma Science*, Vol. 28, No. 2, 2000, pp. 376–385.

[21] Porwitzky, A. J., Scalabrin, L. C., Keidar, M., and Boyd, I. D., "Chemically Reacting Plasma Jet Expansion Simulation for Application to Electrothermal Chemical Guns," *AIAA 2007-4600*, 2007, presented at the 38th AIAA Plasmadynamics and Lasers Conference, Miami, Florida.

[22] Nusca, M. J., Anderson, W. R., and McQuaid, M. J., "Multispecies Reacting Flow Model for the Plasma Efflux of an ETC Ignited–Application to an Open-Air Plasma Jet Impinging on an Instrumented Probe," *ARL-TR-3227*, 2004.

[23] Nusca, M. J., McQuaid, M. J., and Anderson, W. R., "Numerical Simulation of an Open-Air Plasma Jet Using a Multi-species Reacting Flow CFD Code," *AIAA 2000-2675*, 2000, presented at the 31st AIAA Plasmadynamics and Lasers Conference, Denver, CO.

[24] Sutton, K. and Gnoffo, P. A., "Multi-Component Diffusion with Application to Computational Aerothermodynamics," *AIAA 1998-2575*, 1998, presented at the 7th AIAA/ASME Joint Thermophysics and Heat Transfer Conference, Albuquerque, NM.

[25] Scalabrin, L. C., private communication, October 2006.

[26] Scalabrin, L. C. and Boyd, I. D., "Development of an Unstructured Navier-Stokes Solver For Hypersonic Nonequilibrium Aerothermodunamics," *AIAA 2005-5203*, 2005, presented at the 38th AIAA Thermophysics Conference, Toronto, Canada.

[27] Scalabrin, L. C. and Boyd, I. D., "Numerical Simulation of Weakly Ionized Hypersonic Flow for Reentry Configurations," *AIAA 2006-3773*, 2006, presented at the 9th AIAA/ASME Joint Thermophysics and Heat Transfer Conference, San Francisco, California.

[28] Scalabrin, L. C., *Numerical Simulation of Weakly Ionized Hypersonic Flow Over Reentry Capsules*, 2007, PhD thesis, Department of Aerospace Engineering, University of Michigan.

[29] Gupta, R. N., Yos, J. M., Thompson, R. A., and Lee, K., "A Review of Reaction Rates and Thermodynamic and Transport Properties for an 11-Species Air Model for Chemical and Thermal Nonequilibrium Calculation to 30000K," *NASA Reference Publication 1232*, 1990.

[30] GRI-Mech Home Page, http://www.me.berkeley.edu/gri_mech/.

[31] Chang, Y. and Ordonez, C. A., "Generalization of the Arrhenius relation and Ionization Reaction Rates for Carbon Atoms and Ions in Plasmas," *Chemical Physics*, Vol. 231, 1998, pp. 27–30.

[32] Chang, Y. and Ordonez, C. A., "Semi-Empirical Ionization and Excitation Rate Coefficients for Hydrogen, Helium, and Oxygen Atoms and Ions in Plasmas," *AIP Conference Proceedings*, Vol. 475, 1999, pp. 887–890.

[33] Field, F. H. and Franklin, J. L., *Electron Impact Phenomena and the Properties of Gaseous Ions*, 1970, Academic Press, New York, Revised Edition.

[34] McBride, B. J. and Gordon, S., "Computer Program for Calculation of Complex Chemical Equilibrium Compositions and Applications; II. Users Manual and Program Description," *NASA Reference Publication 1311*, 1996.

[35] Hurley, J. D., Bourham, M. A., and Gilligan, J. G., "Numerical Simulation and Experiment of Plasma Flow in the Electrothermal Launcher SIRENS," *IEEE Transactions on Magnetics*, Vol. 31, No. 1, 1995, pp. 616–621.

[36] Orton, N. P. and Gilligan, J. G., "Simulation of the Plasma-Surface Interaction in Electric Launchers," *IEEE Transactions on Magnetics*, Vol. 31, No. 1, 1995, pp. 640–644.

[37] Porwitzky, A. J., Keidar, M., and Boyd, I. D., "Modeling of the Plasma-Propellant Interaction," *IEEE Transactions on Magnetics*, Vol. 43, No. 1, 2007, pp. 313–317.

[38] Williams, A. W. and White, K. J., "Plasma-Propellant Interaction Studies: Measurements of Heat Flux Produced by Hydrocarbon Ablation-Supported Plasmas," *IEEE Transactions on Magnetics*, Vol. 37, No. 1, 2001, pp. 203–206.

[39] Anisimov, S. I., "Vaporization of Metal Absorbing Laser Radiation," *Journal of Soviet Physics JETP*, Vol. 27, No. 1, 1968, pp. 182–183.

[40] Porwitzky, A. J., Keidar, M., and Boyd, I. D., "On the Mechanism of Energy Transport in the Plasma-Propellant Interaction," *Propellants, Explosives, Pyrotechnics*, Vol. 32, 2007, pp. 385–391.

[41] Raizer, Y. P., *Gas Discharge Physics*, 1991, Springer-Verlag, Berlin, Germany.

[42] Benilov, M. S., "Can the Temperature of Electrons in a High-Pressure Plasma be Determined by Means of an Electrostatic Probe?" *Journal of Physics D*, Vol. 33, 2000, pp. 1683–1696.

[43] Stangeby, P. C., *The Plasma Boundary of Magnetic Fusion Devices*, 2000, Institute of Physics Publishing, Bristol, UK.

[44] Gerald, C. F. and Wheatley, P. O., *Applied Numerical Analysis*, 2004, Addison-Wesley Publishing Company, Seventh Edition.

[45] Sternovsky, Z. and Robertson, S., "Numerical Solutions to the Weakly Collisional Plasma and Sheath in the Fluid Approach and the Reduction of the Ion Current to the Wall," *IEEE Transactions on Plasma Science*, Vol. 34, No. 3, 2006, pp. 850–854.

[46] Bird, G. A., *Molecular Gas Dynamics and the Direct Simulation of Gas Flows*, 1994, Oxford University Press.

[47] Keidar, M. and Beilis, I. I., "Transition From Plasma to Space-Charge Sheath Near the Electrode in Electrical Discharges," *IEEE Transactions on Plasma Science*, Vol. 33, No. 5, 2005, pp. 1–6.

[48] Sheridan, T. E. and Goree, J., "Collisional Plasma Sheath Model," *Phys. Fluids B*, Vol. 3, No. 10, 1991, pp. 2796–2804.

[49] Whiting, E. E., Park, C., Liu, Y., Arnoldand, J. O., and Paterson, J. A., "NEQAIR96 Nonequilibrium and Equilibrium Radiative Transport and Spectra Program: User's Manual," *NASA-RP-1389*, 1996.

[50] Scalabrin, L. C. and Boyd, I. D., "Numerical Simulations of the FIRE-II Convective and Radiative Heating Rates," *AIAA 2007-4044*, 2007, presented at the 39th AIAA Thermophysics Conference, Miami, Florida.

[51] Martin, A., Reggio, M., Trepanier, J.-Y., and Guo, X., "Transient Ablation Regime in Circuit Breakers," *Plasma Science and Technology*, Vol. 9, No. 6, 2007, pp. 653–656.

[52] Keidar, M., Boyd, I. D., Gulczinski, F. S. I., and Spanjers, G. G., "Propellant Charring in Pulsed Plasma Thrusters," *Journal of Propulsion and Power*, Vol. 20, No. 6, 2004, pp. 978–984.

[53] Martinotti, F. F., Welch, M. J., and Wolf, A. P., "The Reactivity of Thermal Carbon Atoms in the Gas Phase," *Chemical Communications*, 1968, pp. 115–116.

[54] Levchenko, I., Korobov, M., Romanov, M., and Keidar, M., "Ion Current Distribution on a Substrate During Nanostructure Formation," *Journal of Physics D*, Vol. 37, 2004, pp. 1690–1695.

[55] Yim, J. T., *Computational Modeling of Hall Thruster Channel Wall Erosion*, 2008, PhD thesis, Department of Aerospace Engineering, University of Michigan.